

Chapter 1 Overview of Interfacial Reaction, Electromigration and Thermomigration

1.1 Flip-chip technology

To meet the relentless drive for miniaturization of portable devices, flip-chip technology has been adopted for high-density packaging due to its excellent electrical characteristic and superior heat dissipation capability [1]. As the required performance in microelectronics devices becomes higher, flip-chip technology was adopted to increase more signal and power interconnections than wire bonding in electronic devices. In 1960s, IBM first developed the flip chip technology, called as controlled-collapse-chip-connection (C4) [2-4]. In the C4 technology, high-Pb solder with high melting temperature of 320 °C was used as the joint material [5]. Then the chip was aligned on the ceramic substrate. This C4 technology gained wide utilization in the 1980s since it can provides the advantages in size, performance, flexibility, and reliability over other packaging methods. Owing to area array capability in flip chip technology, the size of product, the height of solder bump, and the length of interconnect are effectively reduced, providing the higher input/output (I/O) pin count and speed in electronic devices.

Before flip-chip assemblies, solder bumps need to deposited onto the under bump metallurgy (UBM) on the chip side. The requirements for UBMs are: (1) it must adhere well both on the underlying metal line, like Al or Cu, and on the surrounding IC passivation layer, (2) it is able to provide a strong barrier to prevent the diffusion of bump metals into the integrated circuit (IC) and (3) it needs to be readily wettable by the bump metals during solder reflow. For example, a thin film Cr/Cu/Au UBM is adopted for the high-Pb solder alloy in the C4 technology.

The tilt view of solder joints on silicon chip is shown in Figure 1-1(a). Figure 1-1(b) is the cross-sectional view of the flip-chip solder joints. As depicted in Figure 1-1(c), the chip with IC is then placed upside down (flip chip), and all the joints are formed simultaneously between chip and substrate during the reflowing process. In flip-chip process, electrical connections are the array of solder bumps on the chip surface, hence interconnects distance between package and chip is effectively reduced. The density of I/O is limited by minimum distance between adjacent bonding pads. For high ends device and when size reduction is the main concern, area-arrayed flip chip technologies is the only choice to meet the needs.

However, the flip-chip technology has some evolutions due to certain concern. In order to cost down the consumer electronics, the polymer substrates, like Bismaleimide Triazine (BT) or Flame Retardant 4 (FR4), are used to replace the ceramic substrate. For this concern, the high-Pb solder has no longer been used due to its high melting point of 320 °C since polymers have very low glass transition temperature. Thus, the eutectic SnPb solder alloy can be used to solve this problem by its low melting point of 183 °C. Next, owing to the environment concern, the Pb-free solder alloys replace the Pb-containing solder alloys due to the toxic of Pb. Then, the thin film UBM will not be suitable for this change. Therefore, the electroplating 5- μm Cu or 5- μm Cu/3- μm Ni was used as the UBM for the Pb-free solder joints. Because of these evolutions, several kinds of solder alloys and UBMs are proposed for the flip-chip assemblies. This makes the flip-chip technology become complex to study since there has too many combinations. The best solder alloy and UBM will provide a lot of benefit for the company.

1.2 Introduction to Interfacial Reaction

Solder is widely used to connect chips to their packaging substrates in flip-chip technology as well as in ball-grid-array (BGA) technology [6]. In the last 50 years, the electronics industry has relied mainly on one type of solder (Sn–Pb solder) in products manufacture [7]. With the discovery of lead (Pb) as a contaminant both to the environment and to human health, new developments have been made to steer away from the use of Sn–Pb solder [8,9]. In 2000, National Electronics Manufacturing Initiative (NEMI) recommended to replace eutectic Sn–Pb solder by eutectic Sn–Ag–Cu solder in re-flow processing and eutectic Sn–Cu solder in wave soldering [6].

A reliable solder joint can be formed by a metallurgical reactions between molten solders and under-bump metallization (UBM) on a chip or metallization on the substrate, which produces stable intermetallic compounds (IMCs) at the joint interfaces [10]. During the soldering process, the formation of IMCs between solder alloys and the metallization layer is inevitable. The growth of these IMCs can strongly affect the mechanical reliability of the solder joints [11-13]. As the result, selection of appropriate UBM plays an important role in developing a reliable flip chip joint, especially the adoption of the lead-free solders due to environmental concerns.

Copper is widely used in the UBM and substrate metallization for flip-chip and BGA applications. It is known that at the Cu/solder interface, Sn reacts rapidly with Cu to form Cu–Sn IMC, which weakens the solder joints due to the brittle nature of the IMC [14]. Therefore, Ni is used as a diffusion barrier layer to prevent the rapid interfacial reaction between solder and Cu layer in electronic devices.

Recently, the reaction between solder and Ni has received much attention because the reaction rate is about two orders of magnitude slower than that of Cu, so

that the effect of spalling of IMC on thin film Ni is less serious and Ni can also serve as diffusion barrier. Why the reaction rate between Ni and solder is much slower than that between Cu and solder has been an interesting kinetic question. The answer is not very clear right now; mostly it is because the supply of Ni to the reaction may be much slower than Cu. The supply may depend on the diffusion of Ni along the interface between Ni_3Sn_4 and Ni and also the solubility of Ni in the molten solder [15].

1.3 Introduction to Electromigration

Electromigration is the phenomenon of mass transportation due to momentum transfer from high current density. Such a mechanism can result in open or short circuit modes of failure. The mechanism also impacts both the design and manufacturing of metallization. For electromigration in a metal, the driving force of the net atomic flux consists of two forces: (1) the direct action of electrostatic field on the diffusion atom, electrostatic force, and (2) the momentum exchange between the moving electrons and the ionic atoms, electron wind force. It can be expressed as

$$F = F_{direct} + F_{wind} = Z^*eE = (Z_{el}^* + Z_{wd}^*)eE \quad (1-1)$$

where Z^* is the effective charge number, e is the electron charge, and E is the electric field. The effective charge Z^* is consisted of two terms, Z_{el}^* and Z_{wd}^* . Z_{el}^* is positive and can be regarded as the nominal valence of the diffusion ion in the metal when the dynamic screening effect is ignored. When these positively charged metal ions are under the field effect, this so called “direct force” draws atoms towards the negative electrode. In the contrary, Z_{wd}^* the wind force, is usually negative and represents the momentum effect from electron flow that pushes atoms towards the positive electrode. Generally, the electron wind force dominates and is found to be on the order of 10 for a good conductor like Ag, Al, Cu, Pb, Sn, etc [16]. Z_{wd}^* can also

be positive, but it was found only in transition elements with complex band structures where electron hole conduction plays a more important role [17]. The atomic flux is related to the electric field and thus the current density. The flux equation can then be expressed as the following:

$$J = J_{chem} + J_{em} = -D \frac{dC}{dx} + C \frac{D}{kT} Z^* eE \quad (1-2)$$

$$E = \rho j \quad (1-3)$$

where C is the atomic concentration, D is the atomic diffusivity, k is Boltzmann's constant, and T is temperature. P is the resistivity and j is the current density. The flux is a function of temperature. As shown in the equation below, the atomic diffusivity is exponentially dependent on temperature.

$$D = D_0 \exp\left(-\frac{Q}{RT}\right) \quad (1-4)$$

where D_0 is the diffusion coefficient, R is the gas constant, and Q is the activation energy of diffusion.

For electromigration to occur, a nonvanishing divergence of atomic flux is a requirement. The divergence may be due to a temperature gradient or microstructural inhomogeneity. Since electromigration is cumulative, it affects the failure rate. Therefore, the mean time to failure (MTTF) in the presence of electromigration is given by the equation

$$MTTF = A \frac{1}{j^n} \exp\left(\frac{Q}{kT}\right) \quad (1-5)$$

The electromigration exponent ranges from $n=1$ to $n=6$, i.e. $n=2$ for Al interconnect. The failure mechanism results in voids, cracks, and hillocks in the samples.

1.3.1 Failure Sites and Flux Divergence

Electromigration was first observed in Al metal interconnects. Less than 0.2% Cu atoms were added to Al line to reduce the effect of electromigration [16]. Blech first developed a structure of a short Al or Cu strip in a base line of TiN to conduct electromigration tests as shown in Figure 1-2(a) [18,19]. Because Al or Cu has lower resistance, as electric field was applied on two ends of TiN line, electric current in TiN took a detour to go along the strip of Al or Cu. After electromigration test, a depleted region occurs at the cathode and an extrusion observed at the anode. Figure 1-2(b) is the scanning electron microscope (SEM) image of the morphology of a Cu strip tested for 99 hrs at 350°C with current density of 5×10^5 A/cm². By conservation of mass, both deletion and extrusion should have the same volume change. We can then calculate the drift velocity from the rate of depletion. In the past years, an impetus to study electromigration in very fine conductors has arisen from the development of very large-scale integrated circuits. The conductors are not only interested in small dimensions; they are often assembled into multilayered structure with a certain combination of conductors and insulators. This gives rise to electromigration problems which is distinctly different from simple single-level conductor line.

The metal layer is a two-dimensional conductor film that can be considered as an ensemble of grain boundaries and their intersections as illustrated in Figure 1-3. Experimental observations have indicated that in most cases, mass depletion and accumulation initiate at grain boundary intersection such as triple junctions. The former would eventually lead to the formation of voids or cracks and the latter to hillocks or whiskers. The reason that the grain boundary intersections are likely to be the failure sites is that they often represent the spots where the mass flux would diverge the most. At the grain boundary intersections, there could be an abrupt change in grain size, which produces a change in the number of paths for mass movement;

there also could be a change in atomic diffusivity due to the change in grain boundary microstructure.

Recently damascene structure have been developed to form Cu interconnect. Cu material is used to replace Al due to its higher electrical conduction. Because Cu has higher melting temperature, its diffusion mechanism is surface diffusion instead of grain boundary diffusion [20]. As for solder joints, because it has lower melting temperature, the diffusion mechanism is lattice diffusion for most solders at a typical operation temperature of an electronic device around 100°C. Table 1-1 lists the melting temperature of Al, Cu and SnPb solder, and their corresponding diffusion mechanism.

1.3.2 Current Crowding Effect

Within a metal line, as soon as the electromigration-induced damage forms, current density also becomes non-uniform. As voids or cracks grow, the non-uniformity of the current density over a conductor line increases. Since the Joule heating is proportional to the square of the current density, the local temperature will also increase rapidly. The current crowding effect therefore plays dual roles here: both the elevated local density and temperature accelerate the electromigration process. Thus obtaining an accurate current crowding density distribution is necessary in determining the flux divergence [20].

Current crowding phenomenon is an even more serious issue in flip chip solder joints. Figure 1-4(a) demonstrates the unique line to bump geometry of a flip chip solder bump joining an interconnect line on the chip side (top) and a conducting trace on the board side (bottom) [17,21,22,23]. Because the cross section of the line on the chip side is about two orders of magnitude smaller than that of a solder joint, the

current density changes significant from the metal line to the solder as current enters the solder joint. The change leads to the current crowding at the entrance into the solder bump, thus resulting in the change of magnitude of current density from 10^5 A/cm² to 10^4 A/cm² at the current crowding region in a typical Al line to solder bump structure. Figure 1-4(b) is a two-dimensional (2D) simulation of current distribution in a solder joint. Note that this current crowding phenomenon leads to non-uniform current distribution inside a solder joint. The current density at the current crowding region is one order of magnitude higher than the average current density at the center of the solder joint. Since the drift velocity is proportional to the current density and non-uniform temperature distribution inside a solder joint due to local Joule heating effect (see Section 1.3.3), electromigration-induced damage occurs near the contact between the on-chip line and the bump; voids formation for the bumps with electrons downward and hillock or whisker for the bumps with electrons upward. Therefore, current crowding effect plays a crucial role in the flip-chip solder joints under electromigration. Consequently, electromigration damage occurs near the contact between the line and the bump; voids induced from the damage can propagate along the interface due to the non-uniform current distribution [24].

In those flip chips using a thin film UBM, the current crowding leads to a pancake-type void across the entire cathode contact [25,26]. Figure 1-5(a) displays the SEM images of eutectic SnPb after electromigration [6,24] After aging for 40 hrs at 125°C and 2.25×10^4 A/cm², voids are seen in the left-upper corner since electron flow entered the bump from the upper-left corner of the joint. Similar phenomena were also observed in Sn-4.0Ag-0.5 Cu Pb-free solder joints as shown in Figure 1-5(b) [25]. Pancake-type void is clearly seen at the corner of flip-chip solder joints when the cathode is on the chip side. With current stressing time increases, pancake-type voids propagate across the top of solder joints, resulting in open failure. Later, the

re-distribution of current density and temperature due to void formation and propagation will be discussed.

1.3.3 Joule Heating Effect

When the current flow pass through a conductor, the heat generated due to the electrons vibrate the atoms in the conductor. This is so called Joule heating effect. The heating power can be describe as:

$$P = I^2R = j^2\rho V \quad (1-6)$$

where P is the heating power, I is the applied current, R is the resistance of the conductor, j is the current density, ρ is the resistivity of the conductor, and V is the volume of the conductor. Thus, the heating is controlled by two factors: first is the applied current, the other is the resistance of the conductor.

When the current to flip chip solder joint is relatively high, the whole system will generate a huge amount of heat resulting from the conducting traces and solder bumps. Generally, the total length of the Al trace can reach few meters, which the effective resistance is approximately few ohms. In contrast, the resistances of the solder bumps and the Cu trace at the substrate are relatively low, typically in the order of few or tens of milliohms. Therefore, the major contributor for Joule heating in flip chip joints comes from the Al trace [27-29]. As a result, the temperature in the bumps during accelerated testing is likely to be much higher than that of the ambient because of the Joule heating. Moreover, the current crowding effect will cause the local high current density; in other words, there will be a local Joule heating in the solder joints and resulted in a non-uniform temperature distribution. Chiu *et al* reported the “hot spot” exists inside the solder bumps at the current crowding region [29,30]. The combination of the Joule heating of Al interconnects on the chip side and the

non-uniform current distribution will lead to a temperature gradient across the solder joints. Consequently, Joule heating effect induced the increase in temperature in the flip-chip solder joints under electromigration significantly affects the analysis of failure time.

1.3.4 Mean-time to Failure

Electromigration requires a nonvanishing divergence of atomic flux. Since electromigration is cumulative, it affects the failure rate. In statistical study, the test samples should be stressed at the same current and temperature conditions. Then, the failure times or lifetimes can be recorded and plot by Weibull or normal distribution. In Weibull distribution, the time of 63.2% of reliability is denoted as the mean-time-to-failure (MTTF) [31]. In 1969, James R. Black explained the MTTF in the presence of electromigration is given by the equation [32]:

$$MTTF = A \frac{1}{j^n} \exp\left(\frac{Q}{kT}\right) \quad (1-5)$$

where A is a constant, j is the current density, n is a model parameter, Q is the activation energy, k is the Boltzmann's constant, and T is the average temperature. There are four of parameters: j , n , Q , and T need to be examined and analyzed. However, the current crowding effect and the Joule heating effect play important roles under electromigration in flip chip solder joints. To further consider about these two effect in MTTF analysis, the modified Black's equation becomes:

$$MTTF = A \frac{1}{(cj)^n} \exp\left[\frac{Q}{k(T+\Delta T)}\right] \quad (1-7)$$

by multiplying j with a crowding ratio c and adding to an increment of ΔT due to Joule heating [33]. For the following discussion, the estimated MTTF will be a key result to compare to each other.

1.4 Introduction of Thermomigration

Thermomigration is the flux of component in a solution induced by the temperature gradient. The phenomenon has also been called thermal diffusion. When a concentration gradient is established due to the impressed temperature, it is known as Ludwig-Soret Effect [26]. From the atomic point of view, temperature gradient can lead to the un-mixing of an initially homogenous alloy due to a biasing of the atomic jump [17]. Instead of electrical field, as in the case for electromigration, the effective driving force exerted by the temperature gradient is expressed as

$$F = \frac{Q^*}{T} \frac{dT}{dx} \quad (1-8)$$

where Q^* is the experimental determined parameter which describes the sign and magnitude of the thermo-transport effect. It is called the heat of transport of the component. Q^* has the positive in the flux equation when the flux is from hot to cold region. For situation in which one component is diffusing, e.g. an interstitial alloy, the flux equation is then given as [27, 39]

$$J = J_{chem} + J_{TM} = -D \frac{dC}{dx} - C \frac{D}{kT} \frac{Q^*}{T} \frac{dT}{dx} \quad (1-9)$$

D/kT is the mobility of the diffusing component, and dC/dx is the concentration gradient at constant temperature. Note that D is the diffusion coefficient. The temperature gradient does not change the jump mechanism or mean jump frequency at any given temperature. However, it biases the direction of jump.

1.4.1 Measurement of the Heat of Transport

Q^* can be obtained by two methods. First method is to allow flux to go to zero in a temperature gradient and measure the concentration gradient at $J=0$. Second method is to measure the flux through an open system at a known temperature gradient.

Figure 1-6 demonstrates the concentration of carbon content in an initially single-phase alloy (0.01%C) under a temperature gradient until a steady state was established. Note the final concentration gradient across the specimen is a linearly relationship with temperature and concentration becomes higher at the hot end. With the flux equals to zero, equation (1-9) becomes

$$\frac{d \ln C_1}{dx} = - \frac{Q_1^*}{RT^2} \frac{dT}{dx} \quad (1-10)$$

The method allows Q^* to be obtained from the slope of the curve without any information on the diffusion coefficient. In the case if the α -Fe shown in Figure 1-6, $Q_c^* = -96$ kJ/mol. It means carbon moves toward the hot end.

In pure metal diffusion occurs by the motion of vacancies so the flux of atom is highly affected by the change in the equilibrium vacancy with temperature. The flux of the element under a temperature gradient can be expressed as

$$J = - \frac{D_A}{\Omega} \frac{(Q_A^* - H_v)}{RT^2} \frac{\partial T}{\partial x} \quad (1-11)$$

Where Ω is atomic volume and H_v is the enthalpy of formation of vacancies. Q_A^* is heat of transport for element A. Experiments have been done by heating one end of pure metal and cooling the other end or by heating the center of a sample by passing an electric current through it and keeping the end cold. The net flux of atom is then measured by motion of inert marker relative to the end of the sample. Table 1-2 [34] lists the experimental values of Q_A^* for several pure metals. All the values for H_v are invariable larger than Q_A^* so the vacancy concentration gradient dominates and the net flux of vacancies is always toward the cold end. As a result, more vacant sites at the hot end allow atoms to jump into on its higher temperature side than on its lower temperature site. An increase in the distance between markers in the hottest parts of the sample is observed [17]. Since the effect of Q_A^* is small relative to the vacancy gradient effect, Q_A^* cannot be measured with much accuracy. The situation becomes

even more complex when it becomes binary alloys. Whether one element becomes enriched at the hot end or cold end of the sample is determined by the competition between the flows of the two elements relative to the lattice under the temperature gradient.

1.4.2 Thermomigration Accompanying Electromigration in Flip Chip Solder

Joints

Thermomigration has been reported to accompany electromigration on flip chip solder joint recently [35,36]. The major heat source exerted on solder joint is from Al trace on the Si die side. Longer electric current path and high current density in Al trace increase the temperature of the Si chip tremendously. As a result, a temperature gradient existed across solder joints and thermomigration can occur along with electromigration. Figures 1-7(a) and (b) show the SEM pictures of an example of a pair of eutectic SnPb solder joint after current stressing. The sample was finely polished and to half of the bump before the testing. Figure 1-7(a) shows the formation of the voids on the chip side and accumulation of solder on the substrate side for the solder bump with downward electron flow. However as shown in Figure 1-7(b), for the solder bump with upward electron flow, voids was also observed on the chip side. This phenomenon cannot be explained by electromigration since the atomic movement is against electron flow on the chip side. It is due to the competing effect of electromigration and thermomigration, as further prove by the marker movement. From temperature measurement and simulation, it was estimated that a temperature gradient of 15°C generated across a solder joint of 100 μm in diameter, and the temperature gradient of 1500°C /cm seems sufficient to cause thermomigration in eutectic SnPb solder joints.

1.4.3 Thermomigration in Composite SnPb Flip Chip Solder Joints

The combination effect of electromigration and thermomigration was observed for powered bump. However, thermomigration in unpowered bump has not been obtained much attention before. Indeed, when the electronic device is large and thermal dissipation is sufficient on the Si chip, signal bump or unpowered bump has minimal thermal effect. When the electronic device becomes smaller and bump pitch becomes closer, thermal effect from powered bump can no longer be neglect.

To induce thermomigration in the composite solder joints, we used the temperature gradient induced by Joule heating in electromigration test. A set of flip chip samples is depicted in Figure 1-8(a) [37], wherein there are 24 bumps on the periphery of a Si chip, and all the bumps had their original microstructure, as shown in Figure 1-8(b), before electromigration stressing. After electromigration was conducted through only four pairs of bumps—pairs 6/7, 10/11, 14/15, and 18/19 in Figure 1-9(a), thermomigration affected all the unpowered solder joints, as shown in Figure 1-9(b). All the Sn (the darker image) migrated to the hot Si side, whereas the Pb migrated to the cold substrate side. The redistribution of Sn and Pb was caused by the temperature gradient across the solder joints because no current was applied to them. Since Si has a very good thermal conductivity, the Joule heating of Al interconnects on the chip side of the four pairs of powered bumps has heated the entire Si chip to induce a temperature gradient and in turn the TM across all the unpowered bumps.

1.4.4 Thermomigration in Pb-free Flip Chip Solder Joints

Hsiao et al.[38] performed thermomigration by operating with alternating current (AC) and direct current (DC). The advantage of AC is that there would be no electromigration under AC, and this will be a good way to decouple electromigration

and thermomigration. The schematic diagram of a Pb-free solder bump used in thermomigration study is shown in Figure 1-10(a). After 800 hrs of 1.01×10^4 A/cm² current stressing at 100 °C, hillocks are present on the chip side, as shown in Figure 1-10(b). The hillocks are formed by the mass transfer in the solder bump caused by thermomigration and comprised of Sn using a SEM energy dispersive spectroscopy (EDS). This result reveals that Sn atoms are driven from cold side to the hot side under TM.

Moreover, what is worth noting is during electromigration test which will couple with thermomigration, not only solder (Sn or Pb) will affect but also UBMs. The dissolution of Cu and Ni in Pb-free solders is quite high, and the diffusion of Cu and Ni in Sn is anisotropic and very fast. The diffusion rate along the c-axis of Sn crystals is faster than that in the a- and b-axis. The dissolution of Cu and Ni atoms may occur under a thermal gradient [39]. Figure 1-11(a) shows a eutectic SnAg solder bump with a 5- μ m UBM on the chip side before a TM test. This bump was next to a bump that was under EM stressing at 0.55 A and 150 °C. This joint had no current passing through it but possessed a thermal gradient of 1143 °C/cm, as illustrated in Figure 1-11(b). After 60 h of the TM test, the Cu-Sn IMC migrated to the cold (substrate) end, as shown in Figure 1-11(c). Although this bump was un-powered, the damage is clear near the upper left corner, as indicated in Figure 1-11(c). The Cu UBM dissolved almost completely into the solder. This dissolution can be attributed to the TM of Cu atoms by fast interstitial diffusion and the reaction with Sn atoms to form Cu-Sn IMCs inside the solder bump.

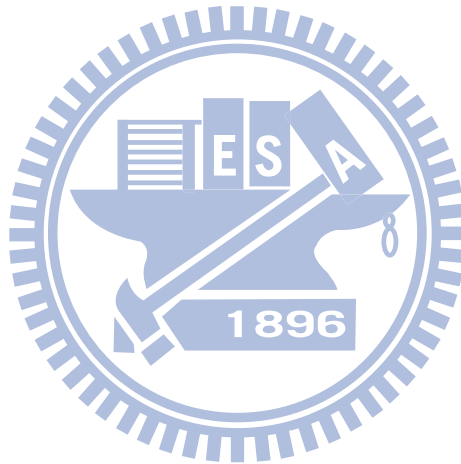
1.5 Summary

In this thesis, we study the effect of thermomigration with and without DC stressing ex-situ. When the system is under both electromigration and

thermomigration, the overall flux can be expressed in terms of chemical force, electrical force and thermal gradient as followed.

$$J = -D \frac{dc}{dx} + C \frac{D}{kT} eEZ^* - C \frac{D}{kT^2} \frac{dT}{dx} \quad (1-12)$$

Detailed discussion on the contribution of each term will be reported in later chapter.



1.6 References

1. J. H. Lau, "*Flip Chip Technology*" (McGraw-Hill, New York, 1995), p.123.
2. E. M. Davis, W. E. Harding, R. S. Schwartz, and J. J. Corning, Solid logic technology: versatile, high performance microelectronics, *IBM J. Res. Develop.* 44, 56 (2000).
3. L. R. Miller, Controlled collapse reflow chip joining, *IBM J. Res. Develop.*, 239 (1969).
4. P. A. Totta and R. P. Sopher, SLT device metallurgy and its monolithic extensions, *IBM J. Res. Develop* 13 (1969).
5. K. Puttlitz and P. A. Totta, "*Area Array Interconnection Handbook*" (Kluwer Academic, Boston, MA, 2001).
6. K. Zeng and K.N. Tu, *Mater. Sci. Eng. R.* **38**, 55 (2002).
7. A. Sharif and Y.C. Chan, *Mater. Sci. Eng. B.* **106**, 126 (2004) .
8. J.W. Yoon, S.W. Kim and S.B. Jung, *Mater. Trans.* **45**, 727 (2004).
9. K. Suganuma, *Curr. Opin. Solid State Mater. Sci.* **5**, 55 (2001).
10. S. K. Kang and V. Ramachandran, *Scripta Mat.* **14**, 421 (1980).
11. M. O. Alam, Y. C. Chan and K. C. Hung, *J. Electron. Mater.* **31**, 1117 (2002).
12. K.H. Prakash and T. Sritharan, *J. Electron. Mater.* **32**, 939 (2003).
13. K. N. Tu and K. Zeng, *Mater. Sci. and Eng. R* **34**, 1 (2001).
14. J. W. Yoon, C. B. Lee and S. B. Jung, *J. Electron. Mater.* **32**, 1195 (2003).
15. W. G. Bader, *Weld. J. Res. Suppl.* **28**, 551 (1969)
16. K. N. Tu, *J. Appl. Phys.* **94**(9), 5451 (2003)
17. P. G. Shewmon, "Diffusion in Solids" (TMS, Warrendale, PA 1989), Chapter 7.
18. K. W. Moon, W. J. Boettinger, U. R. Kattner, F. S. Biancaniello, and C. A. Handwerker, *J. Electron. Mater.* **29**, 1122 (2000)
19. M. E. Looms and M. E. Fine, *Metall. Mater. Trans. A* **31A**, 1155 (2000)

20. Christou, "Electromigration and electronic device degradation" Wiley, New York (1994)
21. Q. T. Huynh, C. Y. Liu, C. Chen and K. N. Tu, J. Appl. Phys. **89**, 4332 (2000)
22. J. W. Jang, C. Y. Liu, P. G. Kim, K. N. Tu, A. K. Mal and D. R. Frear, J. Mater. Res. **15** 1679 (2000)
23. Y. Guo, W. T. Chen and C. K. Lim, Proceedings of the ASME Conference in Electronic Packaging, San Jose, CA, 1992, p. 199
24. Everett C. C. Yeh, W. J. Choi, K. N. Tu, P. Elenius, H. Balkan, Appl. Phys. Lett. **80**(4), 580 (2002)
25. L. Y. Zhang, S. Q. Ou, J. Huang, K. N. Tu, S. Gee, and L. Nguyen, Appl. Phys. Lett. **88**, 012106 (2006)
26. R. A. Oriani, J. Phys. Chem. Solids **30**, 339 (1969)
27. H. Ye, C. Basaran, and D. Hopkins, Appl. Phys. Lett. **82**(7), 1045 (2003).
28. T. L. Shao, S. H. Chiu, Chih Chen, D. J. Yao, and C. Y. Hsu, J. Electron. Mater. **33**, 1350 (2004).
29. S. H. Chiu, T. L. Shao, Chih Chen, D. J. Yao, and C. Y. Hsu, Appl. Phys. Lett. **88**, 022110 (2006).
30. S. H. Chiu, Thesis, National Chiao Tung University, 2007
31. 何輝耀, 可靠度保證-工程與管理技術之應用: 中華民國品質學會發行
32. J. R. Black, IEEE Trans. Electron Devices ED 16, 338 (1969).
33. W. J. Choi, E. C. C. Yeh, and K. N. Tu, J. Appl. Phys. **94**, 5665 (2003).
34. Hans Wever, Elektro u. Thermo-transport in Metallen, J. A. Barth, Leipzig (1973)
35. H. Ye, C. Basaran and D. C. Hopkins, Appl. Phys. Lett. **82**, 1045 (2003)
36. C. Basaran, H. Ye, D. C. Hopkins, D. R. Frear and J. K. Lin, J. Electronic Packaging, **27**, 157 (2005)
37. Annie Huang, A. M. Gusak, K. N. Tu, and Yi-Shao Lai, Appl. Phys. Lett., **88**,

141911 (2006).

38. H. Y. Hsiao and C. Chen, Appl. Phys. Lett., **94**, 092107 (2009)

39. H. Y. Chen, C. Chen, K. N. Tu, Appl. Phys. Lett. **93**,122103 (2008)



Table 1-1 Melting temperature, diffusivity and diffusion mechanism for Cu, Al, Pb and SnPb solder.

	Melting point (°K)	Temperature ratio 373°K/T _m	Diffusivities at 100°C [373°K] (cm ² /sec)
Cu	1356	0.275	Surface $D_s=10^{-12}$
Al	933	0.4	Grain Boundary $D_{gb}=6 \times 10^{-11}$
Pb	600	0.62	Lattice $D_l=6 \times 10^{-13}$
Eutectic SnPb	456	0.82	Lattice $D_l=2 \times 10^{-9}$ to 2×10^{-10}

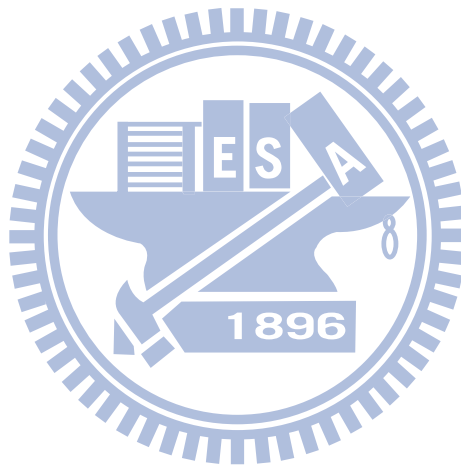


Table 1-2 Experimental values of Q_A^* for some pure metals.

Q^* in Pure Metals			
Metal	H_m (kJ)	H_v (kJ)	Q^* (kJ)
Ag	81	97	0
Au	86	84	-25
Al	60	63	7
Pb	60	49	9
Pt	132	153	65

Hans Wever, *Elektro- u. Thermo-transport in Metallen*, J. A. Barth, Leipzig (1973), p. 216.



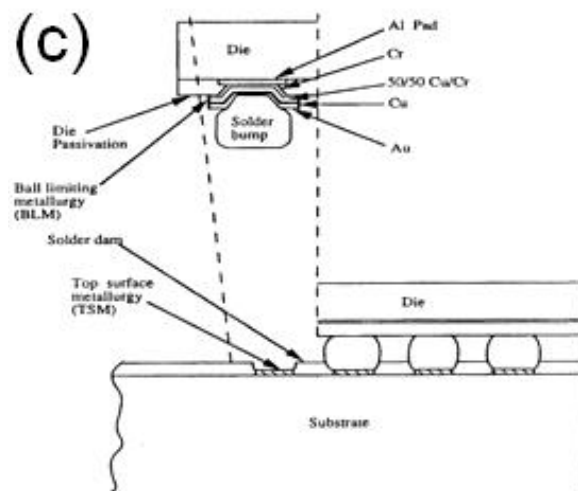
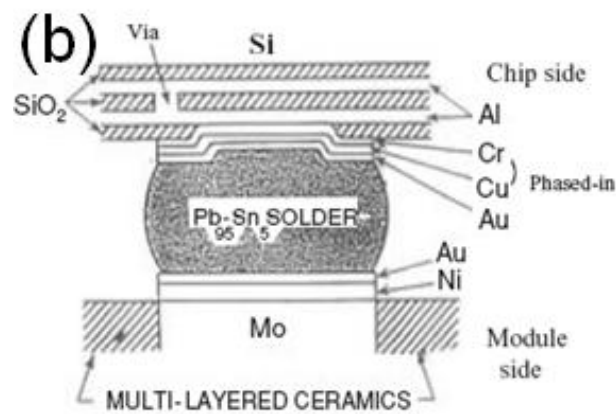
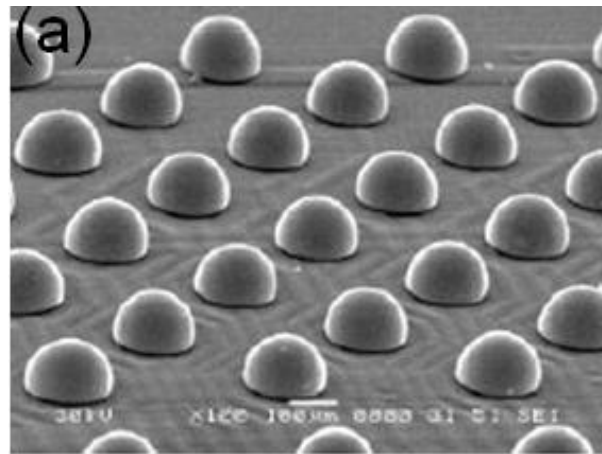


Figure 1-1 (a) Tilt-view of SEM image of arrays of solder bumps on silicon die. (b) A flip-chip solder joint to connect the chip side and the module side. (c) The chip is placed upside down (flip chip), and all the joints are formed simultaneously between chip and substrate by reflow.

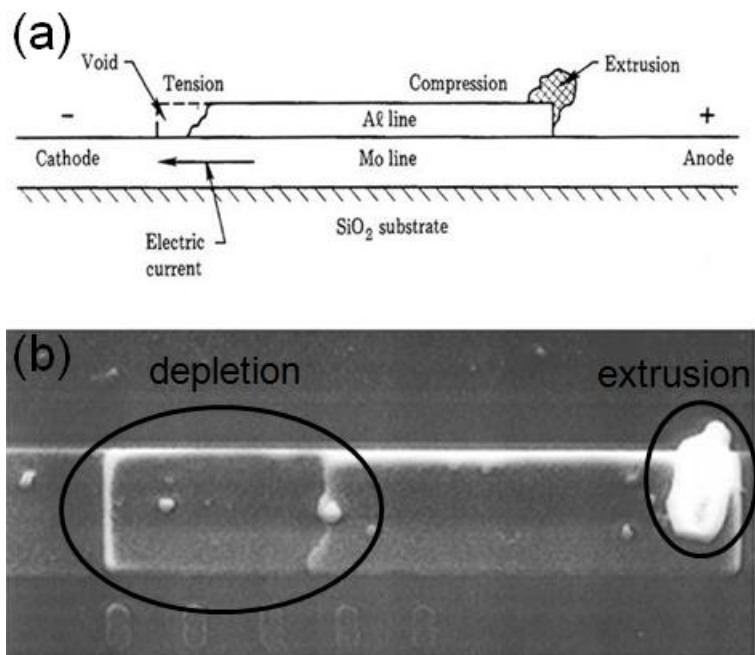


Figure 1-2 (a) Blech's pioneering electromigration sample, showing an aluminum strip deposited on a conducting TiN layer. (b) SEM images of the morphology of a Cu strip tested for 99 hrs at 350°C with current density of 5×10^5 A/cm².

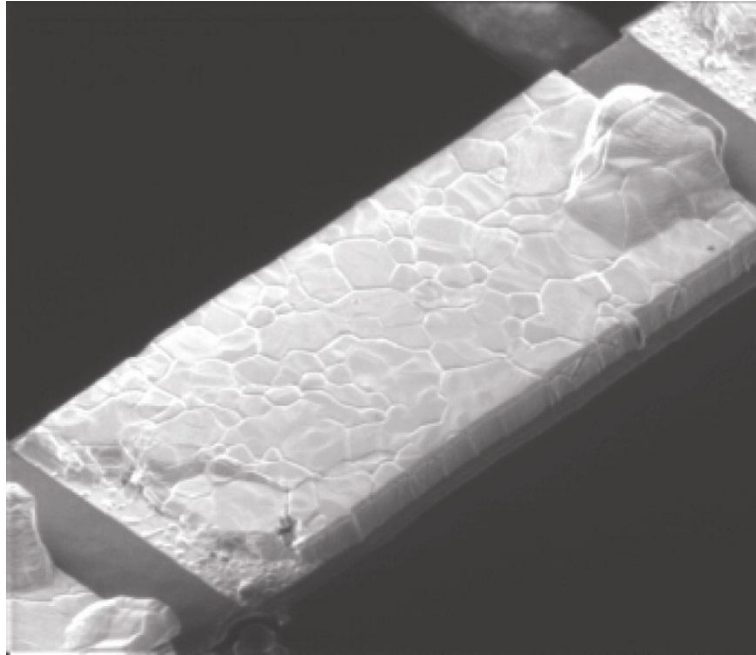
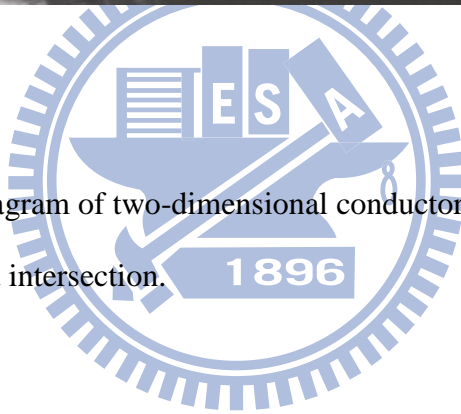


Figure 1-3 Schematic diagram of two-dimensional conductor film with grain boundary and intersection.



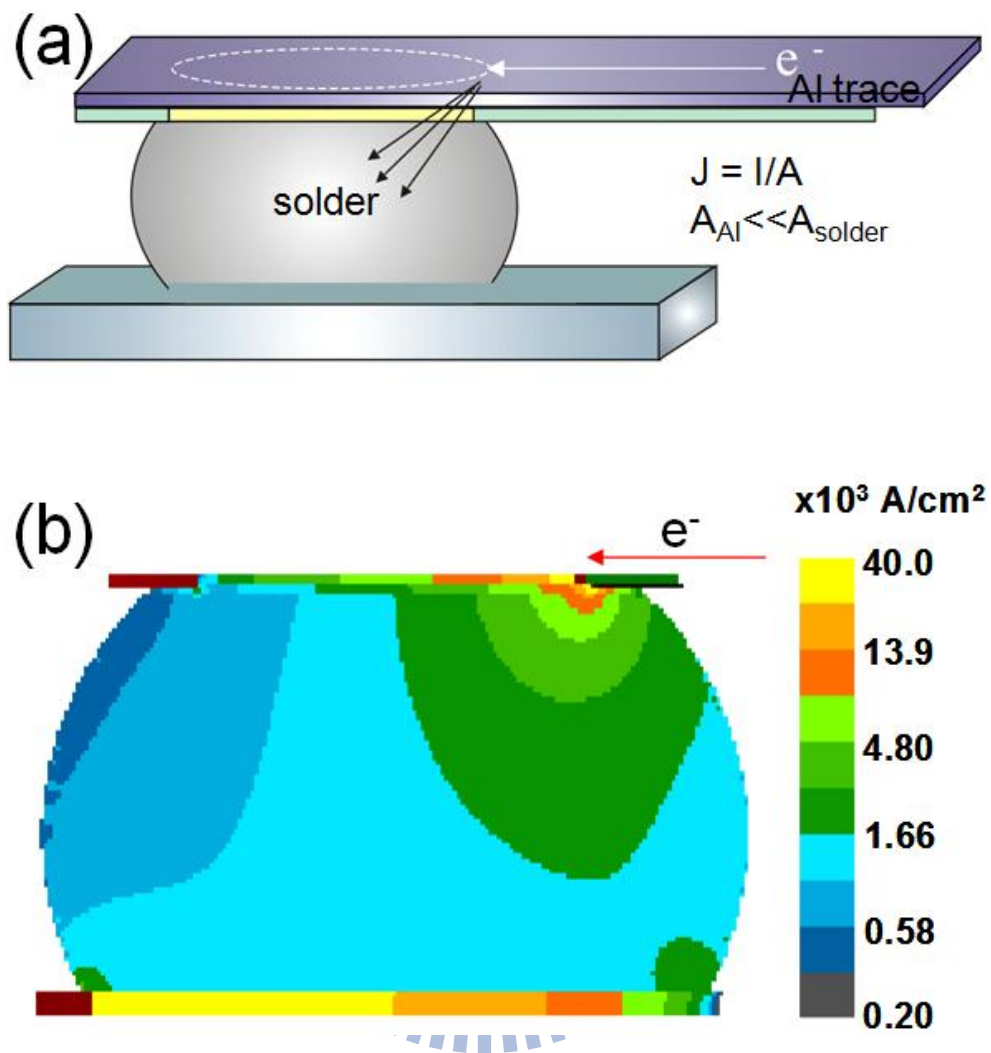


Figure 1-4 (a) Unique line to bump geometry of a flip chip solder bump joining in a interconnect line on the chip side (top) and a conducting trace on the board side (bottom) and (b) two-dimensional (2D) simulation of current distribution in a solder joint.

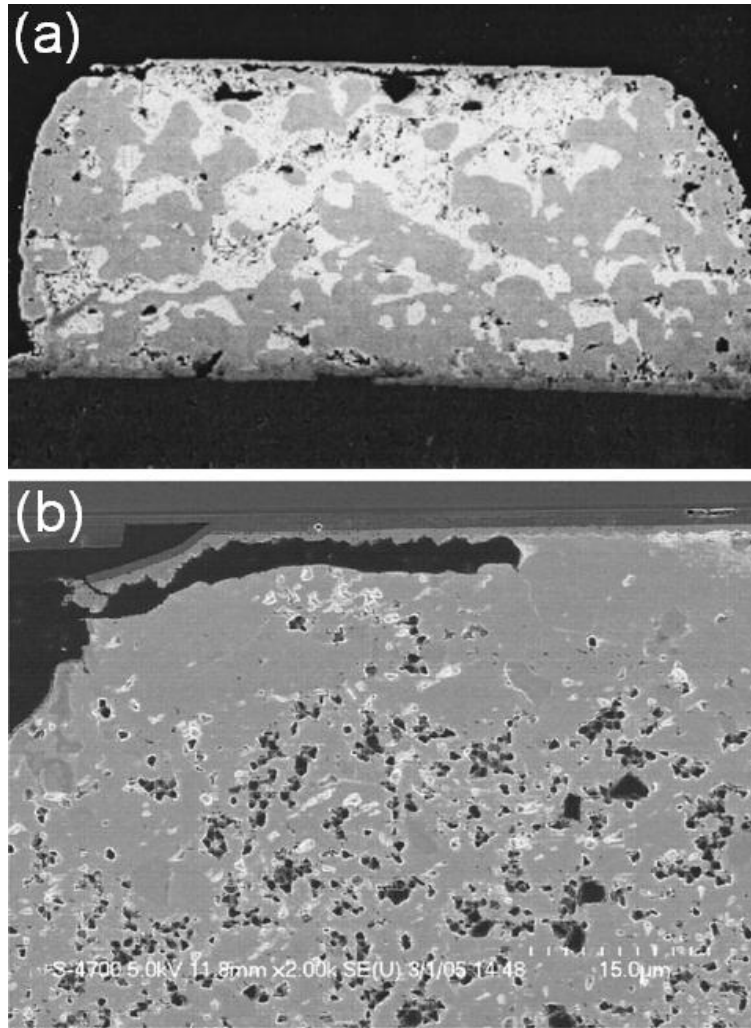


Figure 1-5 (a) SEM images of a sequence of void formation and propagation in a flip-chip eutectic SnPb solder bump stressed at 125 °C at 2.25×10^4 A/cm² for 40 h. (b) SEM image of void formation in flip-chip 95.5Sn-4.0Ag-0.5Cu solder bump at 146 °C at 3.67×10^3 A/cm².

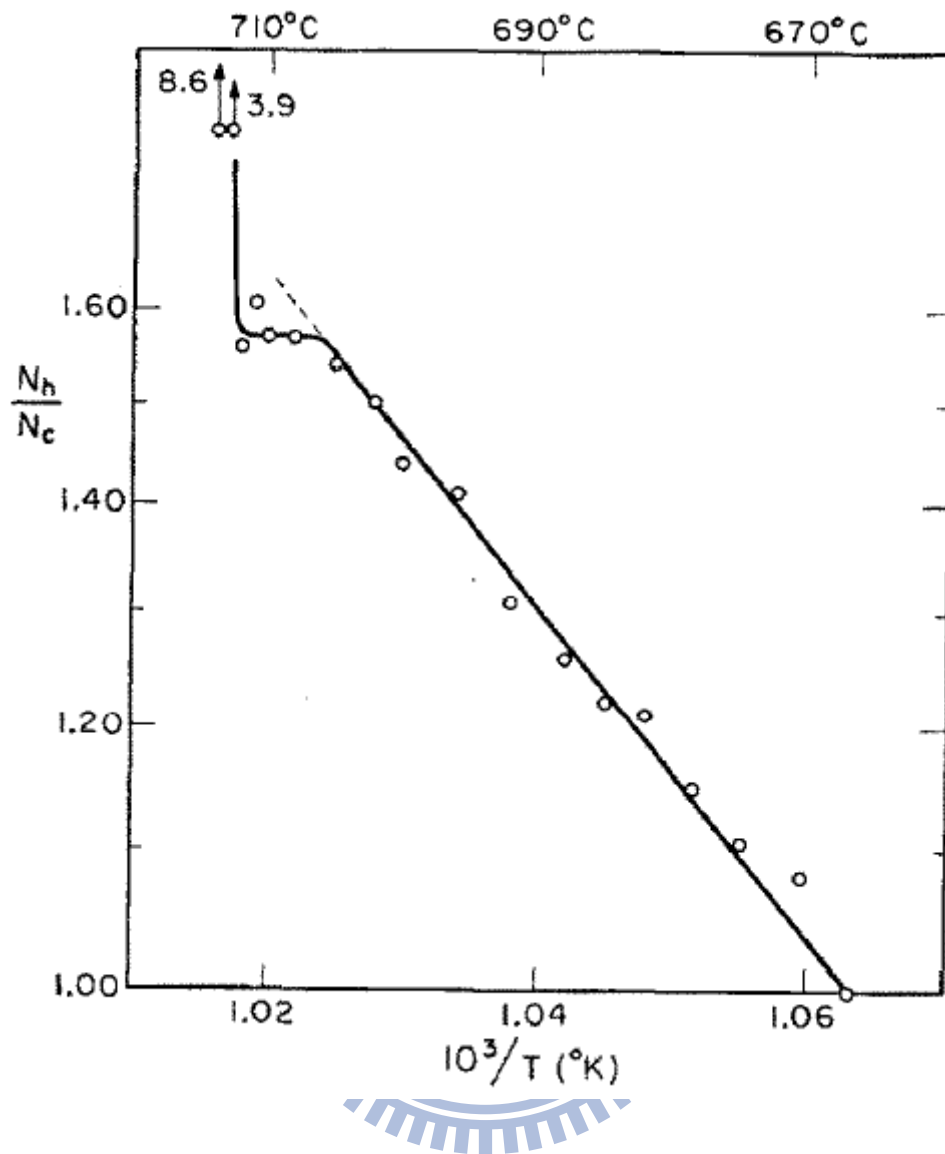


Figure 1-6 Plot of Carbon content (logarithmic scale) vs. 1/T for sectioned alpha iron specimen.

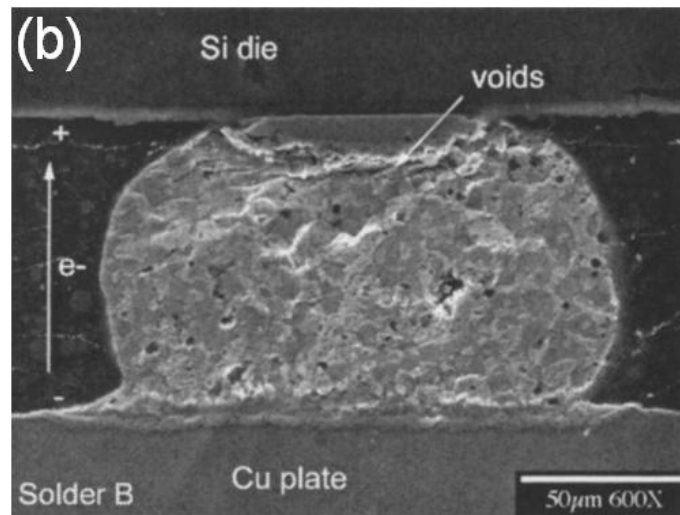
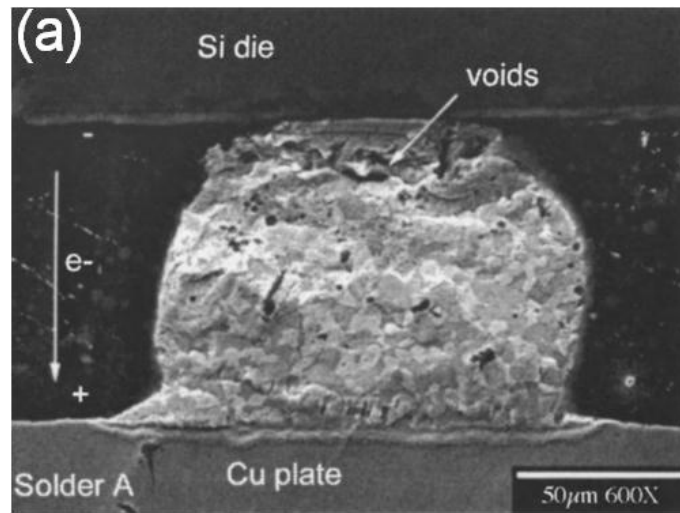


Figure 1-7 The formation of voids on the chip side and accumulation of solder on the substrate side for the solder bump with (a) downward flow and (b) upward electron flow.

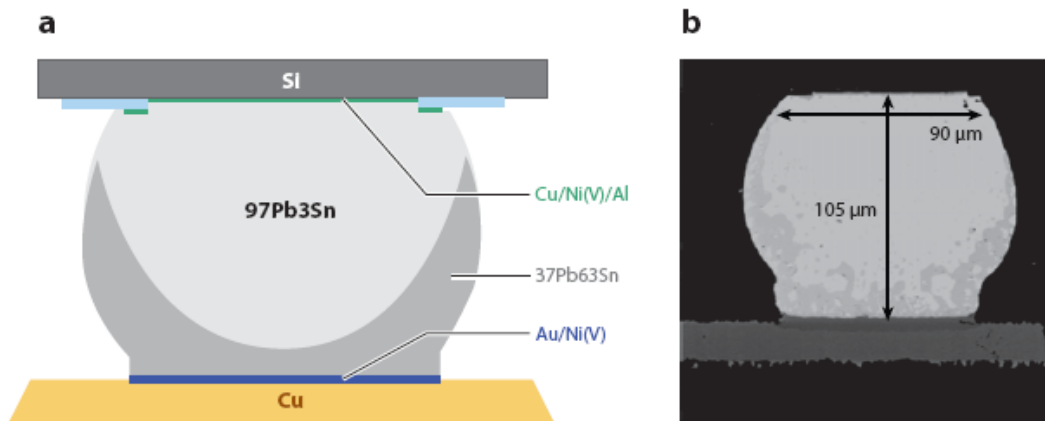
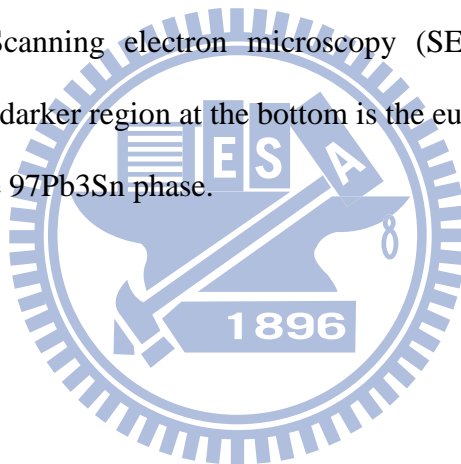


Figure 1-8 (a) A cross section of a composite 97Pb3Sn and 37Pb63Sn flip-chip solder joint. (b) Scanning electron microscopy (SEM) image of the cross section. The darker region at the bottom is the eutectic SnPb. The brighter region is the 97Pb3Sn phase.



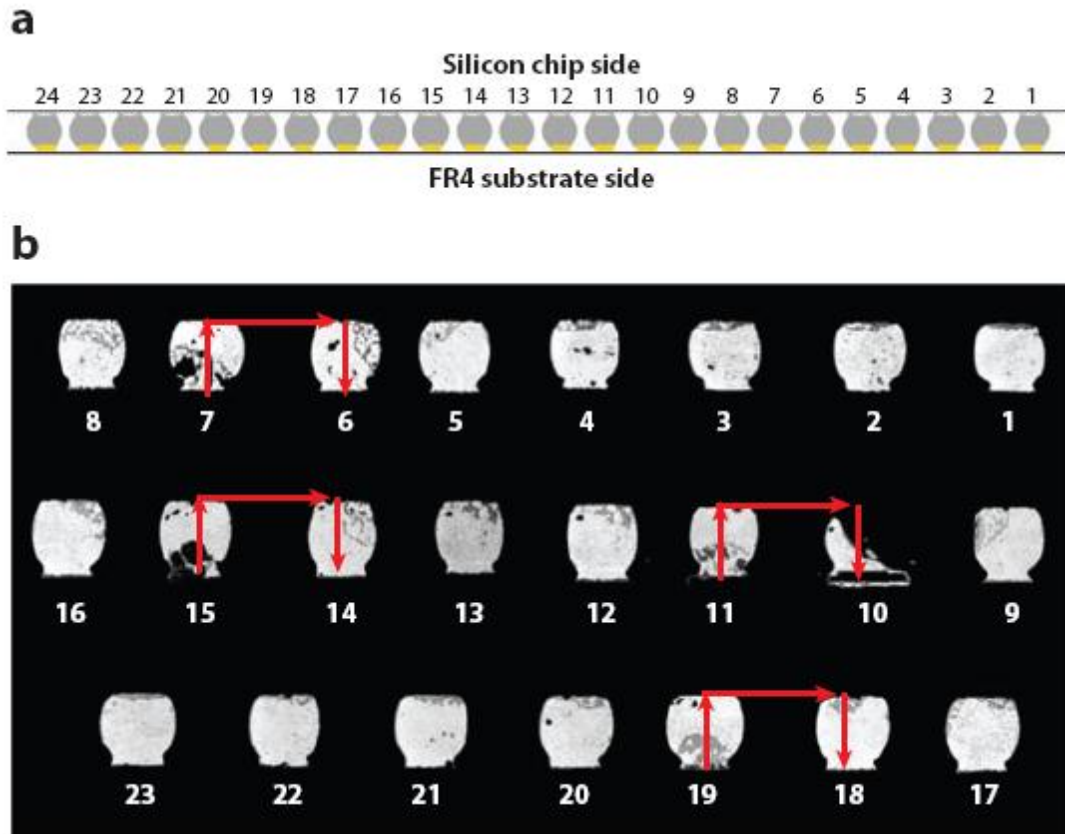


Figure 1-9 (a) Schematic diagram depicting 24 bumps on the periphery of a Si chip.

Each bump has its original microstructure, as shown in Figure 4(b), before EM stressing. EM was conducted at $1.6 \times 10^4 \text{ A/cm}^2$ at 150°C through only four pairs of bumps on the chip's periphery: pairs 6/7, 10/11, 14/15, and 18/19. (b) TM affected all the un-powered solder joints: The darker eutectic phase moved to the hot Si side.

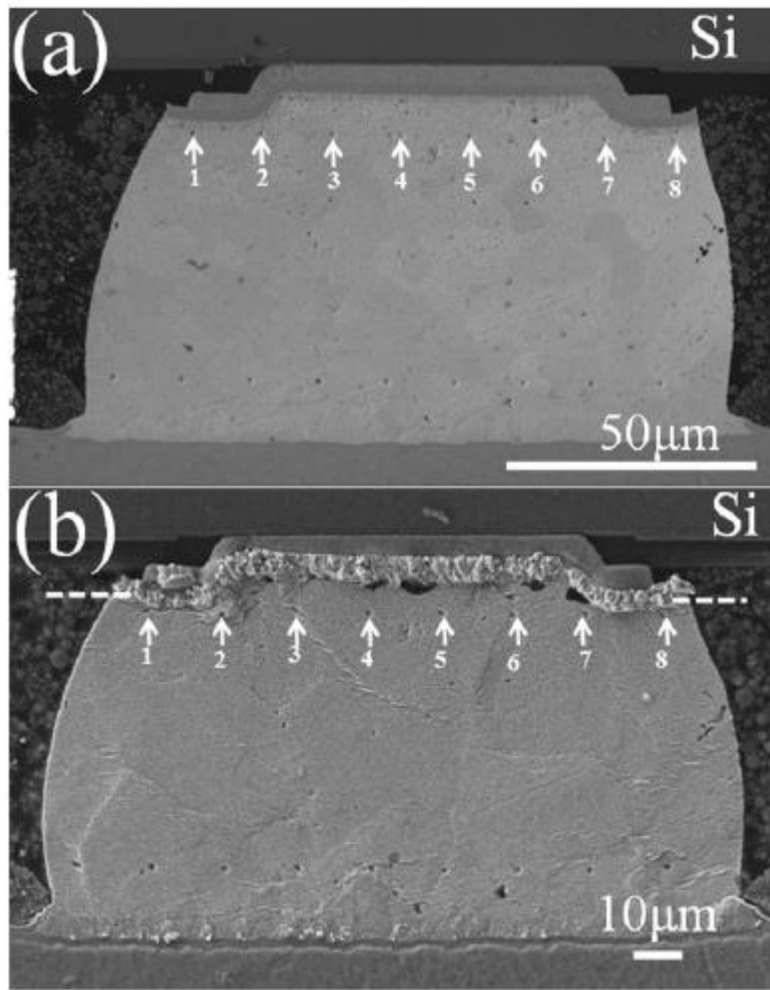


Figure 1-10 SEM images of cross-sectioned bump with markers before and after TM test at $1.01 \times 10^4 \text{ A/cm}^2$ and 100°C . (a) Before TM, and (b) After 800 hrs of the TM test. The markers moved toward the substrate end.

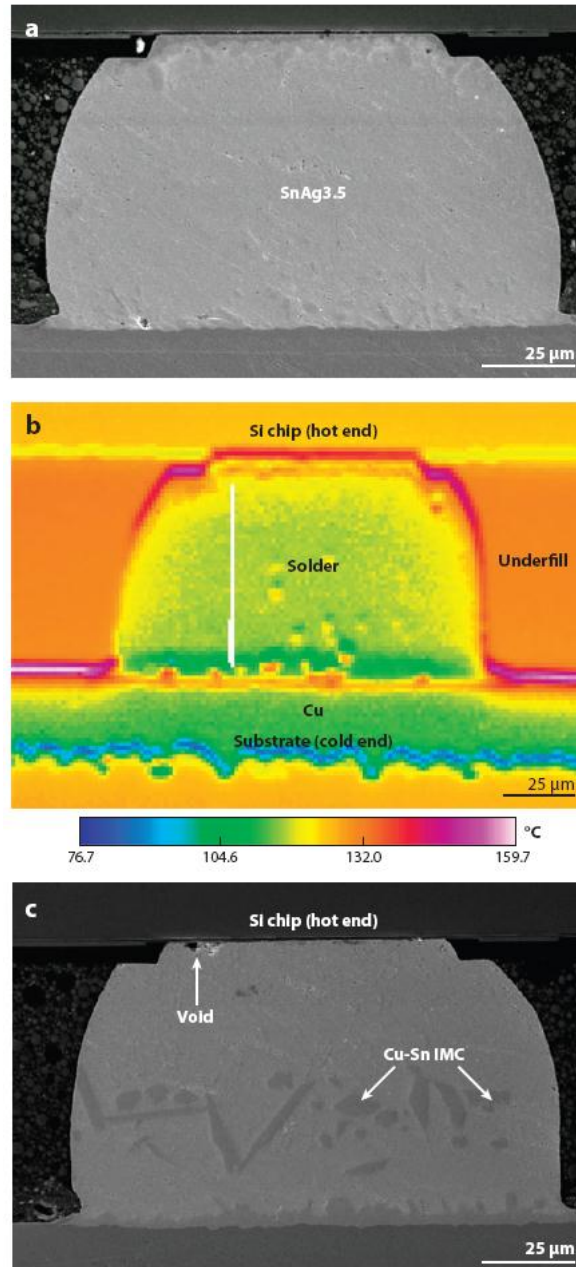


Figure 1-11 (a) Cross-sectional SEM images representing the microstructure for an un-powered bump before a thermomigration test. (b) Temperature distribution measured by an infrared microscope when the neighboring bumps were stressed by 0.55A at 150 $^{\circ}\text{C}$. The built-in thermal gradient was 1143 $^{\circ}\text{C}/\text{cm}$ across the solder bump. (c) After the TM test for 60 hrs. The Cu UBM was dissolved.

Chapter 2 Kinetic study of the Intermetallic Compound Formation of Eutectic SnAg an Eutectic SnPb Solder with Electroplated Ni Metallization in Flip-chip Solder Joints

2.1 Introduction

Solder bumps in flip-chip technology have been adopted in microelectronic industry as interconnections due to their excellent performance in electrical performance, thermal dissipation, and reliability [1]. A reliable solder joint can be formed by a metallurgical reaction between molten solders and UBMs on a chip or metallization on the substrate, which produces stable IMCs at the joint interfaces [2]. During the soldering process, the formation of IMCs between solder alloys and the metallization layer is inevitable. The growth of these IMCs can strongly affect the mechanical reliability of the solder joints [3-5]. As the result, selection of appropriate UBM plays an important role in developing a reliable flip chip joint, especially so with the adoption of the Pb-free solders due to environmental concerns. A typical issue encountered for Pb-free adoption implement is that these Sn-based Pb-free solders were found incompatible with traditional Cu-based metallization due to rapid reaction and spalling of Cu-Sn IMC [6,7]. Instead, Ni-based UBM, such as electroless Ni-P alloy and pure Ni, have attracted great attention in recent years because of their good wettability [8], good diffusion barrier ability and slow reaction rate with solders [5,9]. Many studies have been published on the interaction between Ni-P and Sn-based solders [10-21]. They investigated the formation and growth of IMCs at the interface of molten solder and Ni-P UBM, solder reaction-assisted crystallization of Ni-P alloy, and the influences of the IMCs on the mechanical properties of the solder

joints. The Ni-P metallization has been found to be a main issue for the interface strength, since voids form at the interface, and the IMCs detach easily after a longer reaction time.

Most of previous works are mainly focused on solder/Ni-P reaction. However, a few studies have been done on the interfacial reaction between molten solder and electroplated Ni [18,22-26]. Recently, electroplated-Ni (EP-Ni) thick-film has been adopted as the UBM structure due to its lower resistivity and higher deposition rate. The resistivity of electroless-Ni(P) alloy may be over 100 $\mu\Omega\text{-cm}$ when the content of phosphorous reaches 12% or higher, since the Pb-free solders have a higher reaction during reflowing process, thus the thickness of the Ni(P) layer is over 10 μm in general, causing a much higher bump resistance. On the contrary, the electroplated-Ni has much lower resistivity of 6.8 $\mu\Omega\text{-cm}$. Therefore it has been adopted as a UBM material. The interfacial reactions between eutectic SnPb solder and Ni foil has been studied [9]. Few studies have been done on the interfacial reactions between SnAg solder and electroplated-Ni [27,28]. However, the metallurgical reactions between eutectic SnPb and eutectic SnAg solders and EP-Ni has not been investigated in details in real solder joints [22,26]. In particular, the consumption rate of the electroplated Ni film, as well as the activation energy of IMC formation is still worth noticing.

In this chapter, interfacial reactions between eutectic SnPb and SnAg solders and EP-Ni have been investigated. The Ni consumption rate, IMC growth rate, and activation energy for the interfacial reaction have been determined. In addition, the interfacial reactions between the solders and electroless Ni(P) (EL-Ni) were also studied in the same time. Thus, this work provides the direct comparisons of soldering reaction between the two interfaces in the flip chip scale samples.

2.2 Experimental Procedures

In order to examine the interfacial reaction and the effect of reaction on the mechanical properties, two types of specimens were used. Figures 2-1(a) and 2-1(b) show the flip-chip sample of SnAg and SnPb for the interfacial reaction study respectively; whereas bumped-die sample is adopted to facilitate the shear test on the solder bump as shown in Figure 2-1(c). On the chip side for both samples, Ti of 0.1 μm was sputtered onto the oxidized Si wafer to serve as the adhesion layer. 0.5 μm thick Cu was then sputtered on the Ti layer and served as a seed layer for the subsequent electroplating process. Then the Cu or Ni layer was electroplated on the Ti/Cu layers. Photolithography was applied to define the contact opening on the chip-side for solder electroplating of eutectic SnAg solder. The solder bumps were formed by reflowing in an infrared oven at 260°C for 1 min. For flip-chip package samples, the bumped dies were then mounted to a FR5 substrate. The pad metallization on the substrate side was 5 μm electroless Ni on the 30 μm thick Cu lines. The solder bumps experienced another reflow during the mounting process. For metallurgical reactions at the liquid-state reactions for SnAg solders, flip-chip samples were reflowed at 230, 240, 250 and 260°C for 5, 10, 15 and 20 min, while bumped-die samples were reflowed for 1, 5 and 10 times, in which for 1 min per time. On the other hand, SnPb samples were reflowed at 200, 210, 220°C and 240°C on a hot plate for 5 min, 10 min, 1 hr, 4 hrs, 6.25hrs and 9 hrs respectively. The Si side was placed on the hot plate, so that the temperature in solder was close to the temperature on the hot plate. The microstructure of the interfacial regions between the solders and the Ni-based UBM were examined by a scanning electron microscope (SEM, JEOL 6500). A backscattered electron image (BEI) of SEM was used to examine the morphology of the cross-sectioned SnAg samples. The compositions of the solder joints and the IMC were analyzed semi-quantitatively by energy dispersive

spectroscopy (EDX) and an electron probe microanalyzer (EPMA, JXA-8800M, JEOL). To facilitate the observation of the interfacial IMC layer, a solution of nitric acid and acetone at the ratio of 49:1 was used for the selective etching of Sn. The thickness of the IMC was calculated by commercial software “Matrox Inspector”. To obtain the average IMC thickness, six bumps were measured for each condition. Each IMC thickness was averaged after 25 times of each bump from software in order to reduce the artificial deviations.

2.3 Results and Discussion

2.3.1 Growth of IMC and Ni Consumption Rates

(i) SnAg Solder Samples

The flip-chip samples provide a direct comparison between the EP-Ni/solder and EL-Ni/solder interface. Figure 2-2(a) shows the cross-sectional SEM image for the as-fabricated flip-chip samples; two interfaces can be noted here, the EP-Ni/solder interface located on the chip side and the other substrate side interface. The bump height is about 75 μm . The enlarged SEM images for the two interfaces are illustrated in Figures 2-2(b) and 2-2(c), respectively. Due to the fabrication processes described in the experimental section, the EP-Ni/solder interface of past through two-times reflows, which corresponds to two-minute duration of liquid-state reaction. On the other hand, the interface of EL-Ni/solder only experienced one-minute liquid-state reaction. Two different types of the IMC morphology can be observed from these two systems. The IMCs on the two interfaces were both identified to be Ni_3S_4 . Column-type IMCs are observed on the EP-Ni surface, whereas needle-type IMC formed on the EL-Ni surface. The height of the column-type IMC is more uniform than that of the needle-type IMC.

As showed in Figures 2-2(b) and 2-2(c), the IMC grown on the EP-Ni/solder interface was measured to be 0.94 μm , which is thinner than that grown on the EL-Ni/solder interface (1.31 μm). This thinner layer indicates the initial IMC growth rate is slower on the EP-Ni side. Since the EP-Ni/solder experienced one more minute reflow than the EL-Ni/solder interface, the IMC formation rate at the EP-Ni side is about 1.4 times slower than that at the EL-Ni side. The bumped-die samples were employed to measure the IMC growth rate and EP-Ni consumption rate at typical reflow temperature, 260°C for eutectic SnAg solders. Figure 2-3(a) shows a cross-sectional SEM image for the as-fabricated and one reflow processed SnAg bumps on EP-Ni UBM, and the enlarged area is shown in Figures 2-3(b) and 2-3(c). After reflowed for 10 times, the growing thicker column-type IMC still attached well with EP-Ni UBM.

In order to accurately consider the EP-Ni reliability, we repeat the reflow processes for the same sample for ten times. 2.2 μm remained EP-Ni layer still attached well as shown in Figures 2-4(a) and 2-4(b). Only about 0.8 μm of EP-Ni was consumed after reflowed process and 2.6 μm IMC is obtained to bond solder/UBM interface. The estimated consumption rate of EP-Ni is $1.33 \times 10^{-3} \mu\text{m}/\text{sec}$ under this reflow condition within 10 minutes. For flip-chip samples, the variation of average IMC thicknesses with temperature and time are listed in Table 2-1. The corresponding SEM images of IMC thickness variation with time and temperature are shown from Figures 2-5(a) to 2-5(c). From 5 min to 20 min reflow durations, IMC at EP-Ni side remained column-type and indicated that the grains grew in a thickening process with a rough surface toward the liquid solder. From the EDX analysis, all IMCs are Ni_3Sn_4 and there is residual EP-Ni in between IMC and Cu UBM. In other words, IMC attached very well at the interface. On the other hand, the IMC at the EL-Ni side was also defined as Ni_3Sn_4 but their morphology was more likely the chunk-type or

layer-type as time increased. Moreover, as reflow duration increased, IMC grew thicker rapidly and resulted in IMC spalling away from interface as indicated in Figure 2-5(c). According to SEM images, it is obviously that the growth rate at EP-Ni is much slower than that at EL-Ni. It is supposed that one of the reasons between the differences may result from how dense the structure is. The detail would be discussed later in this paper.

(ii) SnPb Solder Samples

Electroplated Ni was found to possess a lower reaction rate with the SnPb solder. Figure 2-6(a) shows the cross-sectional BEI SEM image for the as-fabricated sample. Even though the interface of the EP-Ni and solder on the chip side experienced about one-minute longer than the EL-Ni(P)/solder interface on the substrate side, the Ni_3Sn_4 IMC thickness at the EP-Ni/solder was thinner. It was $0.90\ \mu\text{m}$ at the EP-Ni/solder interface, whereas it was $1.20\ \mu\text{m}$ at the EL-Ni/solder interface. For the IMC morphology, it is rougher at the EP-Ni/solder interface as shown in the Figures 2-6(b) and 2-6(c). The reason for causing this difference is not clear at this moment. As the reflow time increased, the IMC thickness increased. Figures 2-7(a) to 2-7(d) display the SEM images at the EP-Ni side for the SnPb joints reflowed at 210°C for 5 min, 10 min, 1 hr and 9 hrs, respectively. The IMC thickness increased to 0.93, 0.93, 1.80 and $2.86\ \mu\text{m}$ for the four conditions, respectively. These results indicate that the reaction rate is very low between EP-Ni and the eutectic SnPb solder. On the other hand, the interfacial structure at the EL-Ni end were shown in Figures 2-8(a) to 2-8(d) for the above four reflowing conditions. The IMC thickness increased to 1.32, 1.39, 3.27 and $4.38\ \mu\text{m}$ for the sample reflowed for 5 min, 10 min, 1 hr and 9 hrs, respectively. Again, the IMC thickness was thinner on the EP-Ni side for all the four conditions.

2.3.2 NiSnP Phase and Kirkendall Void Formation

(i) SnAg Solder Samples

For more detailed analysis of the solder/UBM interface reaction, EDX and EPMA were used to identify phases at the interface as well. A representative EPMA image, Figure 2-9(a), shows the interface between SnAg solder and EL-Ni UBM layer at 250°C for 5 min. It reveals a composition that containing Sn, Ni and P exist between the Ni_3Sn_4 and Ni_3P . From the EPMA image, this thinner but clearly visible grey layer exists between the bright Ni_3Sn_4 and the dark Ni_3P layer. EPMA quantitatively analysis showed that the Sn concentration varies inside the NiSnP region with location close to Ni_3Sn_4 side containing larger amount of Sn and vice versa. This thin layer can't be identified the stoichiometry of the elements and either the formation mechanism so far. This unique NiSnP layer existed only in EL-Ni UBM system.

From the SEM images, Kirkendall voids, Figure 2-9(b), can be observed inside the Ni_3P layer in every sample we prepared. Even for SnAg reacted at 230°C for 5 min, the voids inside the columnar-type crystallized Ni_3P can be observed between Ni_3Sn_4 and EL-Ni UBM. These Kirkendall voids have been reported in previous literatures [17,29,30]. Similar situation occurred in our study as well. Based on the unbalanced atomic fluxes, Ni_3P layer formed easily as the Ni atom dissolved into the molten solder and became IMC. Therefore Kirkendall voids and micro-cracks can be obtained inside Ni_3P layer.

Furthermore, we found that the amount of voids increased with longer reflow time and higher temperature, and these voids would be more easily to be observed and their size would also be different. Whereas, there is no such void found at the EP-Ni interface, and the interface remained the same regardless the reflow temperature and durations, except that the IMC grew thicker. The IMC layer on EP-Ni interface did not spall into solder as the increasing reflow time. On the contrary, even a residual

Ni(P) layer, contacted with Cu under layer, was found in EL-Ni system; some Ni₃Sn₄ IMC was spalling into inside solder. He et al. reported that the stress, which generated during the formation of IMC through the liquid-solid reaction, would cause the IMC spalling from the Ni(P) UBM [21]. As the IMC layers became thicker, the compressive stress tends to squeeze out the IMC thus caused the spallation.

Formation of Kirkendall voids in the solder/UBM reaction has been reported by other researches [7,17,31]. The presence of voids was reported to be either in the Ni₃Sn₄ phase [17,31] or in the Ni₃P layer [11]. With the different locations of voids, one may conclude different formation mechanisms. Our observation shows that voids located at the between the Ni₃Sn₄/Ni₃P interface and in the Ni₃P layer. Therefore it was concluded that the presence of Ni₃P layer between the IMC and the UBM is an essential condition for void formation [32]. Due to the reaction at the liquid state, Sn reacted with Ni severely thus induced the depletion of Ni from the Ni-P layer. Therefore the crystallization of the P-enriched portion of the alloy was turn to be Ni₃P. And once the crystallized Ni₃P is formed, it would in opposition to increase the Ni depletion from the EL-Ni layer. Figure 2-9(a) clearly revealed that Ni₃P layer can be seen in SnAg solder system with Ni-P UBM. Consider of the EL-Ni layer, we cannot observe void formation inside this layer since it is an amorphous layer and it was difficult for vacancy to diffuse in. Indeed, the Sn would diffuse through IMC [31], but the Sn flux can be ignored, compared with the out-diffused Ni flux. With an unbalanced element diffusion flux, it leaded to the voids generated inside the Ni₃P layer.

On the contrary, the absence of voids at the interface of the EP-Ni UBM system can be realized because the EP-Ni is much denser that the reaction of Sn-rich solder is not quite easier for element to diffuse through it. Our experiments obtain a comparable result as the previous reference published by M. He et al. [18] whose

research showed void free interfaces of the sputtered pure Ni UBM system because of its dense structure.

(ii) SnPb Solder Samples

A NiSnP layer was detected between the Ni₃Sn₄ IMC and the Ni₃P layer, as shown in Figure 2-10(a). Voids were frequently observed in the Ni₃P layer, as indicated by the arrows in Figure 2-10(b). These Kirkendall voids have been reported in previous literatures [18,22,3]. Furthermore, we found that the amount of voids increased with an increase in reflow time and temperature. Whereas, there is no void found at the Ni₃Sn₄/EP-Ni interface, and the interface remained almost the same regardless the reflow temperature and times, except that the IMC grew thicker. The IMC layer in EP-Ni side did not spall into solder for all the reflow conditions. On the contrary, even there was still remaining Ni(P) layer, some Ni₃Sn₄ IMCs were observed inside solder. He et al. reported that the stress, which generated during the formation of IMC through the liquid-solid reaction, caused the IMC spalling from the Ni(P) UBM [22].

2.3.3 Intermetallics Growth Kinetics

(i) SnAg Solder Samples

It is known that the growth kinetics of the continuous IMC layer (Ni₃Sn₄) can be expressed with an empirical power law describing the average IMC thickness (h) as a function of time (t) and temperature (T):

$$h(t, T) = h_0 + k_h \exp\left(-\frac{Q_h}{RT}\right) t^{1/n} \quad (2-1)$$

where h_0 is the initial intermetallic thickness, k_h and n are constants, Q_h is the apparent activation energy for the thickening process, R is the universal gas constant.

According to equation (2-1), plot Ni₃Sn₄ thickness against the nature log of reflow

time for both EP-Ni and EL-Ni layer, the fitting of the experimental data, shown in Figure 2-11(a), yielded n values of 4.5 and 3.12 for EP-Ni and EL-Ni UBMs respectively. This result is comparable with the n values of 4.55 and 4.69 that reported by Ghosh for Ni_3Sn_4 scallops formed in SnAg/Ni samples at 230-290°C up to 5 min [22]. Furthermore, took nature log of diffusivity and plotted versus with $1/T$, where T is temperature, IMC formation activation energy for both EP-Ni and EL-Ni can be obtained. The activation energies are 25 kJ/mol of IMC formation at the EP-Ni layer, and are 38 kJ/mol at EL-Ni layer respectively, as shown in Figure 2-11(b). These values are quite different compared with the activation energies of 13-17 kJ/mol resulted from Ni diffused in liquid Sn reported by the previous research [35]. The possible reason for this phenomenon would be explained later.

During soldering process, it involves several interface stages, for instance, phase nucleation, atomic transfer across the interface, creation or annihilation of point defects, and dissolution into the molten solder. Therefore, the kinetic parameters evaluated from experimental data may have combined information. The thickening process of Ni_3Sn_4 in Figure 3-5 for both EP-Ni and EL-Ni systems, demonstrates a different behavior from diffusion-controlled growth, which predicts $t^{1/2}$ growth kinetics [22,29,30] and from a scallop coarsening by a ripening process refers to $t^{1/3}$ [34]. These results obtained from our experiment are comparable to the results reported by Ghosh [22]. According to Ghosh, the thickening kinetics of Ni_3Sn_4 scallop is related to the radial growth kinetics, and the grain boundary diffusion is essential in the thickening kinetics, since Ni_3Sn_4 scallops are individual grains.

Kang and Ramachandran [35] reported the interfacial reaction kinetics between pure liquid Sn and bulk Ni. Three kinetic regions for IMC growth could be found, where Ni_3Sn_4 was the dominant phase, in the temperature range of 300–513 °C: initial with $n=1.85$, intermediate with $n=8.33$, and final with $n=1.59$. Kang, Rai, and

Purushothaman [36] reported the interfacial reaction between electroplated Ni,Cu and various solders without kinetic parameters. Gur and Bamberger [37] reported that both thickening and grain growth kinetics of Ni₃Sn₄ follow parabolic law in Ni/Sn diffusion couples in the temperature range from 235 to 600 °C. Considering of the $t^{1/3}$ growth kinetics, Kim and Tu [34] proposed a model which assumes that the scalloped grains coarsening is caused by a ripening process in which the driving force is the Gibbs–Thomson effect. On the other hand, a model based on grain boundary diffusion controlling mass transport also predicts the $t^{1/3}$ behavior [38]. Recently, Ghosh reported n values for Sn-3.5Ag, Sn-Bi and Sn-38Pb reacted with Ni in different temperature ranges. The n values are 4.55 at 230°C and 4.69 at 260°C for SnAg solders. Li *et. al* also reported the interfacial reactions of Ni and Ni(P) with liquid Sn-Bi solders [25]. The n value is greater than three for the thickening kinetics of Ni₃Sn₄ scallop formed in both systems. As reflected by the predicted n values here, the bulk diffusion controlled process occurred in these interfaces might only have minor effect on the thickening process and grain boundary diffusion may be the dominant effect. In order to investigate the radial growth to get further understanding regarding the thickening mechanism, samples were polished crosscut and observed IMC layer from top view on EP-Ni.

Indeed larger n value predicts a slower reaction rate. According to our observation, the IMC shape at the EP-Ni side is comparable before and after the reflow process. However, the IMC at the EL-Ni side showed different morphologies with different process conditions. The IMC at EL-Ni side grew bigger and became layer type after more than 5 minutes reflow while the IMC at the chip side still maintained like column and faceted type and remained thin. To figure out the mechanism and the difference, the IMC height changing without enlarging the grain size suggested that the growth of IMC at the EP-Ni side is only one dimension. The

IMC layer top view images after reflow 5 and 10 mins, Figure 2-12(a) and 2-12(b) show that the size of IMC remained the same; however, the height measured from cross-sectional images kept the same value. Based on our suggestion, the supply of Ni atoms came from the liquid channel between the IMC at the beginning; once the channel became IMC as well, the Ni must diffuse through IMC to react with Sn atoms. Therefore the diffusion paths became longer and the reaction time would be increase. Moreover, it is supposed that once the Ni atom dissolved into molten solder, it will have tendency to diffuse to the top and react in order to maintain the facet shape. As the extended of the reflow time the IMC grew higher and thus diffusion path for Ni became longer. By these two reasons, we therefore got the larger n value, which predicted slower reaction rate by the increase of reaction time. Yet why it was easier to react at the top of IMC/molten-solder interface is still open to question. However it is suggested that free energy might be the main dominant factor.

Ghosh [26] first utilized the radial size distribution (RSD) as a function of the reaction time to analyze the radial growth kinetics of the Ni_3Sn_4 and further understanding can be obtained. According to their results, grain boundary diffusion and radial growth played an important role in thickening process of Ni_3Sn_4 formation. Compare with our results, we got the similar results as well. In short, the grain boundary diffusion combined with radial growth process could have large effect on the n value and resulted in slow reaction rate at EP-Ni interface.

The activation energy could be calculated by the empirical law in Eq. (2-1). The activation energies are 25 kJ/mol for EP-Ni interface, and 38 KJ/mol for EL-Ni interface, respectively for the first 5 minutes. Compared with the 13 to 17 kJ/mol activation energies of the reaction between liquid Sn and bulk Ni [35], the activation energy of EL-Ni has a lager value. However, Gur and Bamberger also reported that the activation energy for the diffusion of Ni in liquid Sn is 27.6 ± 1.7 kJ/mol in the

temperature range of 235 to 600°C [37]. From our observation, the activation energy of the eutectic SnAg in Ni system is higher than that for the pure Sn in Ni.

In fact, the prefactor could have a great effect on estimating the IMC growth activation energy. The larger activation energy we got so far doesn't represent high-speed reaction rate; however, it simply indicated that the formation of IMC at the EL-Ni side was much sensitive to the temperature difference compared with that at EP-Ni side. In other words, the thickness of IMC at EL-Ni side is more sensitive with the increase in temperature. Since the paths for IMC formation at EL-Ni layer side was mainly counted on the crystalline Ni₃P grain boundaries and the number of Kirkendall voids which both would increase with the increase of the reflow temperature. As the temperature increased, the IMC grew thicker and thus we obtained higher activation energy.

The activation energies we had so far are quite different from others since it is a direct comparison between EP-Ni and EL-Ni UBM in the liquid-solid reaction with solders at the same time, which represents real scale flip chip solder as well. This provides us a starting-point to distinguish their reaction rate and activation energy. Besides, there are quite few researches focus on metallurgical reaction in flip chip scale thus we can provide quite useful information for packaging technology. From the results, we can conclude that EP-Ni has much slower reaction rate with solders than EL-Ni and resulted in higher bonding strength here.

(ii) SnPb Solder Smamples

The average IMC thicknesses are listed in Table 2-2 for all the reflowing conditions. The fittings of the experimental data are shown in Figure 2-13(a), which yields an n value of 4.07 and 3.66 for EP-Ni and EL-Ni system, respectively. The values appear slightly bigger than that of 3.14 reported by Ghosh [22] for Ni₃Sn₄

scallops formed in Sn-38Pb/Ni samples at 200-250°C for 5 min. The measured n value is greater than 3.0 for the thickening kinetics of Ni₃Sn₄ IMCs formed in both systems. The thickening process of Ni₃Sn₄ for both EP-Ni and EL-Ni systems in this study differs from diffusion-controlled growth, which predicts $t^{1/2}$ growth kinetics [22,29,30], and from scallop coarsening by a ripening process with thickness proportional to $t^{1/3}$ [38]. According to Ghosh, the thickening kinetics of Ni₃Sn₄ scallops is related to the radial growth kinetics, and grain boundary diffusion may play an important role in the thickening kinetics. Thus, the kinetics in this study may be governed by grain boundary diffusion.

To calculate the activation energy for the Ni₃Sn₄ IMC formation on EP-Ni and EL-Ni(P) UBMs, the Arrhenius plot is shown in Figure 2-13(b) using the thickness data at 1 hr of reflow time. The activation energy for EP-Ni UBM is measured to be 51 kJ/mol, whereas it is 48 kJ/mol for EL-Ni UBM. Compared with the results for the eutectic SnPb solder on Ni foil reported by Kim et al. [9], as shown in Figure 2-13(c), the activation energy they obtained ranges from 47 to 32 kJ/mol using the data for 5 and 10 min of reflow time. The values we obtained are slightly higher. In addition, these values are much higher than those reported by Kang and Ramachandran for Ni reacting with liquid Sn at 300-520°C [2]. The values they obtained lie between 13 and 17 KJ/mol. In addition, Gur and Bamberger also reported that activation energy for diffusion of Ni in liquid Sn is 27.6 ± 1.7 kJ/mol in the temperature range 235-600°C [37]. Thus the activation for the eutectic SnPb on Ni is much higher than that for the pure Sn on Ni.

The above results indicate that the reaction between EL-Ni and SnPb solder has a small activation energy but a higher reaction rate when compared with the EP-Ni. The faster reaction rate for EL-Ni may be attributed to the following reasons: once the

Ni₃P layer forms, Ni atoms could diffuse through Kirkendall voids that exist inside Ni₃P layer. As the reflow time increases, the IMC grew thicker, and then the IMC growth should be via other paths. It is known that for the Ni₃Sn₄ growth, Sn atoms are found to be the dominant diffusion species [32,33]. Therefore, the thickening process could switch to be controlled by Sn atoms diffused through the Ni₃Sn₄ layer to react with Ni atoms. In addition, the voids in the Ni₃P layer provide abundant vacancy source, which is shown in Figure 2-10(b), causing the faster diffusion rate of Sn atoms through the Ni₃Sn₄ layer. Thus, the growth rate of Ni₃Sn₄ in EL-Ni UBM was faster.

2.3.4 Ni consumption rate

In order to determine the different consumption rate of EP-Ni and EL-Ni, we assume that the total loss of Ni was equal to the summation of Ni in Ni₃Sn₄ and in the liquid solder. From the mass balance of Ni, the consumed thickness of Ni is:

$$\Delta h = \frac{1}{\rho_{Ni} A} \left(\frac{nV}{100} \rho_L + f_{Ni} \rho_C V_C \right) \quad (2-2)$$

Where A is the total interfacial area between solder and Ni, n is the wt% of Ni in liquid solder, V is the total volume of liquid solder, f_{Ni} is the weight fraction of Ni in the Ni₃Sn₄ compound, t_C is the thickness of Ni₃Sn₄, and ρ_{Ni} , ρ_L , and ρ_C are the density of Ni, liquid solder and Ni₃Sn₄ compound, respectively. After the saturation of Ni in the molten solder, the consumption rate of Ni depends on the change of volume of Ni₃Sn₄ compounds, and then the rate equation is given by:

$$\frac{dh}{dt} = f_{Ni} \frac{\rho_C}{\rho_{Ni}} \frac{dt_C}{dt} \quad (2-3)$$

Since the solubility of Ni in the eutectic SnPb solder between 200°C and 240 °C is very small, the value of n in Eq. (2-2) is very small. The consumption rates of Ni at 240°C are shown in Figure 3-14, which are 0.97×10^{-3} μm/s for EP-Ni and 1.48×10^{-3}

$\mu\text{m/s}$ for EL-Ni for 5 min of reflow time. In general, the EP-Ni has denser structure than the EL-Ni, which may be responsible for the slower Ni consumption rate for EP-Ni. Furthermore, compared with consumption rate reported by Kim *et. al.*, it is $0.38 \times 10^{-3} \mu\text{m/s}$ at 240°C within 10 min for SnPb solder reacting with Ni foil [9]. The consumption rate for the bulk Ni is also shown in the figure. The lower consumption rate for the Ni foil may be attributed to its dense structure. Thus EP-Ni and EL-Ni have higher reaction rates than the Ni foil with molten SnPb solder.

To investigate whether the EL-Ni on the substrate has effect on the formation of Ni_3Sn_4 IMC on the chip end, the metallurgical reaction in bump-die samples which is only with EP-Ni UBM was also studied. Table 3-3 shows the IMC thickness and the consumed EP-Ni thickness. The consumed EP-Ni thickness after reflow at 210°C is $0.30 \mu\text{m}$, $0.37 \mu\text{m}$, $0.73 \mu\text{m}$ and $1.02 \mu\text{m}$ for 5 min, 10 mins, 1 hr and 9 hrs, respectively, and the corresponding SEM images are shown in Figure 2-15. The rate of consumption of EP-Ni in bumped-die samples at 210°C is $1.0 \times 10^{-3} \mu\text{m/s}$ for 5 min of reflow time. Compared with flip-chip samples, the EP-Ni consumption rates for bumped-die samples are very close to those of flip-chip samples. These results imply that the EL-Ni on the substrate end has little effect on the IMC formation on the chip end, which may be attributed very small Ni solubility in the eutectic SnPb solder. Therefore, the measured Ni consumption rate for flip-chip samples is quite close to that of bumped-die samples.

2.4 Summary

Using flip-chip scale samples, the liquid-state reaction between the SnAg and SnPb solder with EP-Ni as well as EL-Ni has been studied at various reflowing conditions. By fabricating the EP-Ni on the chip side and the EL-Ni on the substrate side, direct comparison on the growth of Ni_3Sn_4 can be made. The IMC growth rate

on the EP-Ni was much slower for all the reflowing conditions compared with EL-Ni UBM. For SnAg system, the temporal law with time exponent, n , where n is greater than three was obtained for the thickening kinetics of Ni_3Sn_4 scallops formed in both EP-Ni and EL-Ni systems. This can be attributed to that the thickening process was mainly affected by grain boundary diffusion and the radial growth reported before. In SnPb system, the consumption rate has been measured to be $0.97 \times 10^{-3} \mu\text{m/s}$ and $1.48 \times 10^{-3} \mu\text{m/s}$ for EP-Ni and EL-Ni, respectively. The activation energy has been determined to be 51 kJ/mol and 48 kJ/mol for the EP-Ni and EL-Ni within 10 min of reflowing time, respectively.

During the reaction, porous Ni_3P layer, along with micro-cracks formed between the IMC and the EL-Ni layer are observed in SnAg and SnPb systems. This porous layer may provide abundant vacancies for the Ni atoms to diffuse through the IMC layer, thus its IMC growth rate was faster on the EL-Ni UBM. There also existed one distinctive layer, NiSnP between the Ni_3Sn_4 and the Ni_3P layer in the Ni-P UBM side and the exact crystal structure of the ternary NiSnP is yet to be clearly identified till now. The activation energy for Ni_3Sn_4 growth in liquid state reaction in SnAg system is found to be 25 kJ/mol at the EP-Ni UBM and is 38 kJ/mol at the EL-Ni UBM. The larger activation energy for EL-Ni UBM predicted that the IMC growth here changes seriously with temperature difference. The mechanism that affects the difference in the activation energy with EP-Ni and the EL-Ni needs to be studied in the future. On the other hand, the larger time exponent at the EP-Ni side here, the n value, predicted a slower reaction rate as the increase in processing duration. In our study, EL-Ni does not provide a longer life time than EP-Ni reacted with molten SnAg solder, and EP-Ni can serve as a good adhesion layer in contact with molten solder.

2.5 References

1. R.R. Tummala, E.J. Rymaszewski, and A.G. Klopfenstein: *Microelectronics Packaging Handbook*, 2nd ed. (Chapman & Hall, 1997) Part 2, Ch 8.
2. S. K. Kang and V. Ramachandran, *Scripta Mat.* **14**, 421 (1980).
3. M. O. Alam, Y. C. Chan and K. C. Hung, *J. Electron. Mater.* **31**, 1117 (2002).
4. K.H. Prakash and T. Sritharan, *J. Electron. Mater.* **32**, 939 (2003).
5. K. N. Tu and K. Zeng, *Mater. Sci. and Eng. R* **34**, 1 (2001).
6. H. K. Kim, K. N. Tu and P. A. Totta, *Appl. Phys. Lett.* **68**, 2204 (1996).
7. K. Zeng and K. N. Tu, *Mater. Sci. Eng. R* **38**, 55 (2002).
8. R.J.K. Wassink, *Soldering in Electronics*. Electrochemical Publications, *IOM* (1984).
9. P. G. Kim, J. W. Jang, T. Y. Lee and K. N. Tu, *J. Appl. Phys.* **86**, 6746 (1999) .
10. K. L. Lin and Y. C. Liu, *IEEE Trans. Adv. Pack.* **22**(4), 568 (1999).
11. Z. Mei and R. H. Dauskardt, Reliability of electroless processed thin layered solder Joints. in 1999 MRS Spring Meeting Symposium M; Materials Reliability in Microelectronics IX; pp. 1.
12. C. Y. Lee and K. L. Lin, *Thin solid films* **249**(2), 201 (1994).
13. J. W. Jang, P. G. Kim and K. N. Tu, *J. Appl. Phys.* **85**(12), 8456 (1999).
14. K. C. Hung, Y. C. Chen, C. W. Tang and H. C. Ong, *J. Mater. Res.* **15**(11), 2534 (2000).
15. K. C. Hung and Y. C. Chen, *J. Mater. Sci. Lett.* **19**,1755 (2000).
16. J. W. Jang, D. R. Peter, T. Y. Lee and K. N. Tu, *J. Appl. Phys.* **88**, 6359 (2000).
17. Y. D. Jeon, K. W. Paik, K. S. Bok, W. S. Choi and C. L. Cho, *J. Mater. Res.* **31**, 520 (2002).
18. M. He, A. Kumar, P. T. Yeo, G. J. Qi and Z. Chen, *Thin Solid Films* **462-463**, 387 (2004).
19. S. J. Wang, H. J. Kao and C. Y. Liu, *J. Electron. Mater.* **30**(2), 130 (2004).

20. S. J. Wang and C. Y. Liu, Scripta Mat **49**, 813 (2003).
21. M. He, W. H. Lau, G. Qi and Z. Chen, Thin Solid Films **462-463**, 376 (2004).
22. G. Ghosh, J. Appl. Phys. **88**(11), 6887 (2000).
23. P.L. Tu, Y.C. Chan, K.C. Hung and J.K.L. Lai, Scripta Mat **44**, 317 (2001).
24. G. Ghosh, Acta Mater **49**, 2609 (2001)
25. J.F. Li, S.H. Mannan, M.P. Clode, K. Chen, D.C. Whalley, C. Liu and D.A. Hutt, Acta Mater **55**, 737 (2007)
26. G. Ghosh, Acta Mater. **48**, 3719 (2000).
27. C. P. Huang and C. Chen, J. Mater. Res. **20**(10), 2772 (2005).
28. C. S. Huang, J. G. Duh and Y. M. Chen, J. Electron. Mater. **32**(12), 1509 (2003).
29. Y. Takaku, X. J. Liu, I. Ohnuma, R. Kainuma, K. Ishida, Mater Trans. **45**, 646 (2004).
30. R. H. Dauskardt, F. Haubensak and R. O. Ritchie, Acta Metall Mater. **38**(2), 143 (1990).
31. C. M. Chen and S. W. Chen, J. Appl. Phys. **90**(3), 1208 (2001).
32. C. E. Ho, S. E. Yang and C. R. Kao, J Mater Sci : Mater Electron **18**, 155 (2007).
33. A. A. Liu, K. N. Kim and P. A. Totta, J. Appl. Phys. **80**, 2774 (1996)
34. H. K. Kim and K. N. Tu, Phys Rev B **53**, 16027 (1996).
35. S. S. Kang and V. Ramachandran, Scr Metall **14**, 421 (1980).
36. S. K. Kang, R. S. Rai and S. Purushothaman, J. Electron. Mater. **25**, 1113 (1996).
37. D. Gur and M. Bamberger, Acta Mater **46**, 4917 (1998).
38. M. Schaefer, R. A. Fournelle and J. Liang, J. Electron. Mater. **27**, 1167 (1998).

Table 2-1 Average thickness of Ni₃Sn₄ for various reflow conditions in this study
(SnAg system).

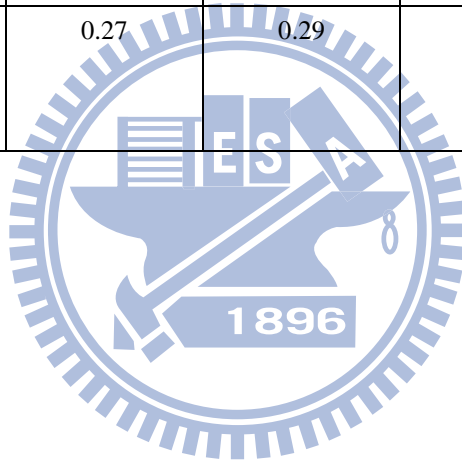
	5 min	10 min	15 min	20 min
230°C EP-Ni	1.62			
230°C EL-Ni	2.96			
240°C EP-Ni	1.7	2.18	2.42	2.56
240°C EL-Ni	3.33	4.63	5.97	6.74
250°C EP-Ni	1.83			
250°C EL-Ni	3.56			
260°C EP-Ni	1.9			
260°C EL-Ni	3.84			

Table 2-2 Average thickness of Ni₃Sn₄ for various reflow conditions in this study
(SnPb system).

	5 min	10 min	1 hr	4 hrs	6.25 hrs	9 hrs
200°C EP-Ni	0.94	0.93	1.60			
200°C EL-Ni	1.26	1.3	2.80			
210°C EP-Ni	0.93	0.93	1.80	2.14	2.47	2.86
210°C EL-Ni	1.32	1.39	3.27	3.88	4.12	4.38
220°C EP-Ni	0.98	0.94	2.09			
220°C EL-Ni	1.39	1.43	3.56			
240°C EP-Ni	0.97	0.96	2.33			
240°C EL-Ni	1.48	1.54	3.87			

Table 2-3 Average thickness of Ni_3Sn_4 for various reflow times for bumped-die samples reflowed at 210°C .

	5 min	10 min	1 hr	9 hrs
IMC thickness on EP-Ni (μm)	0.88	1.02	2.27	3.01
Calculated EP-Ni consumed thickness	0.26	0.31	0.68	0.90
Direct measured EP-Ni consumed thickness	0.30	0.37	0.73	1.02
calculated EP-Ni consumed thickness for flip-chip samples	0.27	0.29	0.54	0.89



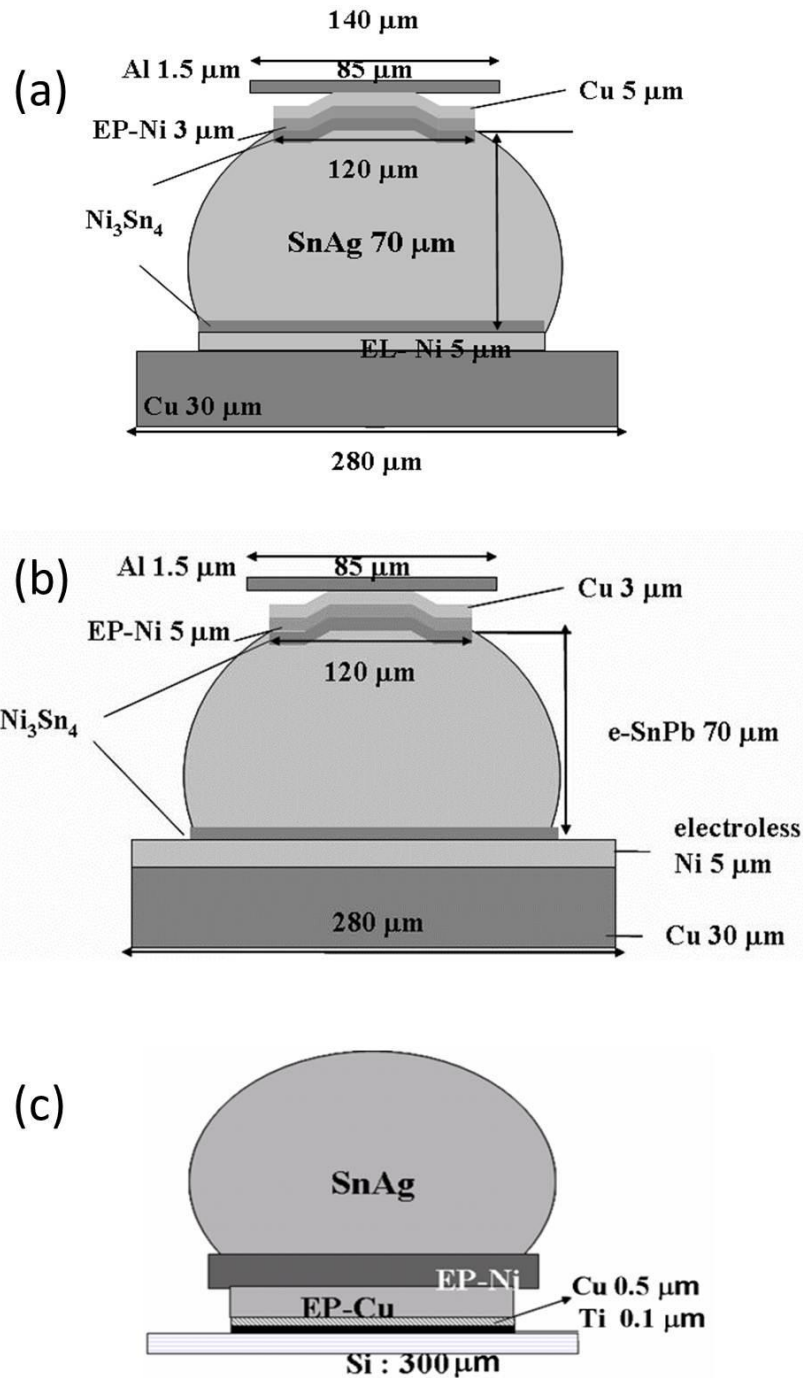


Figure 2-1 (a) Schematic structure for sample used in this study. EP-Ni was adopted on the chip side and EL-Ni was fabricated on the substrate side; (b) SnPb solder with EP-Ni on the chip side and EL-Ni on the substrate side. (c) Schematic illustrations for the three types of bump-die sample used in this study: 5 μm -Cu/3 μm -Ni.

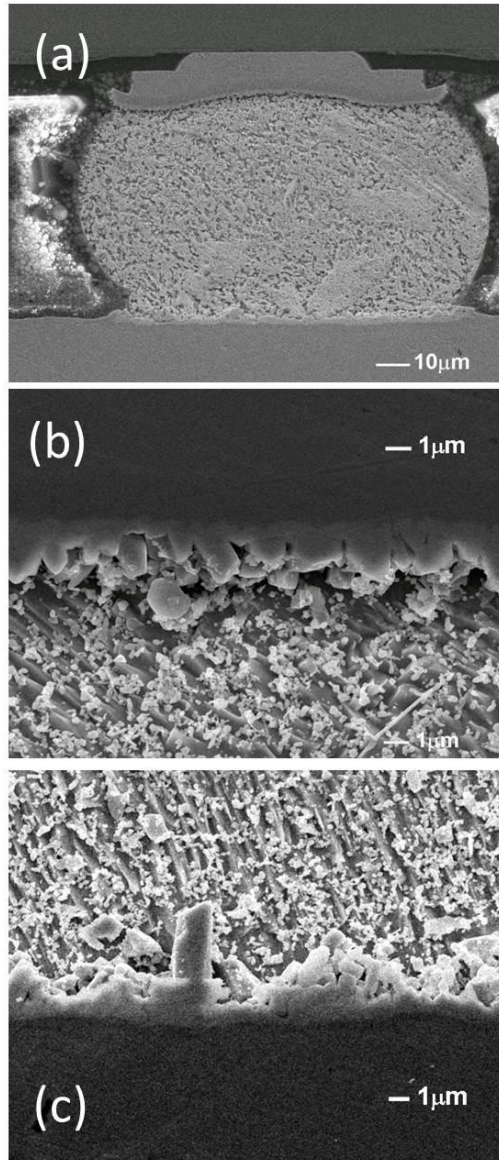


Figure 2-2 Morphology of Ni_3Sn_4 IMC in SnAg solder with plated Ni and the electroless Ni(P) UBM system. (a) Whole bump; (b) Cross-section view at the plated Ni interface (chip side); (c) Cross-section view at the electroless Ni(P) interface (board side).

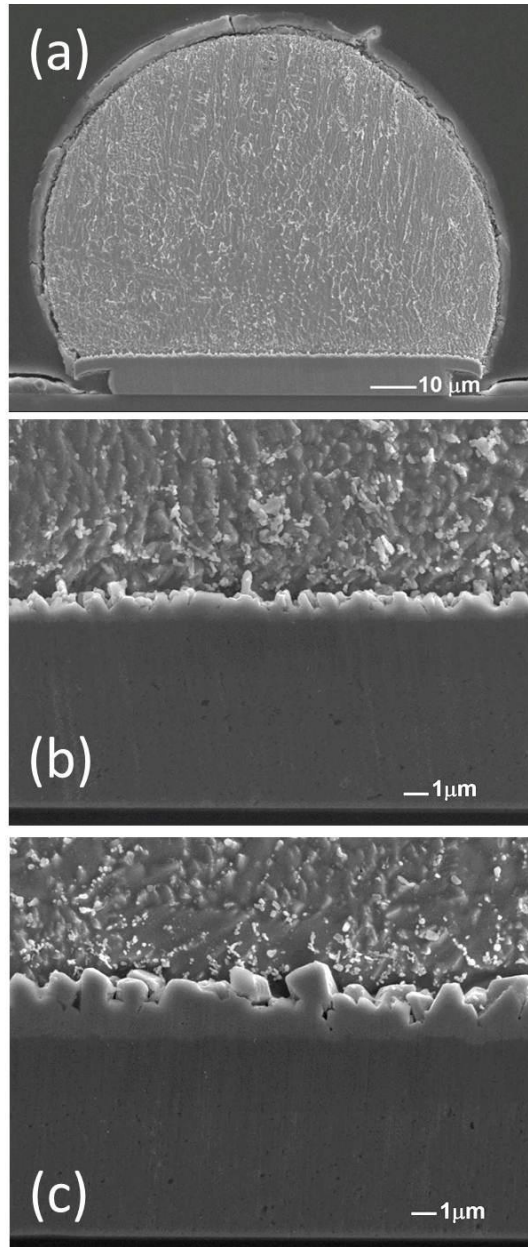


Figure 2-3 Cross-sectional SEM images for the SnAg solder bumps: (a) Whole bump; (b) magnified image for the interfacial structure in 5 μm-Cu/3 μm-Ni sample; (c) the interfacial microstructure after 10 times reflow process.

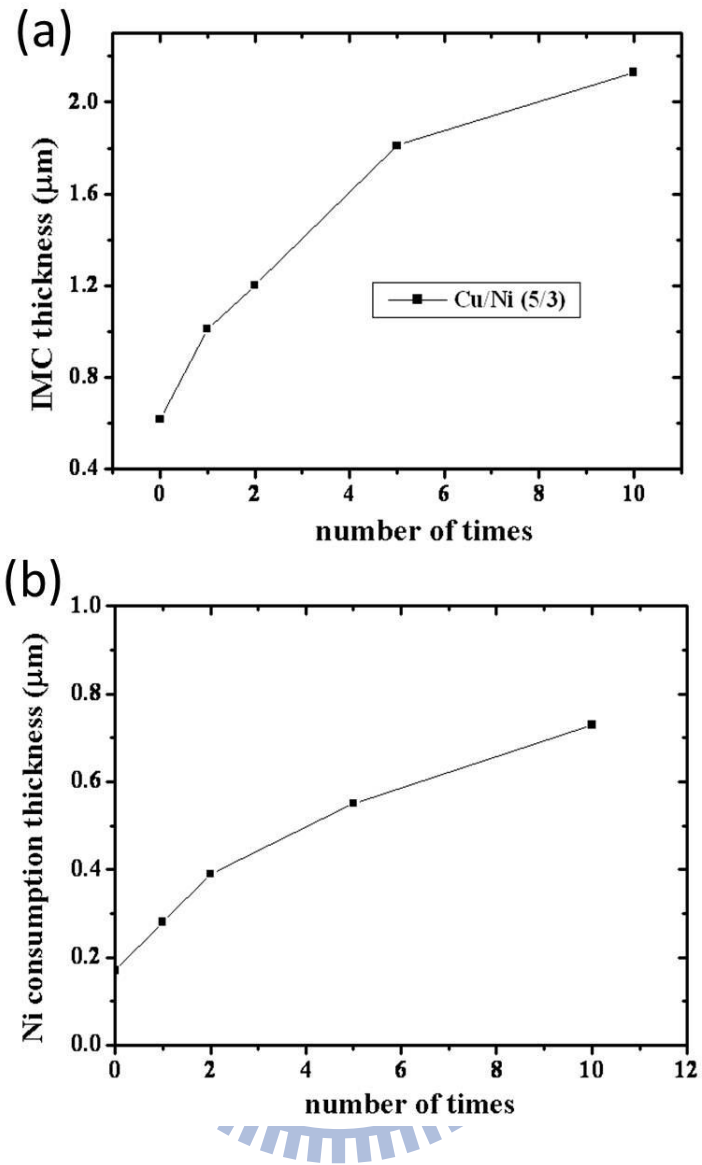


Figure 2-4 (a) IMC thickness versus with reflow times in 5 μm -Cu/3 μm -Ni sample;

(b) IMC consumption thickness versus with reflow times.

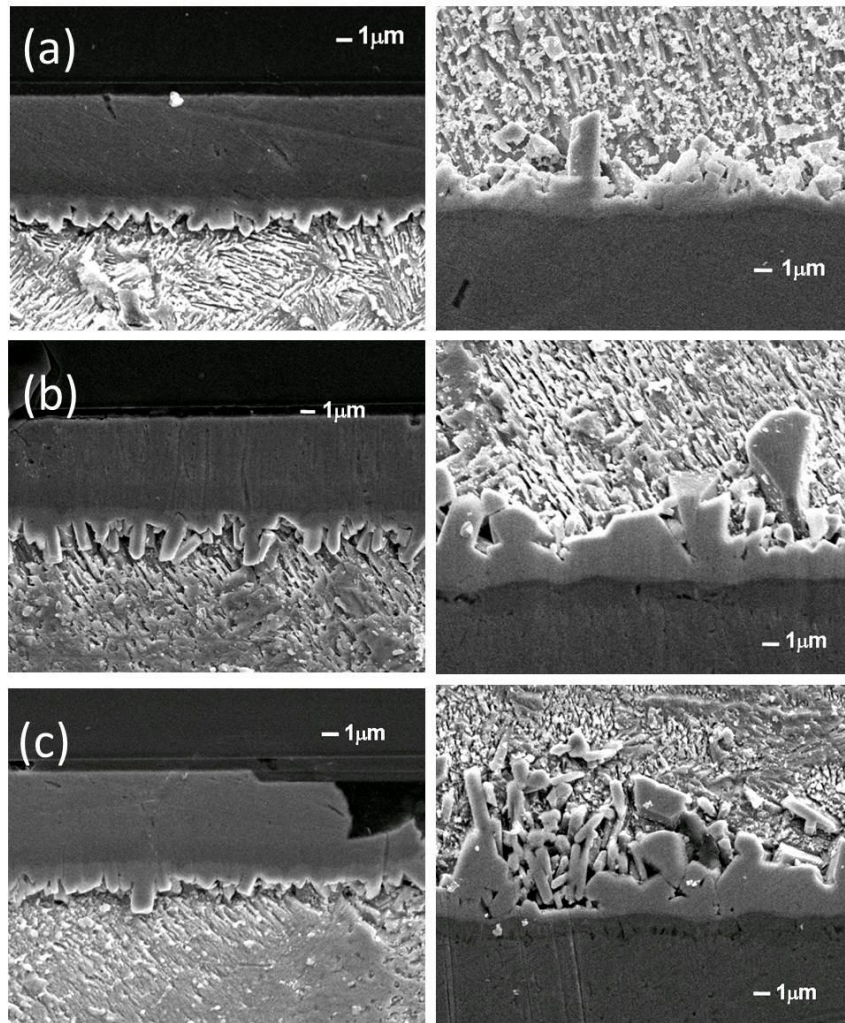


Figure 2-5 Cross-sectional SEM images showing morphology of Ni_3Sn_4 IMC at the interface of the SnAg solder with the EP-Ni and EL-Ni reflowed at 240°C . (a) for 5 min; (b) for 10 min; (c) for 20 min.

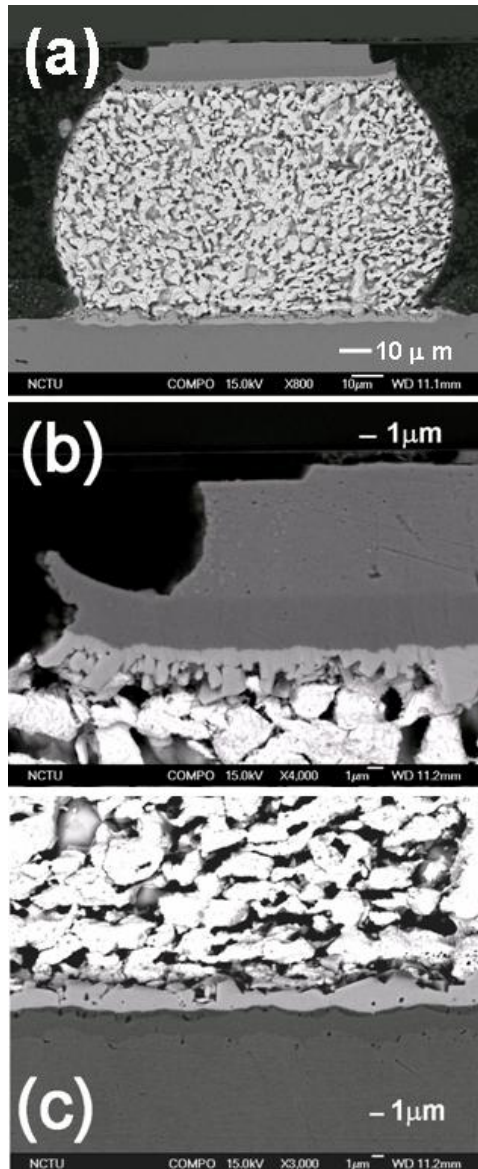


Figure 2-6 Cross-sectional SEM images showing morphology of Ni_3Sn_4 IMCs in SnPb solder with EP-Ni UBM and EL-Ni(P) metallization (a) for whole bump, (b) enlarged view of EP-Ni on the chip side, and (c) enlarged view of EL-Ni on the substrate side.

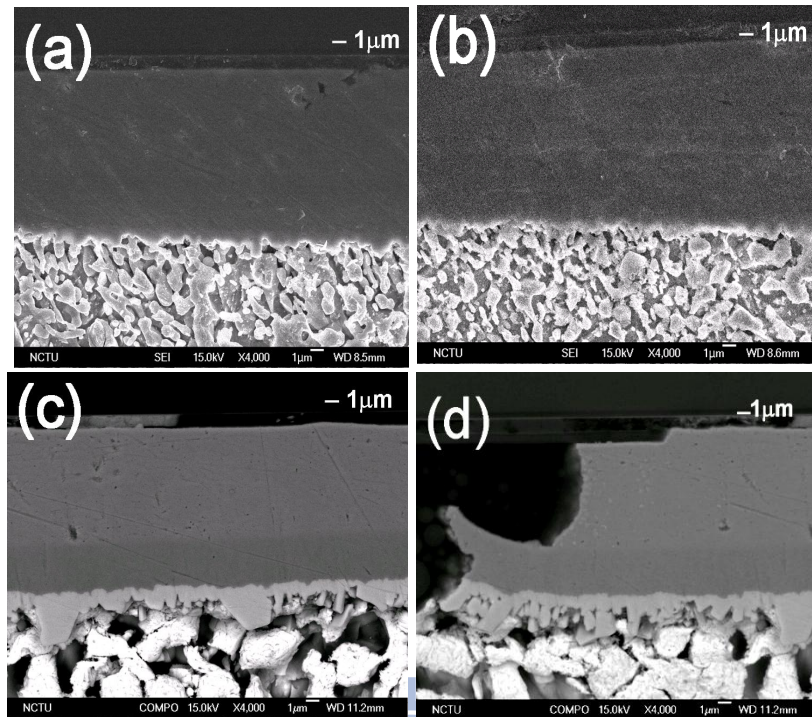


Figure 2-7 Cross-sectional SEM images showing morphology of Ni_3Sn_4 IMCs at interface of Sn-Pb solder and EP-Ni UBM reflowed at 210°C for (a) 5 min, (b) 10 min, (c) 1 hr, and (d) 9 hrs.

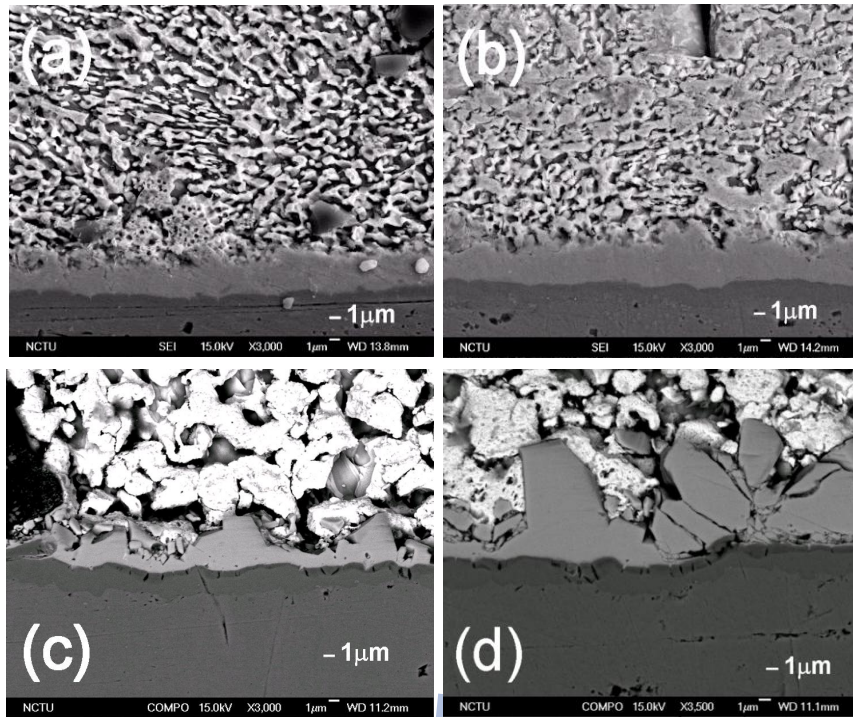


Figure 2-8 Cross-sectional SEM images showing morphology of Ni₃Sn₄ IMCs at the interface of Sn-Pb solder and EL-Ni UBM reflowed at 210°C for (a) 5 min, (b) 10 min, (c) 1 hrs, and (d) 9 hrs.

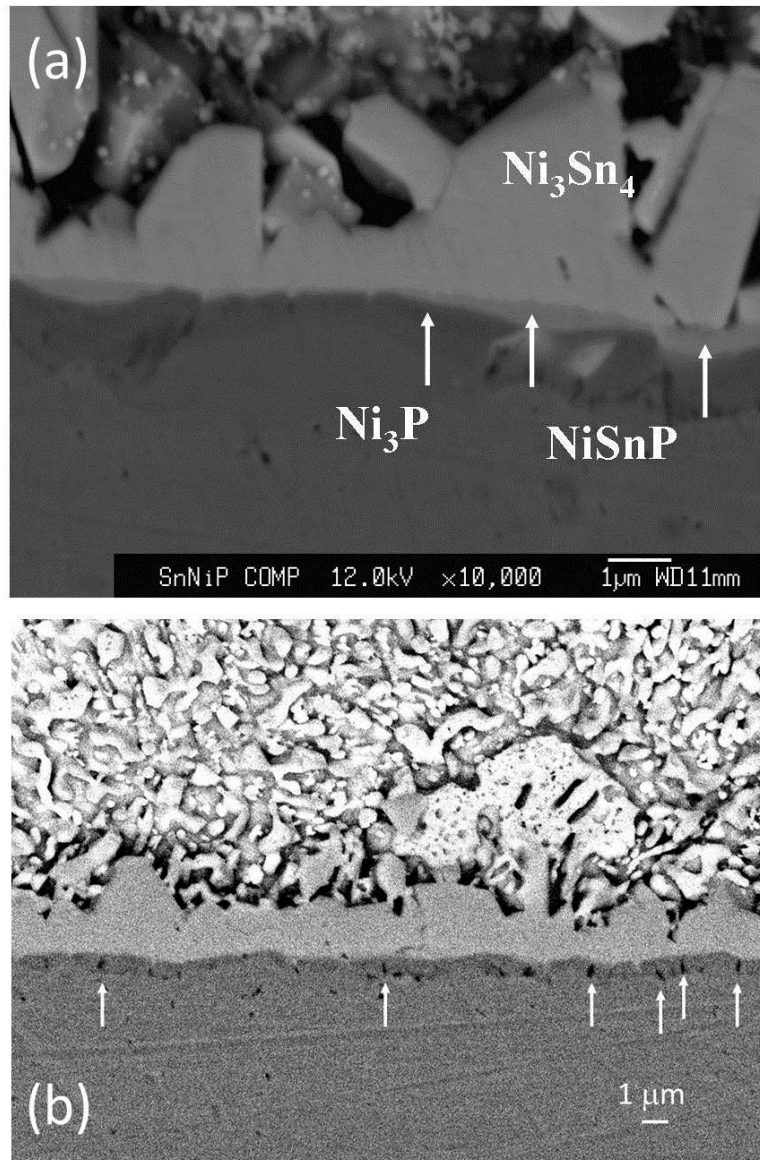


Figure 2-9 (a) EPMA analysis of NiSnP layer between Ni₃Sn₄ and Ni₃P layers in SnAg sample reflowed at 250°C for 5 min. (b) Kirkendall voids formed in samples of SnAg solder with Ni-P UBM reflow at 230°C for 5min.

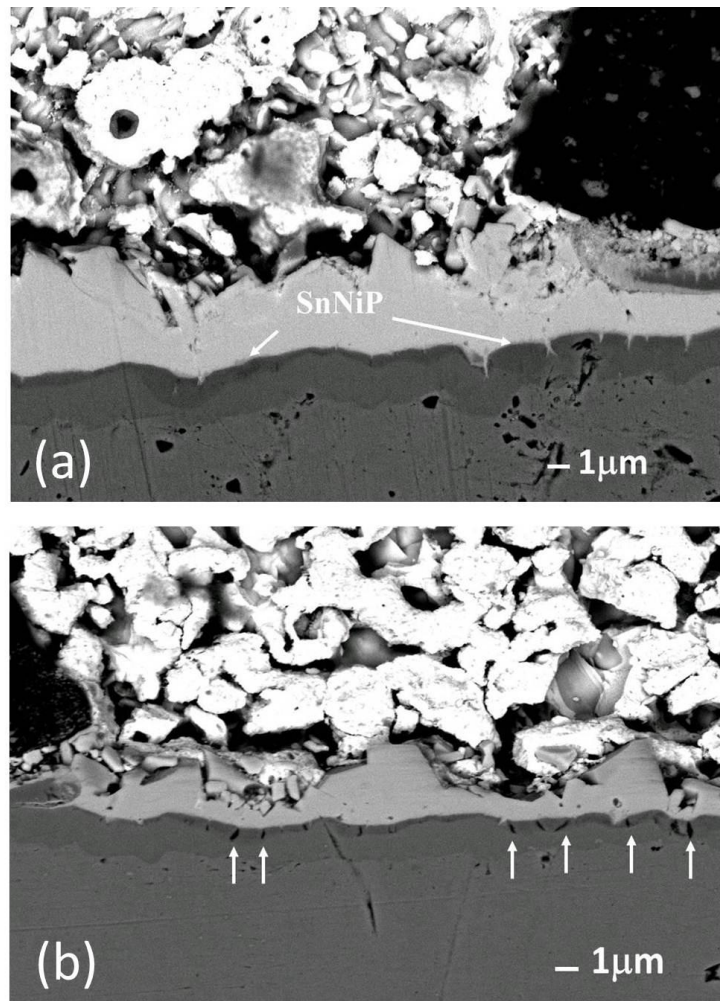


Figure 2-10 (a) Enlarged BEI SEM image on the substrate side showing the IMCs, NiSnP, Ni₃P, and the remaining Ni(P) layer after being reflowed at 210°C for 1 hr, and (b) numerous voids were observed in the Ni₃P layer, indicated by arrows.

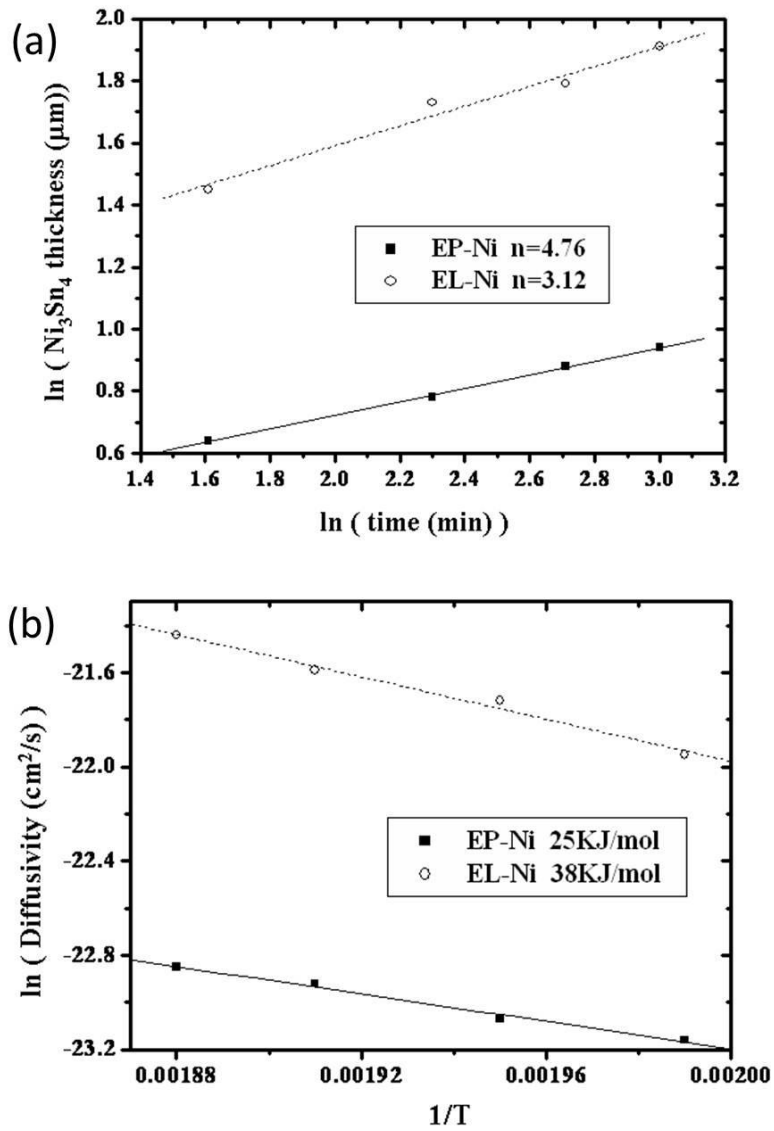


Figure 2-11 (a) Plot of the Ni_3Sn_4 thickness against the nature log of reflow time for both EP-Ni and EL-Ni metallizations; (b) Arrhenius plot for both EP-Ni and EL-Ni metallizations. The activation energies were determined to be 25 kJ/mol and 38 kJ/mol for the IMC growth on EP-Ni and EL-Ni, respectively.

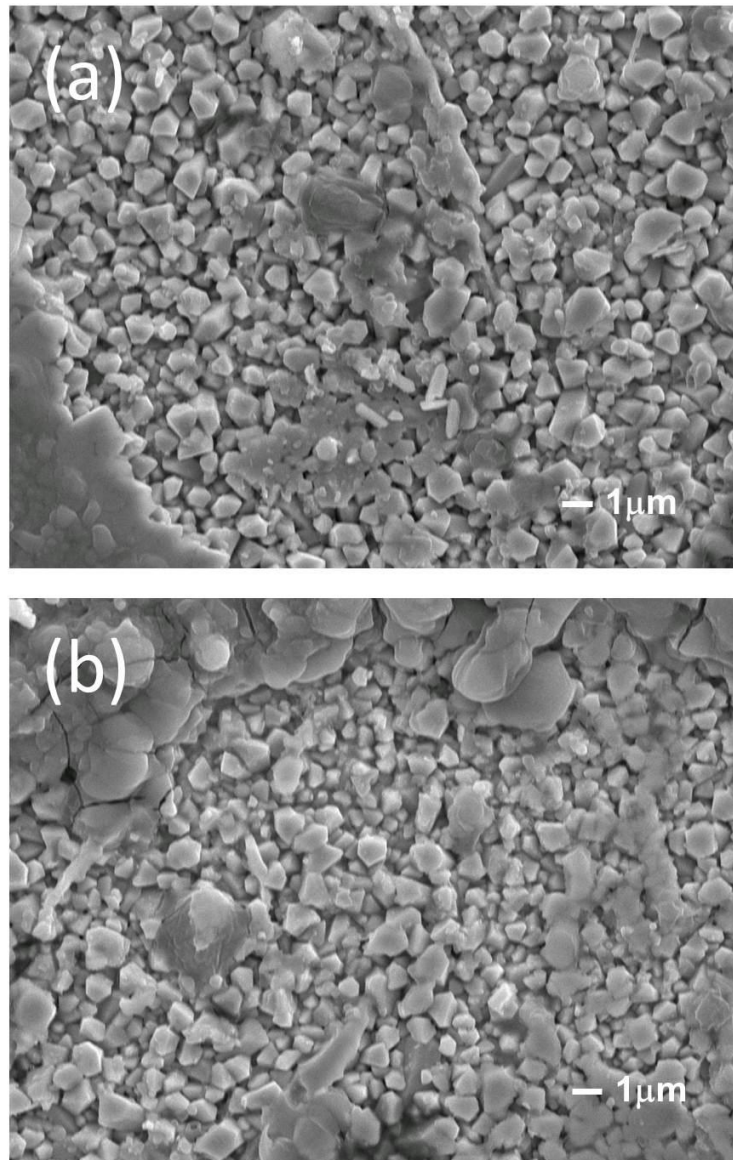


Figure 2-12 Top view SEM images of the interfacial microstructure of the SnAg solder at the EP-Ni side (a) after 5min reflow, (b) after 10 min reflow.

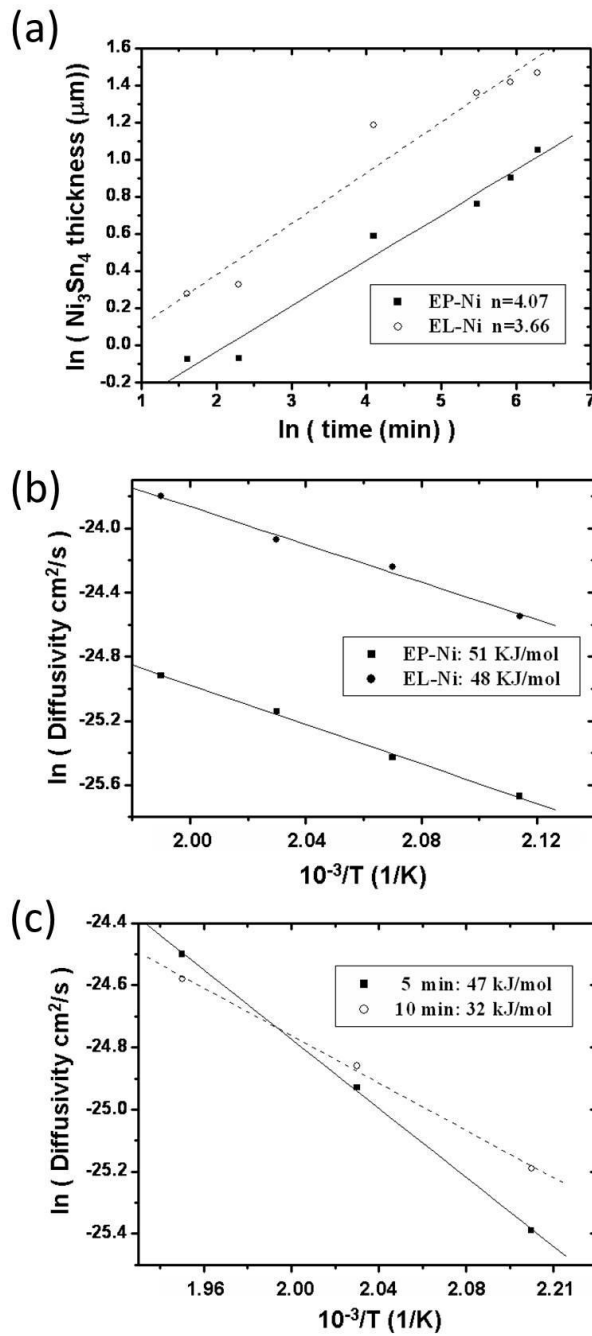


Figure 2-13 (a) The fitting curve of the time exponent for parameter n value of the IMC thickening process. (b) Arrhenius plot for metallization of both EP-Ni and EL-Ni using the data at 1 h of reflow duration. The activation energies were determined to be 51 kJ/mol and 48 kJ/mol for the IMC growth on EP-Ni and EL-Ni, respectively. (b) Arrhenius plot for the results published by Kim et al.[9], which is for eutectic Sn-Pb solder on bulk Ni. Data from reflow durations of both 5 min and 10 min were used.

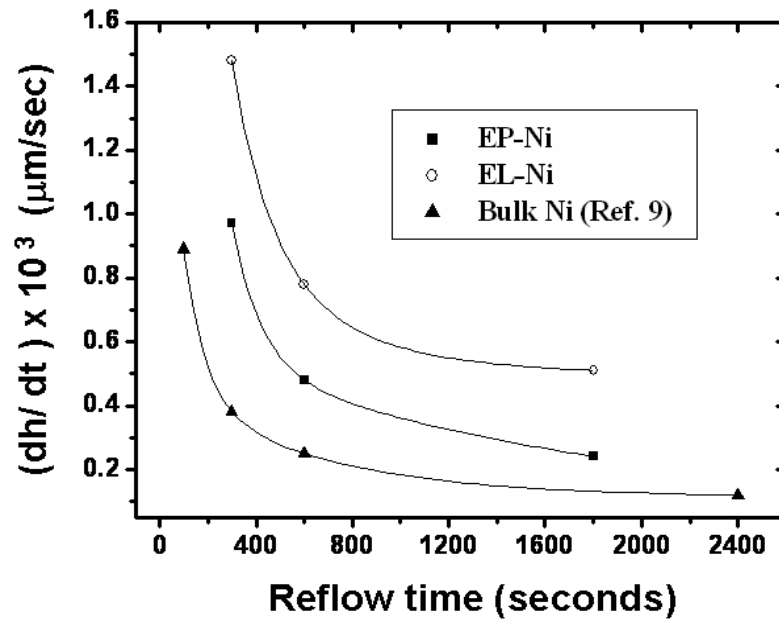
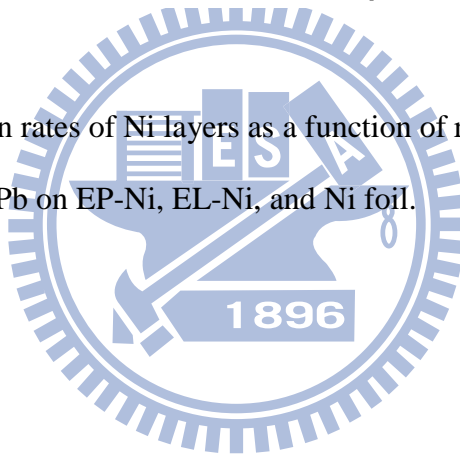


Figure 2-14 Consumption rates of Ni layers as a function of reflow time at 240°C for eutectic Sn-Pb on EP-Ni, EL-Ni, and Ni foil.



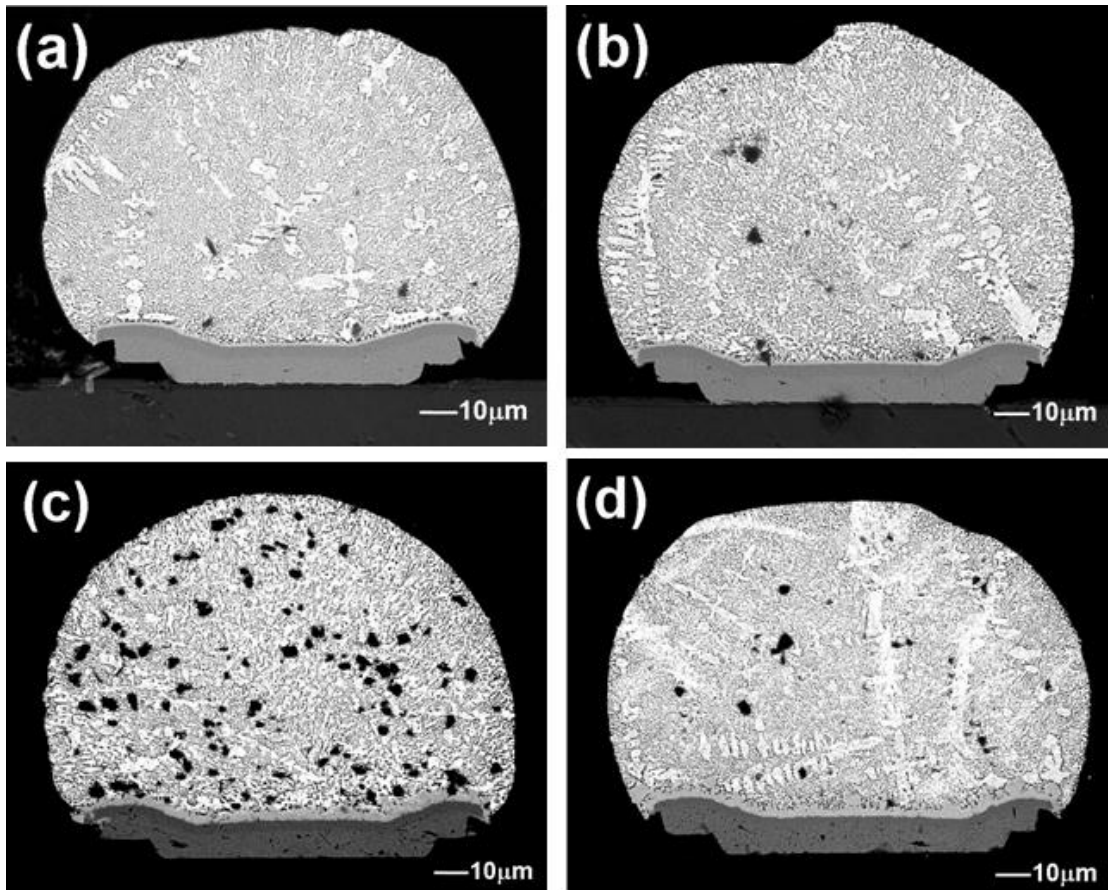


Figure 2-15 Cross-sectional SEM images showing morphology of Ni_3Sn_4 IMCs at the interface of the Sn-Pb solder and the EP-Ni UBM reflowed at 210°C for (a) 5 min, (b) 10 min, (c) 1 hr, and (d) 9 hrs.

Chapter 3 Measurement of Electromigration Activation Energy in Eutectic SnPb and SnAg Flip-chip Solder Joints with Cu and Ni Under Bump Metallization

3.1 Introduction

The electromigration (EM) of flip-chip solder joints has been regarded as a serious reliability issue [1,2], because it can lead to failure due to interfacial void formation and large intermetallic compound (IMC) formation inside solder joints [3-7]. Furthermore, because of the combination of the serious current crowding and the Joule heating effect which cause non-uniform temperature distribution inside solder joints [8], predicting the failure time of flip-chip solder joints is not a straightforward task. Choi *et al.* found that the measured mean-time-to-failure (MTTF), current stressing time till failure was much smaller at higher current density than that of the calculated values from the Black's equation [9]. They proposed that Black's equation should be modified due to the serious current crowding and the Joule heating effect during current stressing.

According to Choi *et al.*, the MTTF equation can be modified as

$$\text{MTTF} = A \frac{1}{(cj)^n} \exp \left[\frac{Q}{k(T+\Delta T)} \right] \quad (3-1)$$

where MTTF is the current stressing time till failure; A is the constant that contains a factor involving the cross-sectional area of the joints, j is the current density in ampere per centimeter square, n is the model parameter for current density, Q is the activation energy, T is the average temperature of the bump, and ΔT is the temperature increase due to the Joule heating effect in Al trace. The measurement of real temperature is critical in determining the activation energy, since temperature term and the activation

energy are located in the exponential term. Several studies have measured activation energy without calibrating the real stressing temperature [10-12], while others measured the bump temperature by placing a thermal couple or temperature crayon on the surface of Si die [10], which may deviate from the bump temperature. On the other hand, Stephen and his coworkers calibrated bump temperature by using a special Al trace design to measure the nearest stressing solder bump temperature. By utilizing temperature coefficient of resistance (TCR) property of Al trace itself, they can calibrate temperature more precisely than others. However, they used Daisy-chain structure, which cannot monitor the change in resistance of one bump, therefore, the failure criteria they used may not be able to detect the first stage of failure in solder bump [13].

In addition, the definition of EM failure can also influence the measurement of activation energy. In general, failure is defined as the resistance increases by 10-20% of its original resistance value to Al and Cu interconnects. For most EM studies of solder joints, Daisy-chain structures are adopted for EM testing, which includes solder bumps, Al traces in Si dies and Cu lines on the substrate. Several factors may contribute to resistance increase, including void formation, IMC formation, and phase separation in solder bumps. Yet, voids may form in the Al traces on the chip side if Daisy-chain structures are used.

Since the cross-sections of Al traces are about two orders smaller than those of solder bumps and Cu lines, the resistance of Al trace weights account for over 90% of Daisy-chain structure. Furthermore, it has been reported that Al traces may also receive EM damage during accelerated EM tests of solder bumps [14]. Therefore, the EM damage of Al traces may have significant influence on the measurement of EM failure time and activation energy. Thus, it is urgent to explore an approach to

measure activation energy so that the MTTF of solder joints can be predicted as precise as possible.

In this study, we utilize the temperature coefficient of resistivity (TCR) of Al traces as a temperature sensor to detect the real temperature in solder bumps during current stressing. In addition, Kelvin bump probes were employed to monitor the bump resistance during EM [15]. A failure criterion was defined as the bump resistance increased to 20% of its original value. Microstructure analysis was performed to examine the failure mechanism, so that the physics meaning of the EM activation energy could be obtained.

3.2 Experimental Procedures

A test layout was designed to measure the resistance of solder bumps and the resistance of their neighboring Al traces, as shown in Figure 3-1(a). The solder joints consist of eutectic SnPb and SnAg solder bumps with electroplated 5 μm -Cu thick UBM, as depicted in Figure 3-1(b). The other set of samples consist eutectic SnAg with 5 μm -Cu/ 3 μm -Ni UBMs, donated as Cu-Ni UBMs, as illustrated in Figure 3-1(c). The diameter of the solder joint is 130 μm . They have a 70 μm high solder bump and a contact opening with of diameter of 85 μm on the chip side. The metallization on the FR5 substrate is 0.05 μm Au/5 μm electroless Ni. The four bumps were connected by Al traces and the six nodes were labeled from N1 to N6. Current was applied through nodes N3 and N4, as illustrated in the Figure 3-1(a). The voltage change of bump B3 can be measured through node N5 and N6. In addition, the resistance for the middle segment of the Al trace between B2 and B3 can also be monitored during EM by nodes N1 and N6. To conduct the EM test, current stressing was carried out at 135°C, 150°C, and 165°C on a hot plate. A constant current of 0.8A was passed through the bumps with Cu UBMs, producing a nominal current density

of $7.0 \times 10^3 \text{ A/cm}^2$. On the contrast, a constant current of 0.9A was applied through the bumps with Cu/Ni UBMs, producing a nominal current density of $7.9 \times 10^3 \text{ A/cm}^2$ because the EM resistance is higher in these bumps.

The TCR of the middle Al trace was calibrated before the EM test to serve as a temperature sensor. The Al resistance under different temperatures was measured by applying 0.2A in it. Joule heating, which was confirmed by an infrared microscope, was less than 1°C under this condition. Then the TCR of the middle Al trace could be obtained. Therefore, the real temperature can be detected during an accelerated EM test by simultaneously measuring the resistances of the middle Al trace.

The EM failure criterion here is defined as 20% increase of its original resistance for the bump with downward current stressing. The microstructure of the solder bump was examined by a scanning electron microscope (SEM, JEOL 6500). A backscattered electron image (BEI) of SEM was used to examine the morphology of the cross-sectioned SnPb samples and the intermetallic compounds. Also, the compositions of the solder joints and the IMC were analyzed quantitatively by energy dispersive spectroscopy (EDX).

3.3 Results and Discussion

3.3.1 Electromigration Test

Figures 3-2(a) to 3-2(c) show the cross-sectional SEM images microstructures for the SnAg/Cu, SnPb/Cu and SnAg/CuNi bumps, respectively before current stressing. Interfacial IMCs are labeled in the Figures. Cu-Sn IMCs form in the SnAg and SnPb solder bumps with Cu UBMs in the chip side, whereas Ni_3Sn_4 IMCs present in the SnAg solder bump with a Ni UBM. Since the EM damage generally occurred on the chip side due to the current crowding there. In this study, EM failure is defined

when the bump resistance increase reaches 20% of its initial value. This can ensure that the measured EM failure time is related to EM damage in the solder bump only. The occurrence of EM damage in Al traces and in Cu lines is excluded.

In solder joints with Cu UBMs, the formation of tiny voids and the consumption of the Cu UBM were observed after the EM failure. The average failure time for the SnAg and the SnPb bumps under three stressing conditions are listed in Table 3-1. Figures 3-3(a) to 3-3(c) represent the cross-sectional SEM image for the failed SnAg/Cu bump with downward electron flow at 135°C, 150°C, and 165°C, respectively. Some of the 5- μm Cu UBM was consumed and were transformed into Cu-Sn IMCs at 135°C in Figure 3-3(a). On the other hand, the Cu layer was almost consumed and formed Cu-Sn IMC at 150°C and 165°C, as illustrated in Figures 3-3(b) and 3-3(c). Some tiny voids formed at the interface of the IMCs and the solder when stressed at 135°C and 150°C. But the void location switched to the interface between the Al trace and Cu-Sn IMC at 165°C, as shown in Figure 3-3(c). Current crowded into the solder bump from the upper-left corner of the bump, causing the voids to start to form there and higher temperatures also induced rapidly Cu dissolution and migration to the substrate side. Both IMC and void formation contribute to the rising of bump resistance.

For EM in the SnPb solder joints, phase segregation also takes place in addition to IMC and void formation. Figures 3-4(a) to 3-4(c) show the cross-sectional SEM images for the bump stressed at 135°C, 150°C, and 165°C, respectively. Similarly, the bump resistance reached 20% of its original value. The Cu UBM was consumed at the current crowding region on the upper-left corner. Yet, there was residual Cu far away from the current crowding/hot spot region. The Cu consumption rate in SnPb solder appears lower than that in the SnAg solder due to smaller Cu solubility in SnPb solder [16]. In addition, the IMCs migrated to the substrate side. Therefore, tiny voids

formed at the interface of the Ti layer and the solder. Phase segregation of Sn-rich and Pb-rich phase in the solder bump might contribute a few percentage increases in resistance [17]. Phase separation is not very clear under current stressing at 135°C as shown in Figure 3-4(a). Pb atoms act the dominate diffusion species when the testing temperature is higher than 150°C. Therefore distinct phase separation can be observed in Figures 3-4(b) and 3-4(c), but not in Figure 3-4(a). In short, similar to SnAg bumps, IMC and void formation accounts for most of the increasing resistance.

Different failure mechanism was observed in the SnAg/Cu-Ni solder joints during EM test. Figures 3-5(a) through 3-5(c) depict the failed bump stressed at 135°C, 150°C, and 165°C, respectively. For the bumps stressed at 135°C, no obvious consumption of Ni UBM was observed. Instead, voids formed at the interface of the Ni_3Sn_4 and the SnAg solder. At higher stressing temperatures, the consumption of the Cu and Ni UBMs may be found occasionally, as indicated by one of the arrows in Figure 3-5(b). As stressing temperature increases, the consumption of Cu and Ni UBM becomes more obvious, as presented in Figure 3-5(c). However, it seems that void formation and propagation dominates the EM failure in the SnAg/Cu-Ni system.

Therefore, the Kelvin probes are able to detect the early damage of the EM for various samples and different stressing condition. In addition, the detected increase in resistance reflects some specific microstructure changes in solder bumps. In Cu UBM system, the main failure mode goes to Cu consumption; however, void formation serves the major failure mechanism in Cu-Ni UBM system.

3.3.2 TCR Effect Measurement and Joule Heating Effect

The central Al trace was adopted as a temperature sensor to measure bump resistance. To ensure that the temperature in the central Al trace was very close to that of the stressed bump, infrared microscopy was employed to measure the temperature

distribution in the Al trace during current stressing. Figure 3-6(a) shows the temperature distribution in the central Al trace and the Al pads directly above bumps B2 and B3 stressed at 0.8A at a hot stage maintained at 100°C. Because the width was as wide as 80 μm, the local Joule heating effect in the Al trace was not as serious as that in the narrower traces [8]. The average temperatures in the five white rectangles were 109.2°C, 109.9°C, 109.9°C, 109.8°C and 109.2°C. Figure 3-6(b) also showed the measured Al pad temperature and Al trace temperature versus with stressing current by using IR. The temperature different between Al pad and Al trace increased when we increased the stressing current. The difference reached to 1.83°C when the stressing current raised to 1.2 A. Under the stressing condition of 0.8A and 0.9A, the temperature difference are less than 1°C. Therefore, the temperature sensor by using central Al trace was able to detect bump temperatures during current stressing.

To measure the Joule heating effect accurately, the TCR of the central Al trace was calibrated in an oven. As the temperature increases, the amplitude of the atomic vibrations increases, and consequently the flow of electrons are impeded. Therefore, the resistivity of a metal increases with temperature. Typically, the TCR can be assumed to be linear and can be simply expressed as:

$$R = R_0(1 + \alpha \Delta T) \quad (3-2)$$

where R_0 is the resistance at 50°C; α is the TCR coefficient; ΔT is the temperature difference and R is the resistance. To obtain the relationship between the resistance of the Al trace and temperature of the Al trace, the resistance of the Al trace was measured against various oven temperatures to obtain the TCR coefficient, as shown in Figure 3-7. The TCR coefficient of the Al trace is obtained as $4.08 \times 10^{-3} \text{ K}^{-1}$, and $4.03 \times 10^{-3} \text{ K}^{-1}$ for SnAg and SnPb packages with Cu UBM system, respectively. On the other hand, the TCR coefficient is calculated as $3.95 \times 10^{-3} \text{ K}^{-1}$ for SnAg packages with Cu-Ni UBM. These values are very close to the value ($3.9 \times 10^{-3} \text{ K}^{-1}$) of bulk Al.

The real temperature during current stressing can be obtained by using this approach. The temperatures were 157°C, 174°C, and 186°C for the SnAg solders with Cu UBMs; whereas they were 150°C, 168°C, and 180°C for the SnPb solders with Cu UBMs. On the other hand, the temperature was 156°C, 170°C, and 184°C for the SnAg solders with Cu-Ni UBMs. These data are also tabulated in Table 3-1. The temperatures increased by about 20°C and 16°C in the SnAg and SnPb solder bumps, respectively. The reason for the higher Joule heating effect in SnAg packages is attributed to the thinner Si die. The die thickness of the SnAg and SnPb packages is 250 μm and 750 μm, respectively. Solder joints with a thinner die have worse heat dissipation ability than those with a thicker die. Yet, it is not clear why the calibrated temperature would not increase with the increasing in the hot plate temperature.

3.3.3 Activation Energy Fitting

To measure the activation energy, at least six samples were stressed in each condition. The average failure time for SnAg solder joints with Cu UBMs was 358 h, 180 h and 56 h at 157°C, 174°C, and 186°C, respectively. Activation energy for electromigration can be obtained by using Eq. (3-1). Figure 3-8(a) shows the plot of $\ln(\text{MTTF})$ against $10^3/T$ with un-calibrated and calibrated temperatures for the SnAg solder. The average failure time is adopted as MTTF in this study. The activation energy increased from 0.94 eV to 1.06 eV with the consideration of Joule heating effect. Figure 3-8(b) depicts the results for SnPb solder joints with Cu UBMs. The average failures time was 342 h, 144 h and 83 h at 150°C, 168°C, and 180°C, respectively. The measured activation energy changed from 0.72 eV to 0.87 eV after the temperature calibration, and the difference was as large as 20%. On the other hand, in SnAg/Cu-Ni system, the average failure time was 431 h, 173 h and 105 h at 156°C,

170°C and 184°C, respectively. The measured activation energy changed from 0.65 eV to 0.85 eV after the temperature calibration, as illustrated in Figure 3-8(c).

The difference in activation energy may have a significant influence on predicting MTTF in solder joints. Take SnPb joints with Cu UBMs for example, at 100°C, the estimated MTTF ($E_a=0.87$ eV) was 110 times longer than that when E_a was taken as 0.72 eV by using Eq. (3-1). Therefore, temperature calibration appears to be very important in the measurement of activation energy. With this approach, the physical meaning of activation energy is evident. Since Kelvin bump probes were employed to monitor the resistance in the solder bumps, the resistance changes solely originated from the damage in the solder bump. The resistance changes in the wiring trace and in the contacts can be excluded.

As shown in Figure 3-3 to 3-4, both IMC and void formation contribute to increasing resistance. Thus, the measurement of activation energy mainly involves the processes of Cu-Sn IMCs formation and void formation on the chip side. The resistivities for the Cu, SnAg, SnPb, and Cu_6Sn_5 were 1.7, 12.3, 14.6, and 17.5 $\mu\text{m}\cdot\text{cm}$, respectively. Therefore, the formation of Cu_6Sn_5 IMCs results in increasing resistance. On the other hand, the voids were tiny and not discontinuous. It is speculated that these voids do not contribute much to the increase of resistance. Lee et al. studied the solid-state reaction between solders and Cu UBM [17], and they reported that the activation energy for the formation of Cu_6Sn_5 IMC is 1.05 eV and 0.94 eV for eutectic SnAg and SnPb solders, respectively. These values are very close to the values reported in this study. Therefore, the measured activation energy of EM is mainly associated with the formation of Cu_6Sn_5 IMCs in Cu UBM system.

However, the activation energy we obtained (0.85 eV) in Cu-Ni UBM system is larger than the formation energy of Ni_3Sn_4 IMCs, which is about 0.17 eV [18] and the Sn selfdiffusion activation energy, which is about 0.28 eV. As shown in Figure 3-5, no

obvious Ni consumption during the early stage of EM. The EM was mainly associated with void formation and propagation. Therefore, the measured activation energy for eutectic SnAg with Cu-Ni UBMs is much larger than the Ni_3Sn_4 IMC formation energy and the void formation energy, and is mainly related to void propagation.

3.4 Summary

In summary, this study provides an excellent approach to measure the activation of EM in flip-chip solder joints. Using Kelvin bump probes, the bump resistance can be measured accurately and EM failure is defined as the increase of bump resistance to 20% of its original value. In addition, the Kelvin probes were also employed to measure the resistance of the central Al trace. The measured activation energies were 1.06 eV and 0.87 eV for the SnAg and SnPb bumps with Cu UBMs, respectively. The values were about 20% bigger than those without calibrating real temperatures in solder bumps and very close to the formation activation energy of Cu-Sn IMCs. On the other hand, the measured activation energy was 0.85 eV for the SnAg bumps with Cu-Ni UBMs, which is mainly related to the void formation in solder.

3.5 References

1. International Technology Roadmap for Semiconductors: Semiconductor Industry Association, San Jose, CA, 2003.
2. K. N. Tu, J. Appl. Phys. **94**, 5451 (2003).
3. L. Zhang, S. Q. Ou, J. Huang, K. N. Tu, S. Gee, and L. Nguyen , Appl. Phys. Lett. **88**, 012106 (2006).
4. F. Y. Ouyang, K. Chen, K. N. Tu, and Y. S. Lai , Appl. Phys. Lett. **91**, 231919 (2007).
5. T. L. Shao, Y. H. Chen, S. H. Chiu, and C. Chen , J. Appl. Phys. **96**, 4518 (2004).
6. S. H. Chiu and C. Chen, Appl. Phys. Lett. **89**, 262106 (2006).
7. Y. H. Lin, C. M. Tsai, Y. C. Hu, Y. L. Lin, and C. R. Kao , J. Electron. Mater. **34**, 27 (2005).
8. S. H. Chiu, T. L. Shao, and C. Chen, Appl. Phys. Lett. **88**, 022110 (2006).
9. W. J. Choi, E. C. C. Yeh and K. N. Tu , J. Appl. Phys. **94** (9), 5665 (2003).
10. S. H. Chae, X. F. Zhang, K. H. Lu, H. L. Chao, P. S. Ho, M. Ding, P. Su, T. Uehling and L. N. Ramanathan, Proceedings of the 56th Electronic Components and Technology Conference, p. 650 (2006).
11. Y. S. Lai, K. M. Chen, C. L. Kao, C. W. Lee, and Y. T. Chiu , Microelectronics Reliability **47**, 1273 (2007)
12. J. H. Lee, G. T. Lim, Y. B. Park, S. T. Yang, M. S. Suh, Q. H. Chung and K. Y. Byun, J. Korean Phys. Soc. **54** (5) 1784, (2008).
13. S. Gee, N. Kelkar, J. Huang and K. N. Tu, Proc. of IPACK 2005, San Francisco, CA, 2005.
14. Y. W. Chang, S. W. Liang and C. Chen, Appl. Phys. Lett. **89**, 032103 (2006).
15. K. Zeng and K. N. Tu , R38, **55** (2002).
16. C. K. Chou, C. A. Chen, S. W. Liang, and C. Chen, J. Appl. Phys. **99**, 054502

(2006).

17. T. Y. Lee, W. J. Choi, K. N. Tu, J. W. Jang, S. M. Kuo, J. K. Lin, D. R. Frear, K.

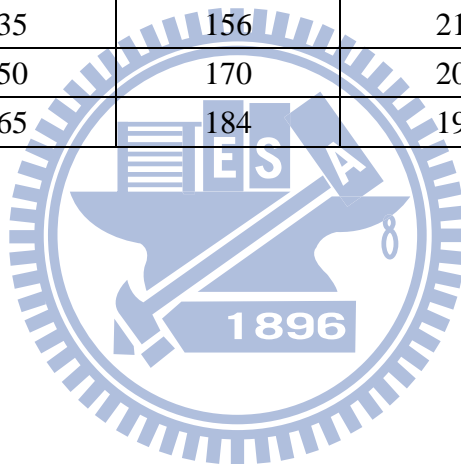
Zeng and J. K. Kivilahti, *J. Mater. Res.* **17** (2) 291 (2002).

18. M. O. Alam and Y. C. Chan, *J. Appl. Phys.* **98**, 123527 (2005).



Table 3-1 Calibrated temperature and the average failure time of SnAg/Cu, SnPb/Cu and SnAg/CuNi solder bumps under three testing hot plate temperatures.

	Hot plate temperature (°C)	Calibrated temperature (°C)	Temperature increase (°C)	Average failure time (hr)
SnAg/Cu (0.8 A)	135	157	22	358
	150	174	24	180
	165	186	21	56
SnPb/Cu (0.8 A)	135	150	15	342
	150	168	18	144
	165	180	15	83
SnAg/CuNi (0.9 A)	135	156	21	431
	150	170	20	173
	165	184	19	105



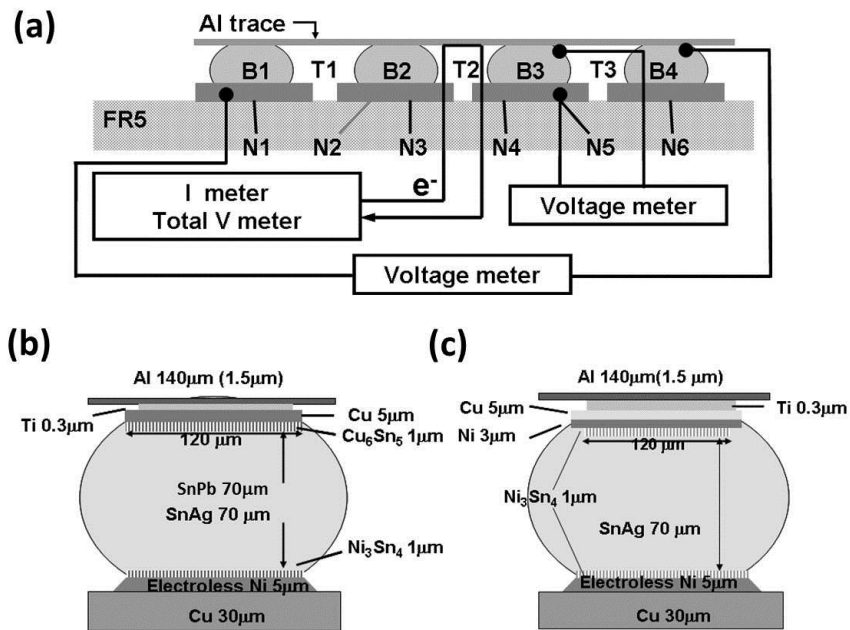


Figure 3-1 (a) Cross-sectional schematic of the layout for Kelvin bump probes. The Al trace connected all four solder bumps together. Cross-sectional schematic for the solder bumps with a (b) Cu UBM and (c) Cu/Ni UBM.

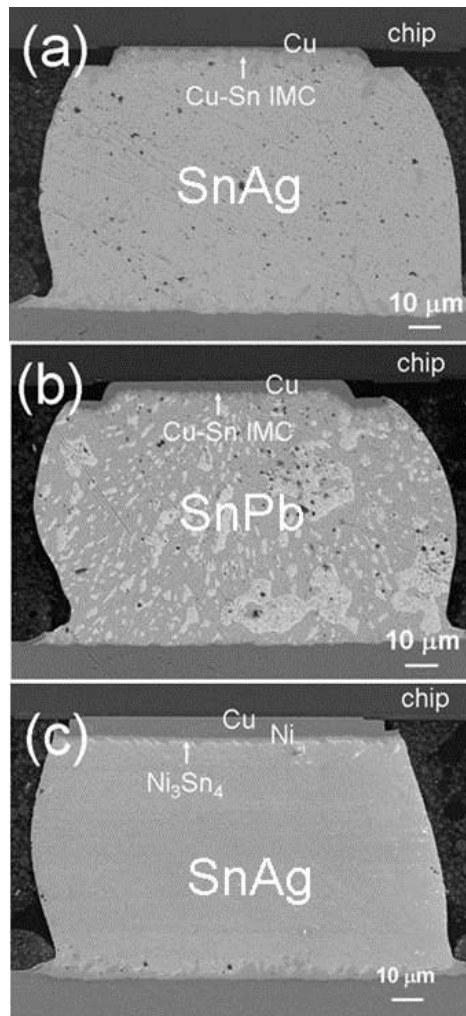


Figure 3-2 Backscattered SEM images for solder bumps before current stressing. (a) SnAg bump with a Cu UBM, (b) SnPb bump with a Cu UBM, and (c) SnAg bump with Cu–Ni UBM.

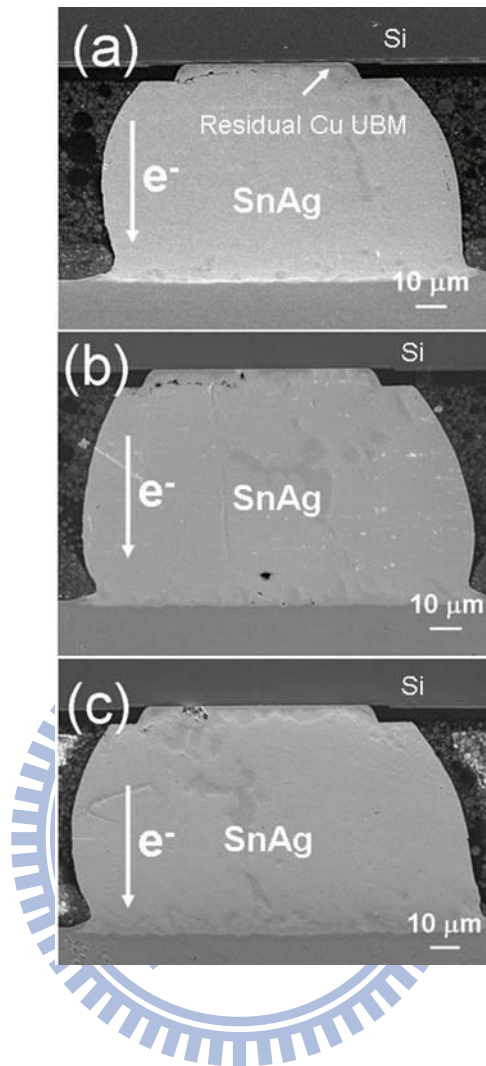


Figure 3-3 SEM images of the SnAg bumps with Cu UBMs stressed by a downward current of 0.8 A at (a) 135°C, (b) 150°C, and (c) 165°C. The bump resistance increased by 20% or more.

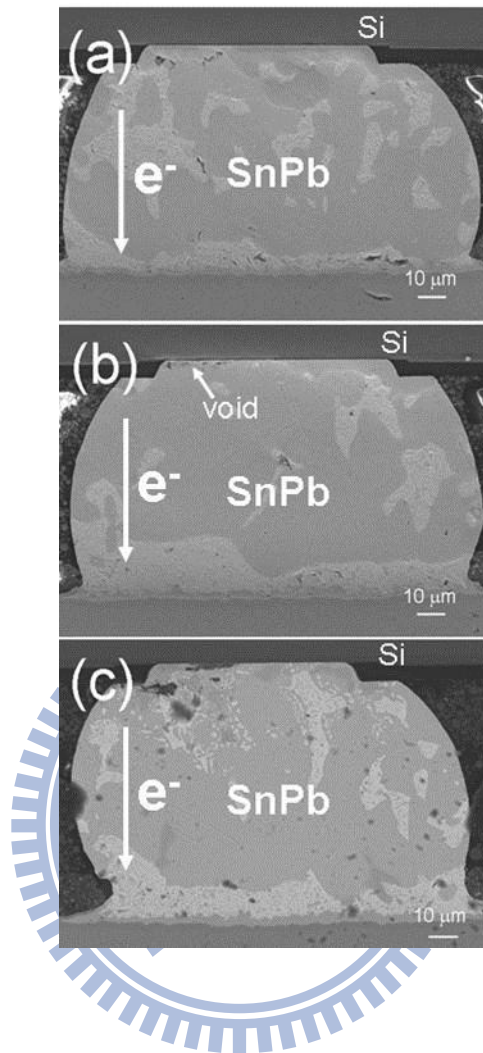


Figure 3-4 Backscattered SEM images of SnPb bumps with Cu UBMs subjected to 0.8 A downward current stressing at (a) 135 °C, (b) 150°C, and (c) 165°C.

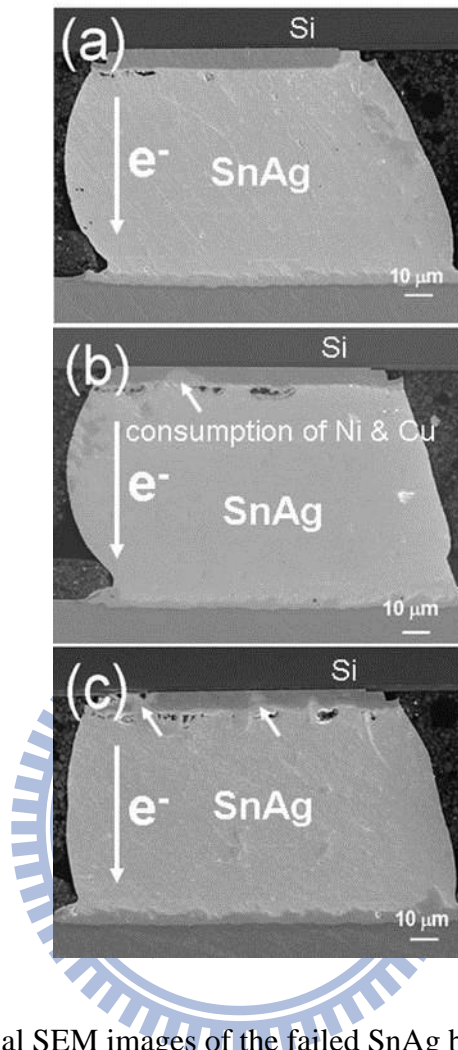


Figure 3-5 Cross-sectional SEM images of the failed SnAg bumps with Cu–Ni UBMs subjected to downward current stressing of 0.9 A at (a) 135°C, (b) 150°C, and (c) 165°C.

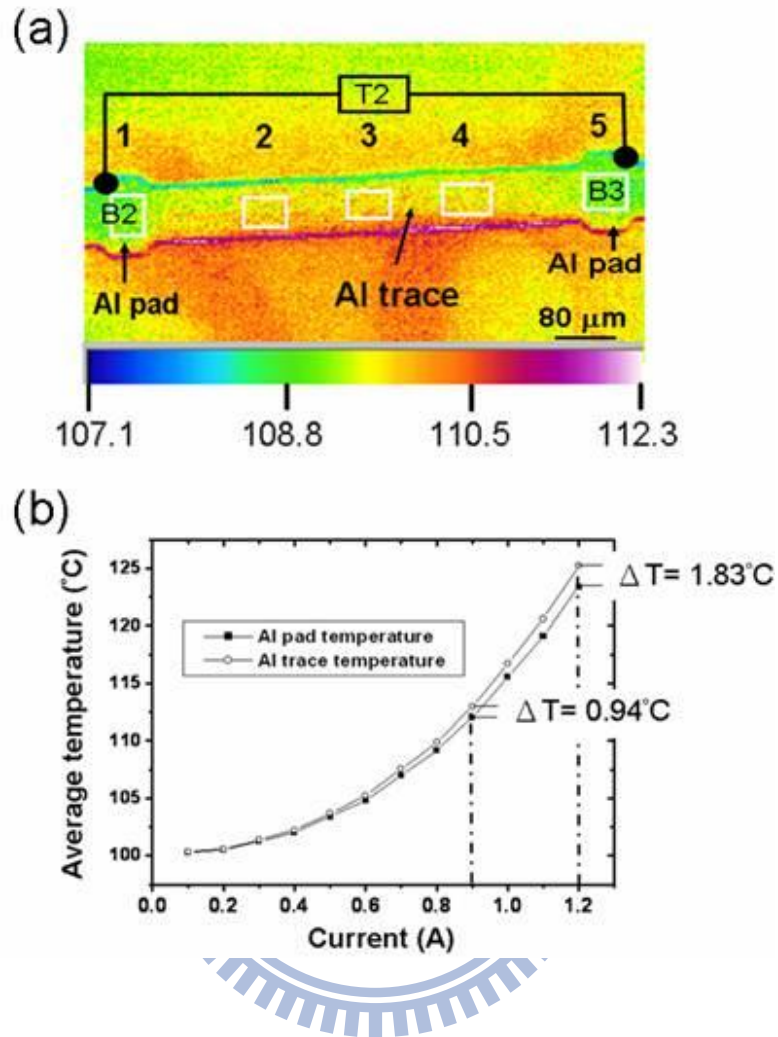


Figure 3-6 (a) Temperature distributions in the central Al trace and the Al pad measured by the IR microscope when powered by 0.8 A at 100°C. Bumps B2 and B3 located directly below the left Al pad and right pad respectively. (b) The measured Al-pad and Al-trace temperatures under various applied currents.

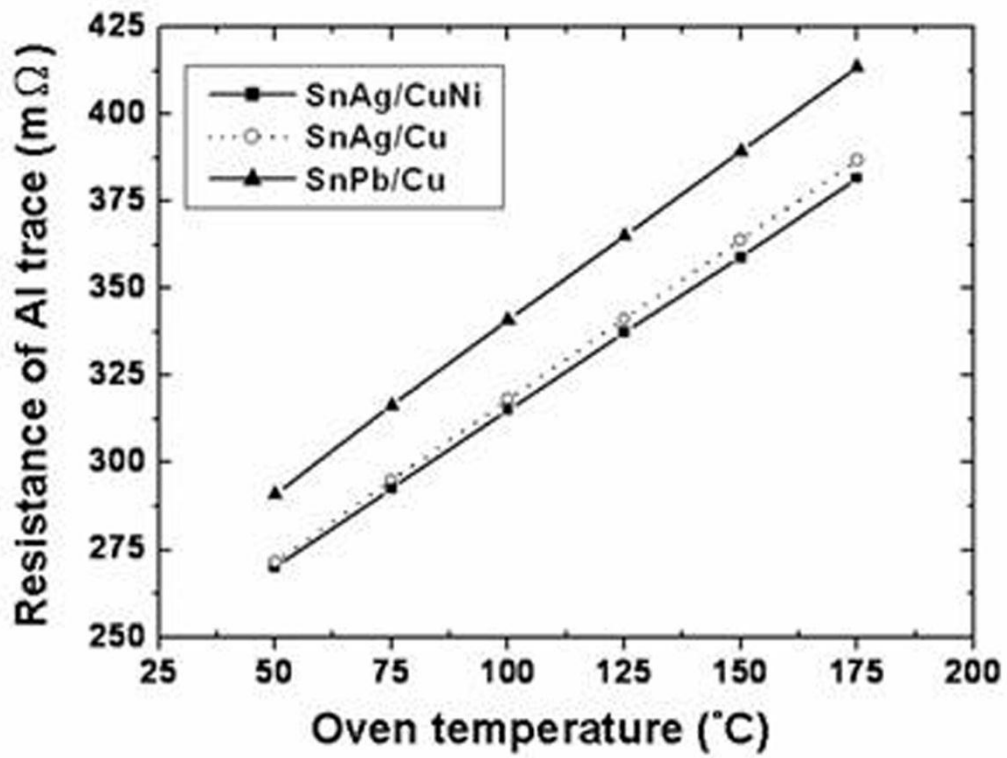


Figure 3-7 Plot of the measured resistance of the central Al trace against oven temperature for the three samples. The TCR coefficients can be obtained from the slopes of these curves.

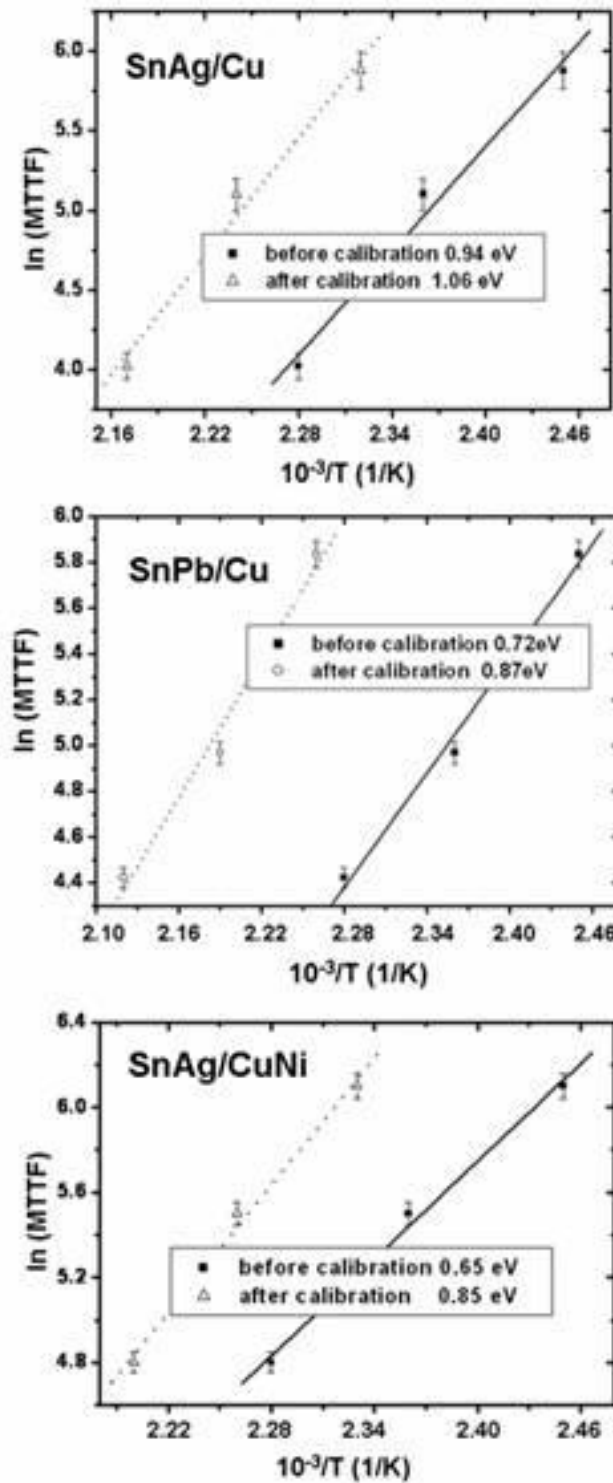


Figure 3-8 Plots of MTTF against $10^{-3}/T$ for the (a) eutectic SnAg bumps with Cu UBMs, (b) eutectic SnPb bumps with Cu UBMs, and (c) eutectic SnAg solder with Cu–Ni UBMs.

Chapter 4 Effect of UBM Structure on Electromigration Life Time of Sn-Ag Solder Joints

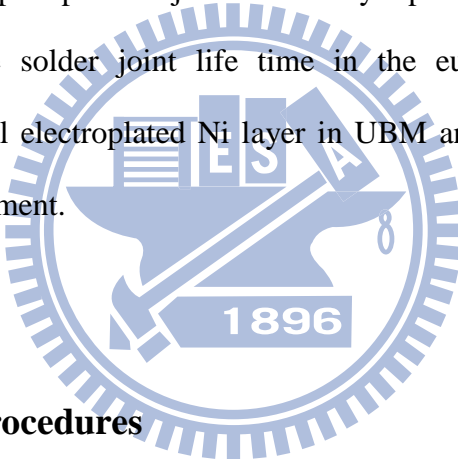
4.1 Introduction

Owing to the shrinking flip chip solder joint diameter, usually less than 50 μm , the EM has been recognized as an important reliability issues [1-6]. The serious current crowding effect is one of the major failure mechanisms in EM,[7] which causes void formation or enhances dissolution of the thick-film UBM in flip chip solder joints [8-12]. Void formation and the consumption of UBM to form IMC inside solder bump resulted in the most persistent and serious reliability issues in flip chip solder joints. As the result, the selection of an appropriate UBM layer becomes an important process for developing a reliable flip chip joint, especially with the adoption of the Pb-free solders due to environmental concerns. For example, as the bump shrinks, the thickness of UBM does not scale down with solder size, and the extremely fast dissolution rate of UBM into Sn-based solder induces the serious intermetallic compound (IMC) formation [13].

In order to minimize the current crowding effect, thick Cu UBM has been chosen for the SnAg solder joint [14,15]. The EM reliability was significantly improved after adopted thicker Cu UBM to against current crowding by the current redistribution [14]. The EM can be avoided by limiting the current crowding effect in the solder region. By utilizing the simulation results, Liang *et al.* found that joints with a thicker Cu UBM exhibited a lower maximum current density and hot spot temperature; the current crowding and local Joule heating effect vanished when the Cu UBM thickness was over than 50 μm [15]. Moreover, Lin *et al.* also reported that joints with a thicker Ni UBM tend to have longer average life time [16]. The combination of current

crowding and local Joule heating near the entrance point induced asymmetric Ni UBM consumption. Therefore, once the Ni UBM was exhausted in a certain region, this region became nonconductive and resulted in failure. On the other hand, Ni, as well as, is much more resistant to dissolution when in contact with solder and is less susceptible to fail through dissolution as UBM layer [12]. Based on their observations, it is a reasonable assumption that the design of UBM is pivotal for the solder joint life time. Therefore, by integrated thick Cu and Ni, this thick UBM structure might be able to extend solder joint life time.

However, the detailed study of the effects of the UBM structure on failure mechanism in Pb-free flip chip solder joints are rarely reported. This chapter reports a method to enhance the solder joint life time in the eutectic SnAg system by introducing an additional electroplated Ni layer in UBM and a possible mechanism for the life time improvement.



4.2 Experimental Procedures

In order to investigate the EM process, a special layout of four solder joints which can be monitored by Kelvin probes [17] was adopted, as illustrated in Figure 4-1(a). On the chip side, a $0.12\ \mu\text{m}$ Ti layer was sputtered as an adhesion/diffusion-barrier layer between the UBM and the Al trace which connects the four bumps together. A bump height of $70\ \mu\text{m}$ eutectic SnAg solder joints with $5\ \mu\text{m}$ Cu/ $3\ \mu\text{m}$ Ni bilayer UBM, as well as, $5\ \mu\text{m}$ single layer Cu UBM were prepared as shown in Figures 4-1(b) and 4-1(c). The diameter of the solder joint is about $150\ \mu\text{m}$ and they were joined to an FR5 substrate. The dimension of Al trace in the chip side was $100\ \mu\text{m}$ wide and $1.5\ \mu\text{m}$ thick, while the dimension of the Cu lines on the substrate was $25\ \mu\text{m}$ thick and $100\ \mu\text{m}$ wide. On the substrate side, six Cu nodes were

fabricated and labeled as Node N1 through N6. By these six nodes, the resistance for the middle segment of the Al trace, Bump 2 and Bump 3 can also be monitored.

IR microscopy was employed to observe the hot spot during current stressing. Prior to current stressing, the emissivity of the specimen was calibrated at 100 °C. After calibration process, a desired current was applied. Afterwards, the temperature measurement was performed to record the temperature distribution at the steady state. Current stressing was carried out at different temperatures from 135 °C, 150 °C to 165 °C on a hot plate. Current stress was applied to the bumps with the current density of 7.0×10^3 A/cm² for Cu UBM, and on the other hand, 7.9×10^4 A/cm² for Cu/Ni UBM system at the UBM opening. Since those data is useful to take into consideration when it is reasonable in counting for Black equation. When it first stressed with 7.0×10^3 A/cm² for Cu UBM, the failure time was too short, especially under 165°C, which was not sufficient for using in Black equation. Therefore, two different kinds of current densities here were used.

The temperatures in the solder joints could also be mapped by a QFI thermal IR microscope with 0.1 °C temperature resolution and 2 μm spatial resolutions. The microstructure of the interfacial regions between the solders and UBMs were examined by a SEM. Moreover, the compositions of the solder joints and the IMCs were analyzed quantitatively by EDX.

Three-dimensional finite element analysis (FEA) was performed to simulate the current-density distribution in the solder joint. The dimension setting of the Al trace, pad opening, and Cu line were identical as the dimension of the flip-chip sample. The IMC formed between the UBM and the solder was also considered in the simulation models. The Ni layers on the chip and the substrate sides were assumed to consume 0.5 μm and form 1.0 μm of Ni₃Sn₄ IMC. Layered IMCs, Ni₃Sn₄, were used in this simulation for the Ni₃Sn₄ to avoid difficulty in meshization. On the other hand,

1.0 μm Cu_6Sn_5 formed at the chip side on Cu UBM system. The resistivity and thermal conductivity values of the materials used in the simulation are listed in Table 5-1. The model used in this study was SOLID69 eight-node hexahedral coupled field element using ANSYS simulation software. The size of the element in the solder bump was 3.0 μm .

4.3 Results and Discussion

4.3.1 Different Bump Resistance Increase and the Corresponding Microstructure

Images

Figures 4-2(a) and 4-2(b) show the cross-sectional SEM image of the eutectic SnAg solder joint with Cu/Ni and Cu UBM before current stressing, respectively. The increase in bump resistance during EM can be precisely measured using Kelvin bump probes, and it can also monitor the void formation and microstructure change during EM test. Figure 3 shows the total resistance of the stressing circuit as a function of stressing time until device failure; in this paper, we define the failure criteria as the resistance of Bump 3 increases to 20 % of its original value. After 44-hr current stressing at $7.0 \times 10^3 \text{ A/cm}^2$ and 150°C , as shown in Figure 4-3(b), the resistance of Bump 3 in Cu UBM system reached the failure criteria, while it took 160 hrs for Cu/Ni system under higher testing condition, shown in Figure 4-3(a). The profile in Figure 4-3(a) rose slowly at the initial stage, the stressing time within 85 hrs, but changed dramatically afterwards. On the other hand, profile in Figure 4-3(b) increased sustained. Indeed these two slopes in Figure 4-3(a) represented different stage, for instance, void nucleation or the propagation. The detailed mechanisms for the different slopes represented in Cu/Ni UBM system is still under investigated. Under our testing conditions, Cu/Ni UBM system has the longer failure time than the Cu

UBM system. The corresponding SEM images are shown in Figures 4-4(a) and 4-4(b). Void formation was clearly observed near the entrance point in both Cu/Ni and Cu systems till the resistance of bump 3 reached to 1.2 times of its original value. The main difference between these two systems is the void formation location. For Cu/Ni UBM system, the voids appeared near the interface between solders and intermetallic compounds (IMC); however, voids formed near the interface at the Cu UBM and Al trace after the consumption of thick Cu UBM at the upper-left corner, which is the current crowding region.

The EM failure mechanism in these two systems can be understood in two different ways. In Cu/Ni UBM system, voids first formed at the interface between IMCs and solders, and then propagated along the interface known as the pancake type void which has been reported in the previous literatures [18,19]. Once the Ni atoms were completely depleted at certain regions; the upper Cu dissolved locally into the solder and became IMC as well. The location where the upper Cu UBM was reacted to IMC was specified by an arrow in Figure 4-4(a). The voids propagated along the interface beneath IMC at some place, which can be observed at the middle of UBM and solder interface. However, in the single layer Cu UBM system, the Cu atoms first dissolved at very high rate by interstitial diffusion [20]. The fast reaction causes the poor interface contact and at least 5~7 % bump resistance increase. Therefore, EM lifetime becomes shorter in Cu single layer UBM system.

Furthermore, a higher Cu solubility in Pb-free solders may also facilitate the EM of Cu to enhance the formation of Cu-Sn IMCs and resulted in a shorter lifetime of Cu UBM system. It was reported that the solubility of Cu in eutectic SnPb at 220 °C is 0.18 wt. %, whereas it reaches 1.54 wt. % in Pb-free solders at 260 °C [21]. The thermal distribution will be further discussed later.

Once the resistance of Bump 3 increased over than 20%, the damage spreads out

along the interface dramatically and quickly. In our study, the solder joint with Cu/Ni UBM failed after current stressing for 1200 hrs under 150°C. The failure definition here referred to the open of the circuit which is made up by one pair of solder bump and Al trace. On the other hand, it takes only 407 hrs for solder joint with Cu UBM under the same temperature with lower current density. Such large difference implied that SnAg solder with Cu/Ni UBM certainly increases the failure time.

To further examine the effect of UBM on EM life time, stressing time was prolonged to 100% bump resistance increase of its original value and to the open failure as well. Figures 4-5(a) and 4-5(b) show the SEM images of Cu/Ni and Cu UBM system respectively after the resistance of Bump 3 increases to 100% of their original value. The corresponding bump resistances of the stressing circuit as a function of stressing time for CuNi UBM system is shown in Figure 4-6. As mentioned before, once the local Ni was consumed completely, the upper Cu UBM would react with solder quickly and turn UBM to Cu-Ni-Sn IMC. In Figure 4-6, most of UBM reacted with solder and became IMC after current stressing and resulted in poor attachment with upper Al trace. It can be divided into three parts as shown in Figure 4-6(a). The first part was denoted as stage I which the bump resistance increased from $1.25 \text{ m}\Omega$ to $1.5 \text{ m}\Omega$ and represented 1.2 rise. This stage I lasted for 400 hrs and void formation was suggested to be the major factor. Stage II lasted about 200 hrs and the followed by a large rate of bump increase afterward. It is suggested that void propagation and UBM dissolution resulted in the following bump resistance increase. Similarly, void formation can also be observed clearly from Figure 4-6. The void propagated along the interface between solder and IMC and almost passed through the UBM opening. Those referred to the increase in bump resistance. Serious void formation in Cu UBM system can be obtained as well from Figure 4-5(b). In addition to the large void formation between solder and IMC interface, it can be also

observed at the interface between UBM and Al trace, which caused by the dissolution of Cu UBM. Compared with the failure in early stage, as shown in Figure 4-4(b), there was less residual Cu left behind and large void extend across the solder. Cu dissolution and void formation both contributed to the increase in bump resistance.

Furthermore, Figure 4-8 show the resistance of the stressing circuit as a function of stressing time till open failure and the corresponding SEM images. Based on Figure 4-8, it took 1500 hrs for Cu/Ni UBM system to fail. But for Cu UBM system, it took 154 hrs to reach failure under the same condition. We will have a more detail discussion by current distribution and temperature simulation results. Not only the current crowding effect but also Joule heating effect, the fast reaction rate and dissolution rate of Cu into solder induced much shorter life time.

4.3.2 Joule Heating Effect

In addition to the current crowding effect, Chiu [22] *et al.* reported the Joule heating effect, observed along with the current crowding, using infrared microscopy. The temperature difference between the hot spot near the current entrance point and the solder can reach up to 9.4°C during the current stressing. Therefore, the hot spot should be considered as an important factor affecting the solder joint life time. To overcome the difficulty of measuring the temperature distribution inside the solder bump, an infrared (IR) microscope was adopted at various stressing conditions. Hot spots were clearly observed at a high stressing current as shown in Figure 4-9(a) and 4-9(b). The hot spot temperature was 122.3°C, which locates near the current entrance point near the upper right-hand side at the chip side in CuNi UBM system, while it was 129°C in Cu UBM case at the same location. Indeed thicker UBM helps to disperse heat and redistributed current route, therefore the hot spot temperature is

higher in single Cu UBM system. The average temperature of Cu system was measured 117°C, and that of CuNi system was only 113°C. In other words, the hot spot temperature were higher than the average temperature about 10°C. Since hot spot temperature and the average temperature inside solder joint are both higher in Cu UBM system, the diffusion near the hot spot regions is much faster and the dissolution rate is higher as well. The solubility of Cu in SnAg solder is much larger than the solubility of Ni in SnAg solder. As the result, the bilayer structure of CuNi UBM successfully reduced the heat distribution in solder joint and resulted in a lower hot spot temperature, thus we can obtain a longer life time for CuNi UBM system.

4.3.3 Simulation Results

The three-dimensional (3D) thermoelectrical coupled simulation was carried out by the FEA to investigate the current distribution in our test samples [23]. The model used was a SOLID69 eight-node hexahedral coupled field element with ANSYS software. The electrical and thermal resistivity of the materials and the boundary conditions used in this modeling were chosen from our previous study.¹⁷ The resistivity of SnAg is 12.3 $\mu\Omega\cdot\text{cm}$ as well. The current crowding behavior inside solder bump, near the entrance of the Al trace, are demonstrated in Figure 4-10(a) and 4-10(b) for Cu/Ni and Cu system under 7.9×10^4 A/cm² respectively. According to simulation results shown in Figure 6 under the same condition, the maximum current density in Cu UBM system was 3.2×10^4 A/cm², which resulted in 4.0 of current crowding ratio [24]; However, that reached only 2.0×10^4 A/cm², which the current crowding ratio was 2.5 in CuNi UBM system. Compared with Cu UBM system, the addition of high resistivity Ni layer, 6.8 $\mu\Omega\cdot\text{cm}$, successfully re-dispersed the current route. The resistivity of Ni₃Sn₄ is 28.5 $\mu\Omega\cdot\text{cm}$, higher than 17.5 $\mu\Omega\cdot\text{cm}$ of Cu₆Sn₅,

helped re-distributed the current as well. In the Cu UBM system, the high maximum current density caused the severe current crowding effect. Since the EM driving force is proportional to the current density, the failure will be accelerated by the effect of current crowding. In the bilayer system, after the current went into solder from chip side, current would first spread out inside UBM, thus if UBM has large resistivity, it can rearrange the current distribution and lower down the current crowding ratio. Compared with the single layer Cu UBM system, the critical Ni layer addition provides the better current distribution. As the result, the current crowding effect is reduced to minimum and the device life time, controlled by the EM process, improve dramatically. In our study, even lower current density was used in Cu UBM system, but still we obtained shorter failure time. In short, CuNi UBM system has better EM life time compared with Cu UBM system.

4.3.4 Electromigration Activation Energy Measurement

For the Cu UBM system, using the same stressing conditions is not suitable for a statistical failure time due to the possible melting issue. For example, under 165 °C and 7.9×10^4 A/cm² current density testing condition, the average failure time of the Cu UBM system is only 15 hrs while it reached near 100 hrs in Cu/Ni UBM system at the same condition. Therefore, the current density was purposely reduced to 7.0×10^3 A/cm² to have more comparable failure time. By utilizing the more accurate time duration, we can estimate not only the EM activation energy but also the failure mechanism as well. Tables 4-2 and 4-3 show the EM lifetime statistics of SnAg/CuNi and SnAg/Cu solder joints, with calibrated bump temperature by using Kelvin probes under 7.9×10^3 and 7.0×10^3 A/cm² current stressing.

According to Choi *et. al.* the MTTF equation can be expressed as [8]

$$\text{MTTF} = A \frac{1}{(cj)^n} \exp \left[\frac{Q}{k(T+\Delta T)} \right] \quad (4-1)$$

where A : constant that contains a factor involving the cross-sectional area of the joints, j : current density in ampere per centimeter square, n : model parameter for current density, Q : activation energy, k : Boltzmann's constant, T is the local factual bump temperature or Al trace temperature; MTTF is the current stressing time till failure and Q is the activation energy for electromigration. Since the Al trace is the main heat source, the entrance point with a large current crowding effect would be accompanied by the increase in Joule heating. In our study, the temperature term is calibrated by using Al trace temperature, which is more accurate than the hot plate temperature. Taking the natural log of the electromigration life time versus with $10^{-3}/k$, then we can obtain the electromigration activation energy before and after calibration

4.4 Summary

In summary, we have demonstrated a method to enhance the electromigration lifetime of SnAg flip chip solder joints by adopting Cu/ Ni bilayer UBM structure. The particular significance of adding the thin Ni layer is to reduce and limit the current crowding effect. The better current redistribution and limited current crowding effect provide the main contributions of the time to failure improvement in the bilayer system. As long as the current crowding can be rearranged from solders to UBM layer, which has higher resistance to electromigration, we can have a more reliable solder joint. The IR and simulation results also agreed with our experiments. The current crowding effect can be reduced and the hot spot temperature was decreased as well.

4.5 References

- 1 K. N. Tu, *Solder Joint Technology* _Springer, New York, 2007, pp. 245–287.
- 2 I. A. Blech, *Appl. Phys. Lett.* **29**, 131 (1976).
- 3 H. B. Huntington and A. R. Grone, *J. Phys. Chem. Solids* **20**, 76 (1961).
- 4 K. Zeng and K. N. Tu, *Mater. Sci. Eng., R.* **38**, 55 (2002).
- 5 L. H. Xu, J. H. L. Pang, and K. N. Tu, *Appl. Phys. Lett.* **89**, 221909 (2006).
- 6 L. Zhang, S. Q. Ou, J. Huang, K. N. Tu, S. Gee, and L. Nguyen, *Appl. Phys. Lett.* **88**, 012106 (2006).
- 7 K. N. Tu, *J. Appl. Phys.* **94**, 5451 (2003).
- 8 W. J. Choi, E. C. C. Yeh, and K. N. Tu, *J. Appl. Phys.* **94**, 5665 (2003).
- 9 J. W. Nah, K. W. Paik, J. O. Suh, and K. N. Tu, *J. Appl. Phys.* **94**, 7560 (2003).
- 10 T. L. Shao, Y. H. Chen, S. H. Chiu, and C. Chen, *J. Appl. Phys.* **96**, 4518 (2004).
- 11 Y. H. Lin, Y. C. Hu, C. M. Tsai, C. R. Kao, and K. N. Tu, *Acta Mater.* **53**, 2029 (2005).
- 12 Y. L. Lin, C. W. Chang, C. M. Tsai, C. W. Lee, and C. R. Kao, *J. Electron. Mater.* **35**, 1010 (2006).
- 13 L. H. Xu, J. K. Han, J. J. Liang and K. N. Tu, *Appl. Phys. Lett.* **92**, 262104 (2008).
- 14 J. W. Nah, J. O. Suh, K. N. Tu, S. W. Yoon, V. S. Rao, V. Kripesh, and F. Hua, *J. Appl. Phys.* **100**, 123513 (2006).
- 15 S. W. Liang, Y. W. Chang and C. Chen, *J. Electron. Mater.* **36** (10), 1348 (2006).
- 16 Y. H. Lin, Y. S. Lai, Y. W. Lin and C. R. Kao, *J. Electron. Mater.* 37(1), 96 (2008)
- 17 Y. W. Chang, S. W. Liang and C. Chen, *Appl. Phys. Lett.* **89**, 032103 (2006).
- 18 E. C. C. Yeh, W. J. Choi, K. N. Tu, P. Elenius, and H. Balkan, *Appl. Phys. Lett.* **80**, 580 (2002).
- 19 L. Zhang, S. Ou, J. Huang, K. N. Tu, S. Gee and L. Nguyen, *Appl. Phys. Lett.* **88**,

012106 (2006).

20. B. F. Dvson, T. R. Anthony and D. Turnbull, *J. Appl. Phys.* **38**, 3408 (1967).

21. K. Zeng and K. N. Tu, *Materials Science and Engineering Reports*, **R38**, 55 (2002).

22. S. H. Chiu, T. L. Shao and C. Chen, *Appl. Phys. Lett.* **88**, 022110 (2006).

23. S. W. Liang, Y. W. Chang, T. L. Shao, Chih Chen and K. N. Tu, *Appl. Phys. Lett.* **89**, 022117 (2006).

24. S. W. Liang, S. H. Chiu, T. L. Shao and C. Chen, *J. Electron. Mater.* **21**(1), 137 (2008)

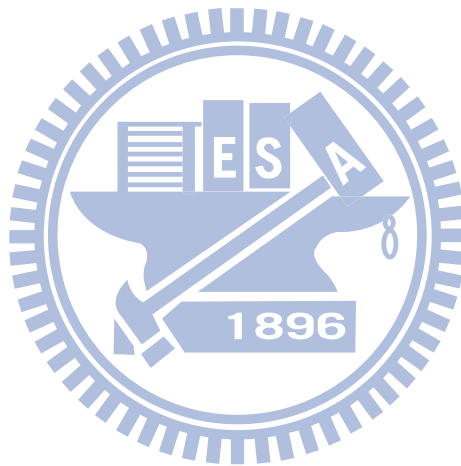


Table 4-1 Material Properties used in our simulation.

Materials	Resistance ($m\Omega \cdot cm$)
Al	3.2
Cu	1.7
Ni	6.8
SnAg3.5	12.3
Electoless Ni	70
Cu_6Sn_5	17.5
Ni_3Sn_4	28.5

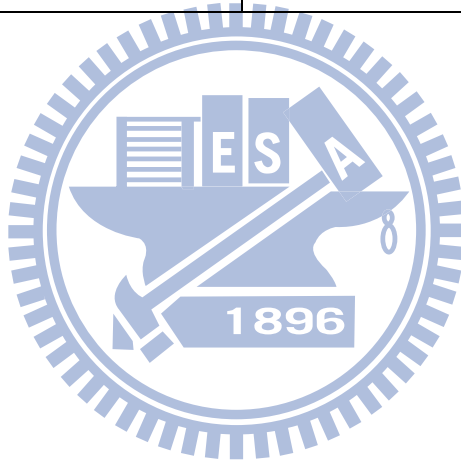


Table 4-2 Electromigration lifetime statistics of SnAg/CuNi solder joints with reanalyzed bump temperature by using Kelvin probes under $7.9 \times 10^3 \text{ A/cm}^2$ current stressing.

SnAg	Hot plate temperature (°C)	Calibrated temperature (°C)	Temperature increase (°C)	Average failure time (hr)
	135	156	21	431
	150	170	20	173
	165	184	19	105

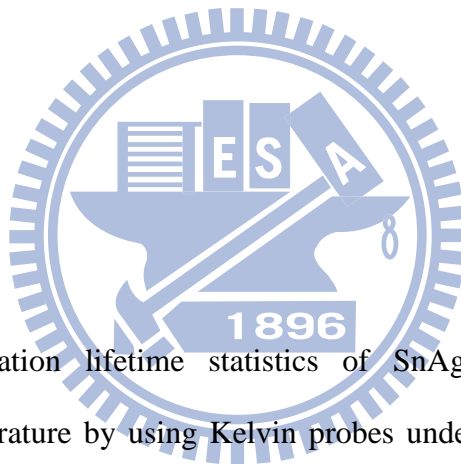


Table 4-3 Electromigration lifetime statistics of SnAg/Cu solder joints with reanalyzed bump temperature by using Kelvin probes under $7.0 \times 10^3 \text{ A/cm}^2$ current stressing.

SnAg	Hot plate temperature (°C)	Calibrated temperature (°C)	Temperature increase (°C)	Average failure time (hr)
	135	157	22	358
	150	174	24	180
	165	186	21	56

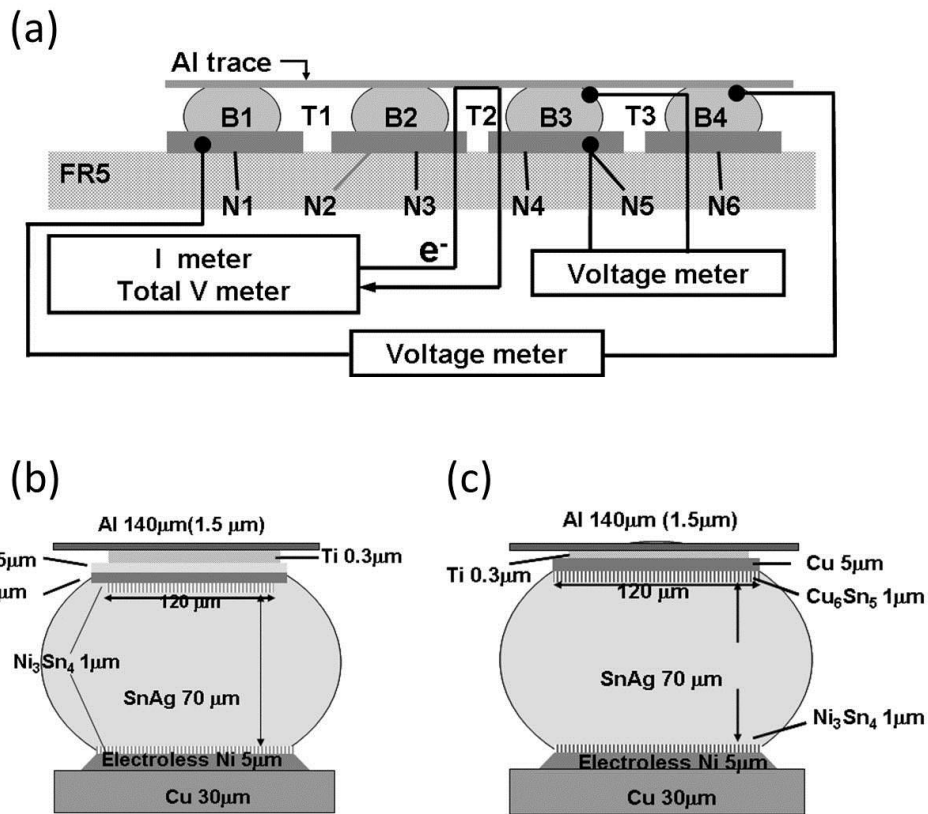


Figure 4-1 Cross-sectional schematic of the layout design. The Al trace connected all the four solder bumps together. (a) electromigration setup, (b) SnAg solder with CuNi UBM, and (c) SnAg solder with Cu UBM.

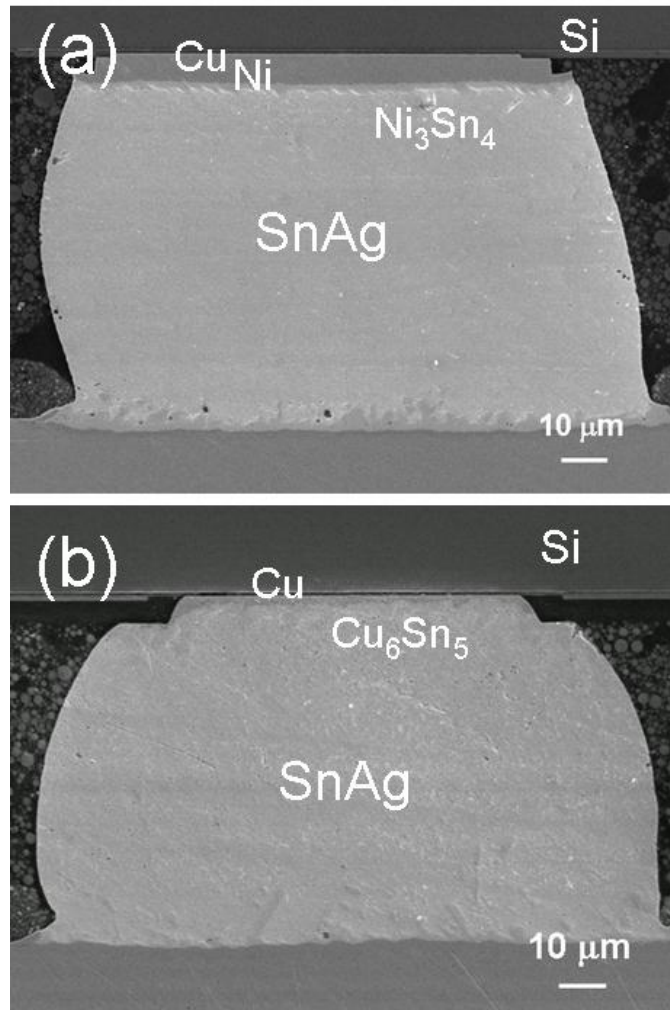


Figure 4-2 The corresponding cross-sectional SEM images for solder bump before current stressing. (a) SnAg solder with CuNi UBM (b) SnAg solder with Cu UBM.

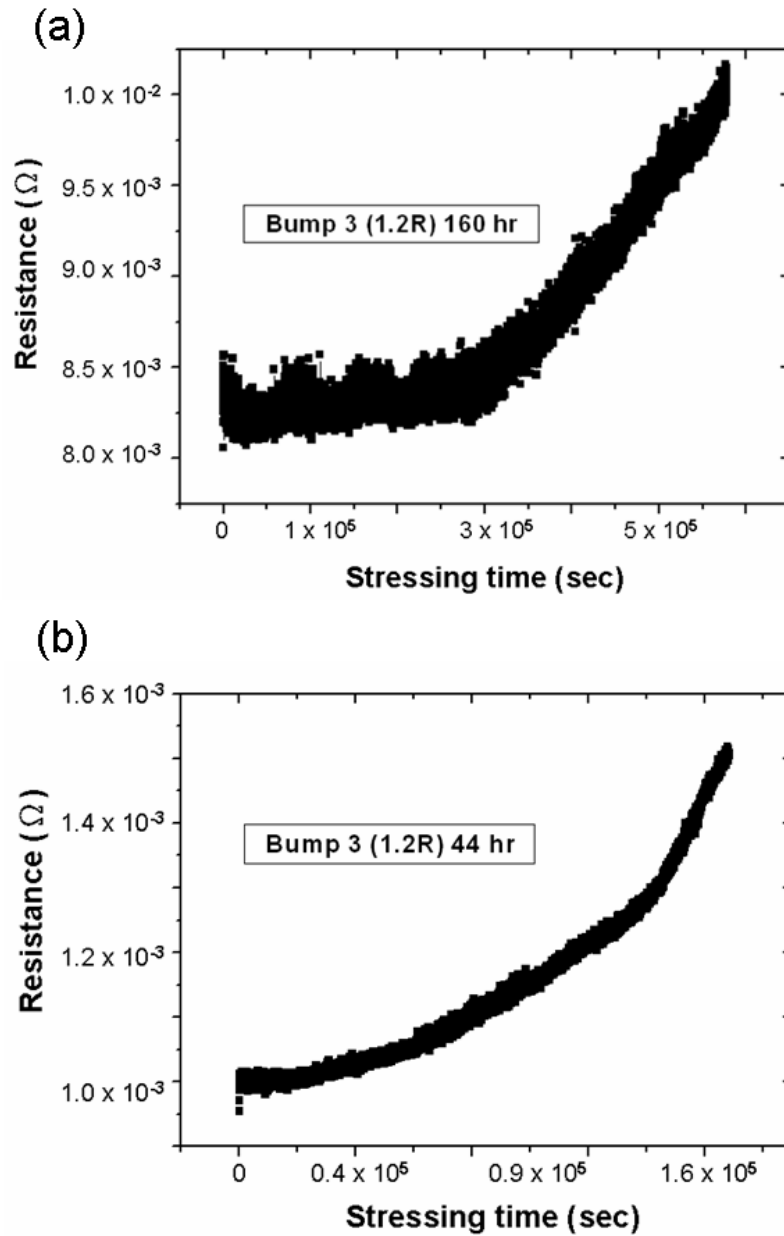


Figure 4- 3 The corresponding Bump resistance for the stressing circuit as a function of stressing time up to failure which represented as the resistance of Bump 3 increased 20 % when powered by 0.9 A (7.9×10^4 A/cm²) at 150 °C. (a) Cu/Ni UBM system, (b) Cu UBM system.

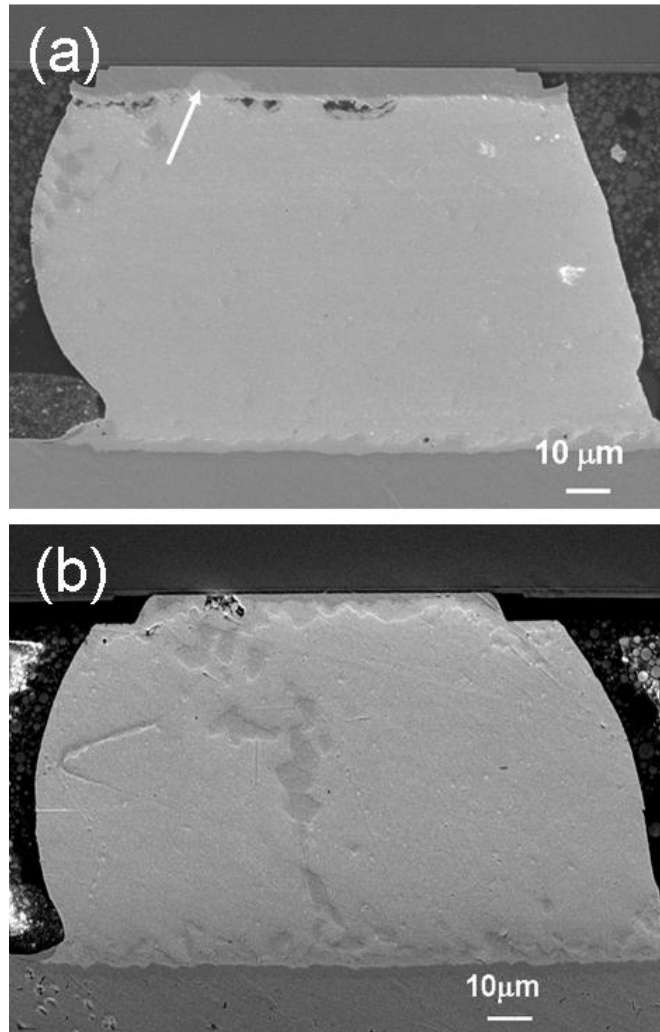


Figure 4-4 The corresponding cross-sectional SEM image for solder bump. (a) SnAg/CuNi after being stressed by 7.9×10^4 A/cm² at 150 °C current stressing for 160 hrs till the resistance of Bump 3 increasing 20%. (b) SnAg/Cu after being stressed by 7.9×10^4 A/cm² at 150 °C current stressing for 44 hrs till the resistance of Bump 3 increasing 20%.

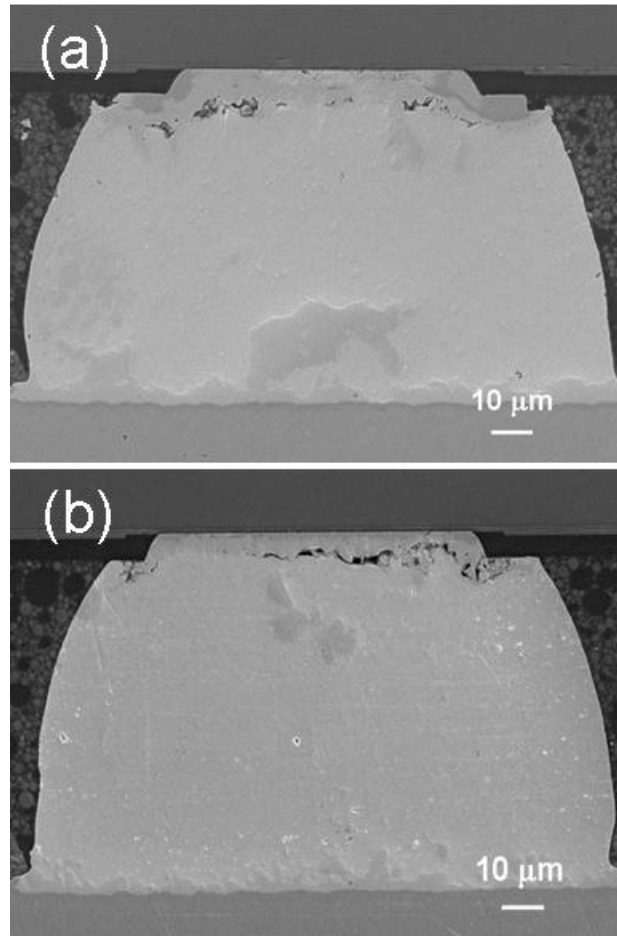


Figure 4-5 The corresponding cross-sectional SEM image for solder bump. (a) SnAg/CuNi after being stressed by 7.9×10^4 A/cm² at 150 °C current stressing for 160 hrs till the resistance of Bump 3 increasing 20%. (b) SnAg/Cu after being stressed by 7.9×10^4 A/cm² at 150 °C current stressing for 44 hrs till the resistance of Bump 3 increasing 20%.

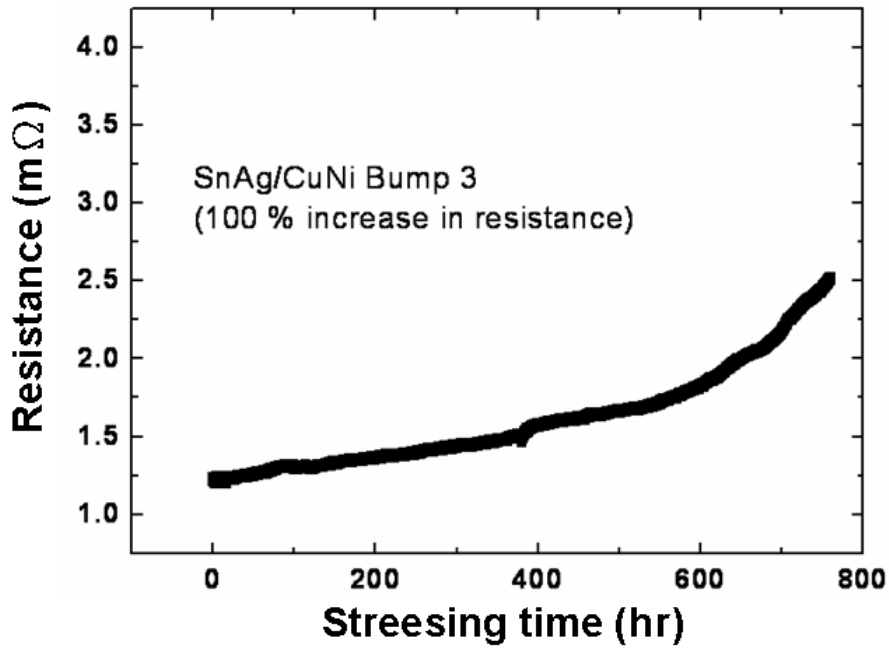


Figure 4-6 The corresponding Bump resistance for the stressing circuit as a function of stressing time up to failure which represented as the resistance of Bump 3 increased 100 % when powered by 0.9 A (7.9×10^4 A/cm²) at 150 °C in Cu/Ni UBM system.

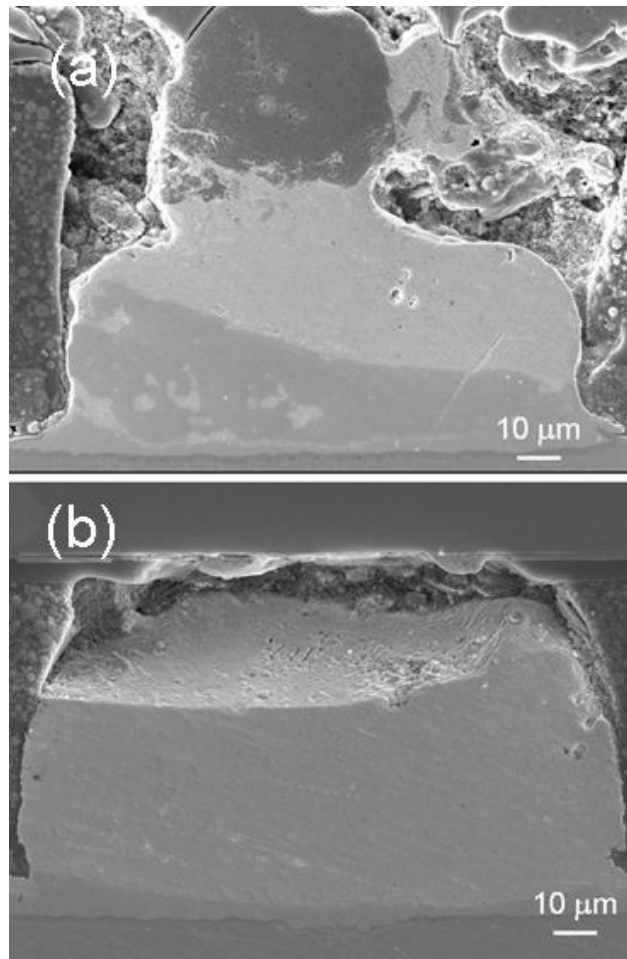


Figure 4-7 The corresponding cross-sectional SEM image for solder bump. (a) SnAg/CuNi after being stressed by 7.9×10^4 A/cm² at 150 °C current stressing till Bump 3 totally failed. (b) SnAg/Cu after being stressed by 7.9×10^4 A/cm² at 150 °C current stressing till the Bump 3 totally failed.

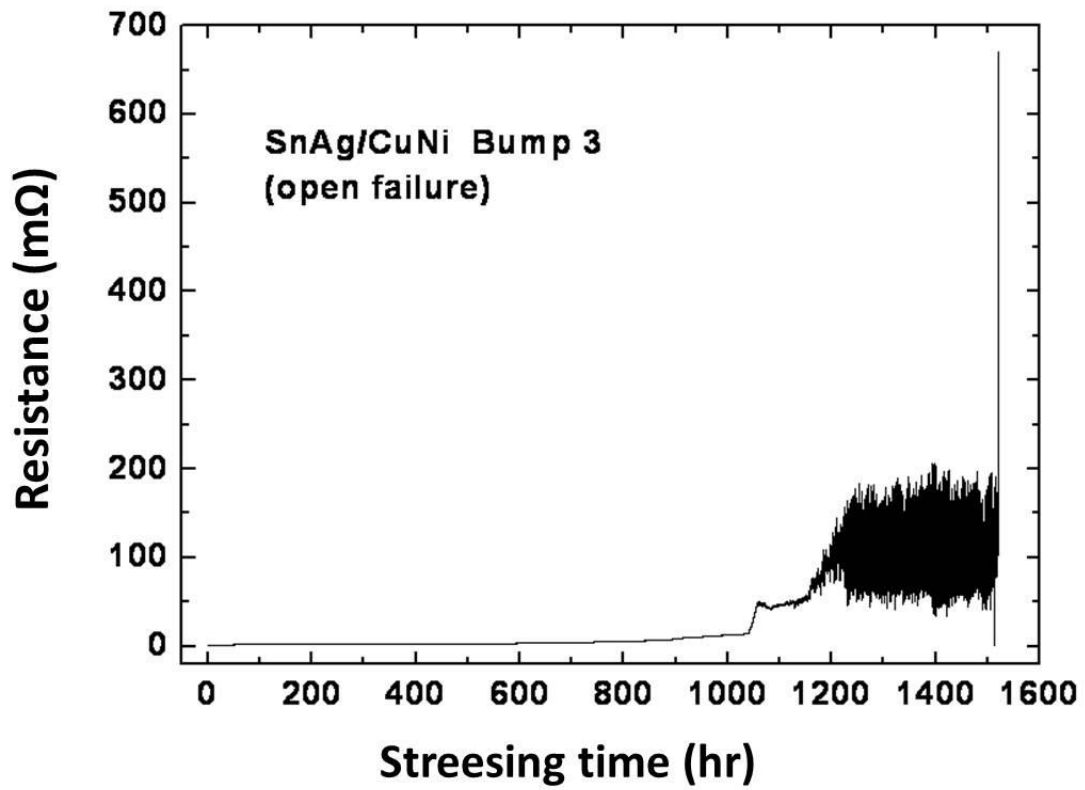


Figure 4-8 The corresponding Bump resistance for the stressing circuit as a function of stressing time up to totally failure of Bump 3 when powered by 0.9 A (7.9×10^4 A/cm²) at 150 °C in Cu/Ni UBM system.

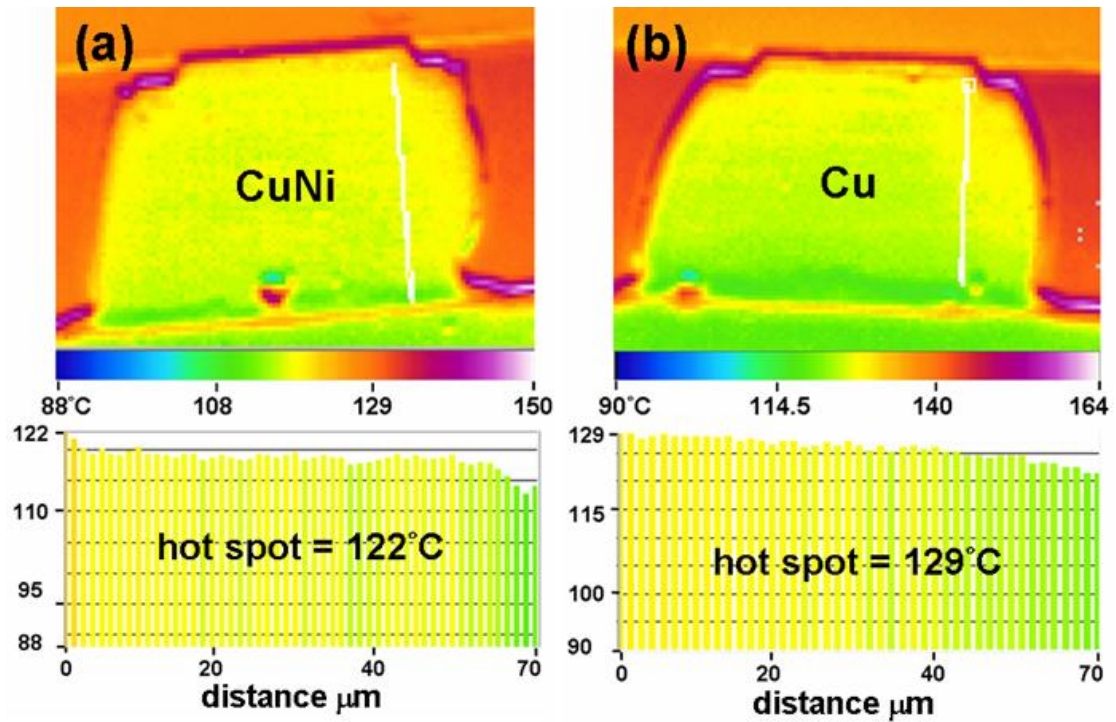
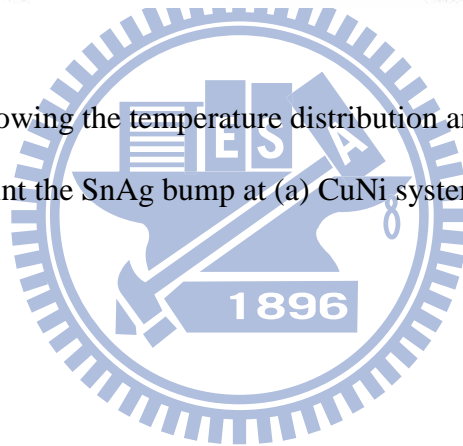


Figure 4-9 IR images showing the temperature distribution and the hot spot point near the entrance point the SnAg bump at (a) CuNi system; (b) Cu system.



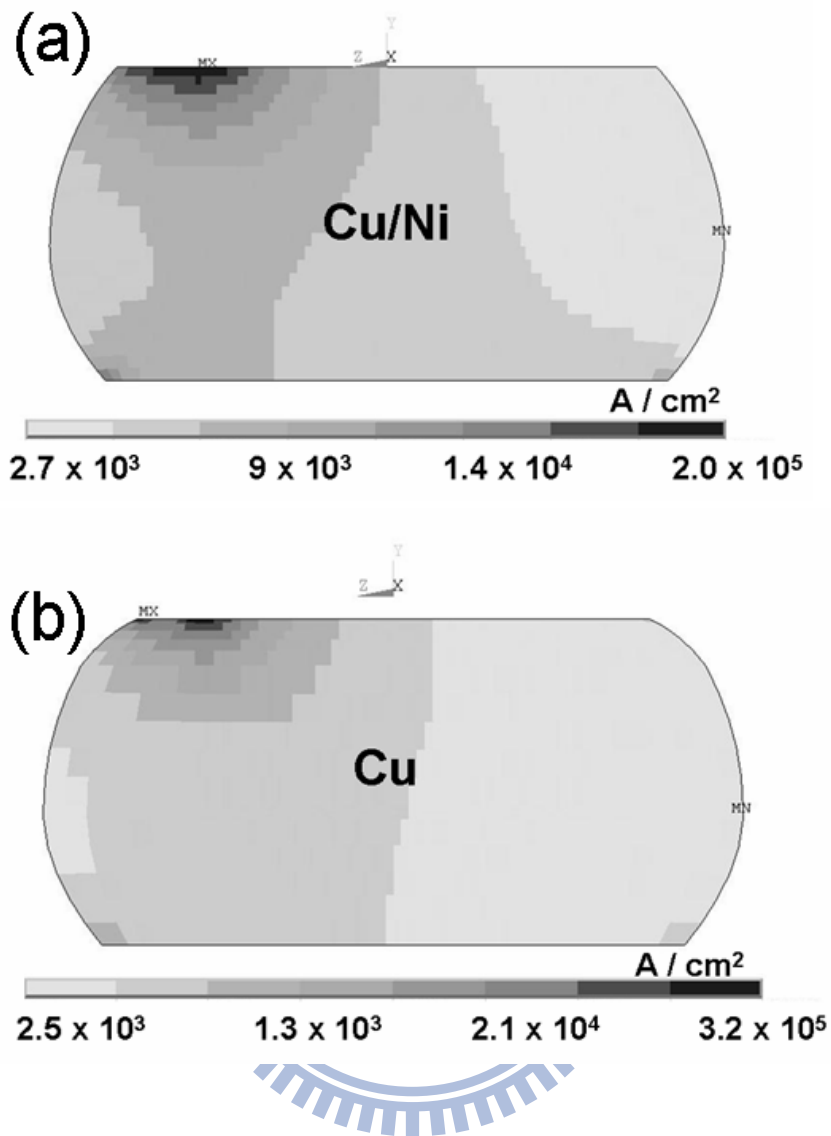


Figure 4-10 (a) Cross-sectional view of current density distribution in solder joint for CuNi UBM system; (b) corresponding cross-sectional view for current density distribution for Cu UBM system.

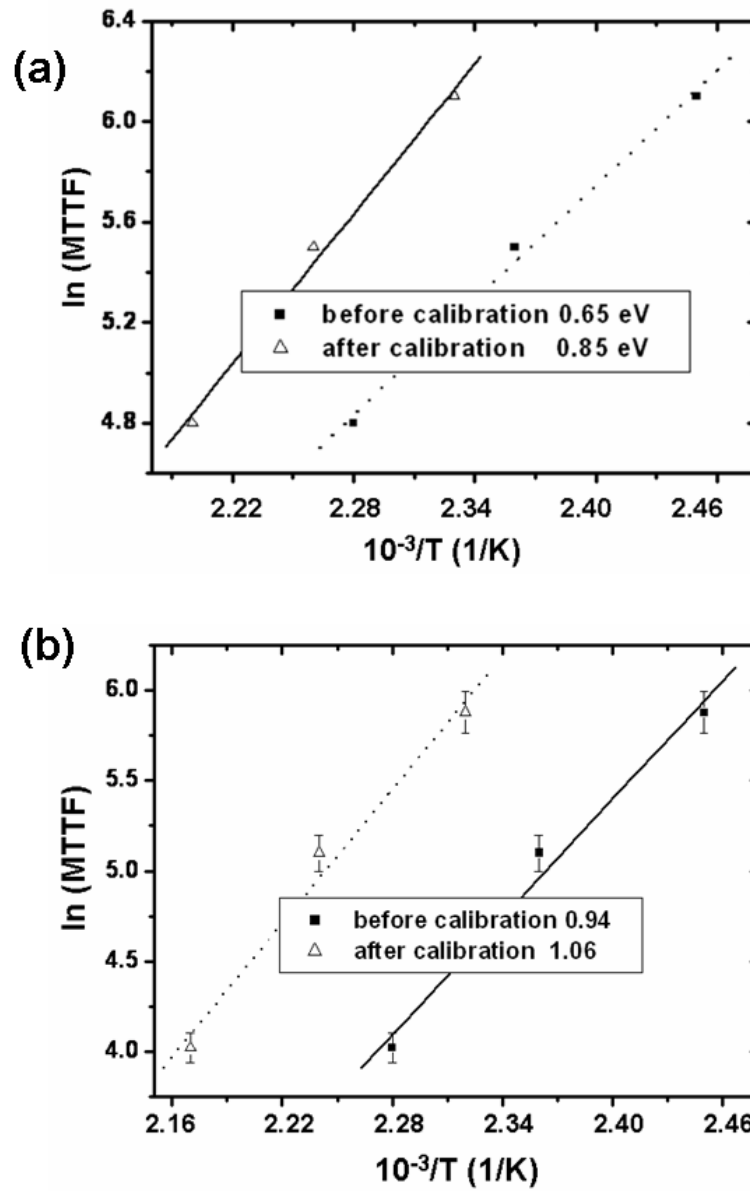


Figure 4-11 Plots of MTTF against $\frac{10^{-3}}{k}$, (a) eutectic SnAg solder joints with Cu/Ni UBM, and (b) eutectic SnAg solder joints with Cu UBM.

Chapter 5 Failure Induced by Thermomigration of Cu-Sn and Ni-Sn Intermetallic Compounds during Electromigration in Pb-free SnAg Solder Joints

5.1 Introduction

Electromigration (EM) in flip-chip solder joints has become inevitable in recent years because of the miniaturization trend to meet the demand for higher performance in portable electronics [1]. Many efforts have been made to investigate this emerging issue [2-10]. The crowing effect in the chip end plays a crucial role in the failure mechanism during EM [5,11], causing void formation in solder joints with thin-film UBMs or dissolution of UBMs in solder joints with thick-film UBMs at high current-density regions [10,12,13].

Moreover, it is interesting that thermomigration (TM) also occurs during the accelerated electromigration test for flip-chip Pb-containing solder joints [6,7,14,16]. Typically, the applied current ranges from 0.5 A to 2.0 A and thus serious Joule heating takes place during the EM test. The resistance of the wiring trace on the Si side is much longer than that on the substrate side. Non-symmetrical Joule heating builds up a temperature gradient across the solder joints. For Pb-containing solder, Pb atoms move to the cold end on the substrate side. On the other hand, Sn atoms migrate to the hot end on the Si side. At tested temperatures higher than 100 °C, Pb atoms appear to be the dominant diffusion species, causing void formation on the chip end. Due to environmental concerns, the microelectronic industry replaces the eutectic SnPb solder with Pb-free solders. However, only few studies address the TM issue in Pb-free solders [16,17]. In particular, the TM of Cu and Ni UBMs are not clear.

In this chapter, we examine the TM and EM behaviors in eutectic SnAg solder joints with Cu and Ni UBMs. It is found that TM of Cu dominates the failure mechanism at high stressing currents, instead of EM damage of solder alloys. Copper atoms, or Cu_6Sn_5 intermetallic compounds (IMCs), migrate to the cold end and serve as the dominant diffusion species during EM, and voids form in the original location of Cu UBM. On the other hand, the TM of Ni appears much slower than that of Cu. Theoretical calculations were carried out and also agreed with the observed phenomena.

5.2 Experimental Procedures

The dimensions of the flip-chip joints used in this study are shown schematically in Figure 5-1(a) and 5-1(b). The bump has a dimension of 130 μm in width and 75 to 80 μm in height with a UBM opening of 100 and 110 μm in diameter for Cu UBM and Cu/Ni UBM, respectively. A 0.3- μm Ti layer was sputtered as an adhesion/diffusion barrier layer between the UBM and the Al trace. The solder joints consist of eutectic SnAg solder bumps with electroplated 5- μm Cu UBMs or with electroplated 5- μm Cu/electroplated 3- μm Ni UBMs, as shown in Figure 5-1(a) and 5-1(b), respectively. The EM test layout consisted of four bumps. An Al trace of 2550 μm long, 100 μm wide, and 1.5 μm thick connected the four bumps together. The four bumps were denoted as “Bump 1” through “Bump 4,” as shown in Figure 5-1(c). Six Cu nodes were fabricated on a FR5 substrate, and they are labeled as Nodes “N1” through “N6.” The dimension of the Cu lines on the substrates was 30 μm thick and 100 μm wide.

To facilitate the observation of EM and TM behaviors, the joints were polished laterally to approximate their centers. After polishing, the widths of the Al traces and

the Cu lines also decreased accordingly. Desired electric currents were applied through Nodes N3 and N4. Therefore, Bumps 1 and 4 did not yet carry current. However, they have almost the same Joule heating as Bumps 2 and 3 because the Al trace and the Si die possess excellent ability for heat conduction. The applied current was 0.55 A at 150°C on a hot plate, which corresponds to an average current density of $9.7 \times 10^3 \text{ A/cm}^2$ in the UBM opening. The temperature distribution in the solder bumps during the current stressing was measured by a QFI infrared (IR) microscope, which has a temperature resolution of 0.1°C and a spatial resolution of 2 μm. The IR measurement was performed before the EM test. During the temperature measurement, the flip-chip package was stressed by 0.55 A on a hot stage maintained at 100°C, and the polished bump surface faced the IR microscope. The temperature measurement was then performed to record the temperature distribution (map) after reaching a steady state. Because the hot stage for the IR microscope can be heated only up to 110°C, the temperature measurement performed at 100°C. Kelvin probes were employed to monitor the resistance changes for both Bumps 2 and 3 [18]. Thus, the EM damage can be monitored *in-situ*, and the current can be terminated as soon as the resistance increases to the desired value. The changes in surface microstructure were examined by using a SEM, using either secondary image mode or BEI mode. Next, to identify the Cu TM phenomenon, focused ion beam (FIB) was employed to etch a surface at the interface between the Si side and the solder to analyze the interfacial damage caused by TM.

5.3 Results and Discussion

5.3.1 Microstructure Change due to Thermomigration

(i) SnAg with Cu UBM

Before current stressing, the IMCs on the chip side attach to UBMs very well. Figures 5-2(a) and 5-2(b) show the cross-sectional SEM images for the microstructures of the SnAg/Cu and SnAg/CuNi bumps, respectively, before current stressing. Interfacial IMCs are labeled by the arrows in the figures. Cu-Sn IMCs form in the SnAg solder bump with a Cu UBM on the chip side, and there are about 3.18 μm Cu UBMs left for the as-fabricated bumps. On the other hand, Ni_3Sn_4 IMCs form in the solder/chip interface in the SnAg solder bump with a Ni UBM. The EM damage generally occurs on the chip side due to the current crowding effect [9,11]. Although there were no currents passing through Bumps 1 and 4, the temperature measurement by the IR microscope indicates that they have almost the same Joule heating effect as Bumps 2 and 3. Therefore, they are quite suitable to serve as control samples to inspect TM simultaneously during the accelerated EM test.

We found that voids formed in the chip end for all the four bumps after the current was applied through Bumps 2 and 3 for 76 hrs, as shown in Figures 5-3(a) through 5-3(d). The current was terminated when the resistance of Bump 3 reached 4.0 times its original value. Voids formed in the cathode/chip end for Bump 3 because both EM and TM forces move the Cu atoms to the substrate side in this bump, as depicted in Figure 5-3(c). Therefore, the largest voids formed in Bump 3. Nevertheless, it was observed that severe damage also occurred in the anode/chip end of Bump 2 with the formation of large voids. Its resistance also increased to 2.0 times its original value. It is reported that Sn atoms migrate to the hot end, which is the chip side in this test structure [7]. The voids accumulate in the interface of the solder and the Si chip. For the Pb-free solder in this study, it is also expected that Sn atoms would migrate to the hot end on the Si side because Sn has a positive heat transport number [17,19]. In addition, the EM force also pushes the Sn atoms to the anode on the Si side. Thus, the voids in the chip side for Bump 2 are not accredited to EM or

the TM of the solder.

Instead, it is proposed that TM of Cu_6Sn_5 IMCs dominates the failure mechanism in this stressing condition. The SEM images for Bumps 1 and 4 also support this assumption, as illustrated in Figures 5-3(a) and 5-3(d). Only TM takes place in these two bumps because there was no current passing through these two bumps. Yet, the thermal gradients were slightly smaller than those in Bumps 2 and 3. Thus, less damage and smaller voids occurred in these bumps. Furthermore, it has been found that the voids replaced the positions of Cu_6Sn_5 IMCs and of the Cu UBM. Therefore, Cu or Cu_6Sn_5 migrated to the substrate side under the huge thermal gradients in the four bumps.

Another evidence that lends support to Cu diffusion can be illustrated in Figures 5-4(a) and 5-4 (b). Figure 5-4(a) represents the cross-sectional view of Bump 1 before current stressing, and Figure 5-4(b) was the view after 60 hr-stressing when the resistance of Bump 3 reached to 2.3 times of its original value. While Bump 1 was un-powered, the damage is clear near the upper left-hand corner. In addition, from the BEI image shown in Figure 5-4(b), the IMC has formed toward the substrate side and the Cu UBM has dissolved almost completely into solder. This can be accredited to the thermomigration of Cu atoms by fast interstitial diffusion and reaction with Sn atoms to form IMC inside the solder bump.

The results are quite reproducible, and other results also support that the Cu-Sn IMC TM dominates the failure mechanism in this stressing condition. The BEI images in Figure 5-5 show the microstructures of the four solder bumps after stressing at 0.55 A at 150°C for 82 h. Severe damages occur in Bump 3, as illustrated in Figure 5-5(c). Although there are no obvious voids formed in the rest of the three bumps, spalling of the Cu-Sn IMCs are clearly observed. In Bump 1 in Figure 5-5(a) where no currents passed through, the Cu UBMs were consumed completely, and the IMCs

detached from the original interface in the chip side. They seem to be in the process of migrating to the substrate side under a huge thermal gradient. For Bump 4 in Figure 5-5(d), Cu-Sn IMCs in the chip side also started to migrate to the substrate end due to TM. In Bump 2, although the EM force pushes the Cu atoms upward to the chip end, spalling of Cu-Sn IMCs still took place at the right-hand side of the upper interface. This finding also implies that the TM force is greater than the EM force acting on the Cu atoms.

To further examine whether there are voids in the interface of the solder and the Si chip for the samples in Figure 5-5, FIB was employed to examine the interface. Figure 5-6(a) depicts SEM images for the interface of the bump in Figure 5-5(a), in which the Cu-Sn IMCs started to move to the substrate by TM. The etched position is illustrated by the dotted line in Figure 5-5(a). It is found that numerous tiny voids formed at the interface. An FIB ion image was adopted to examine the interface, so that the solder and the IMCs could be distinguished, as shown in Figure 5-6(b). It was observed that the voids locate in between the SiO₂ and the Cu-Sn IMCs. Some of them occurred in the Al trace. It is speculated that the IMCs are in the process of migrating thermally toward the substrate (cold) side; thus, voids start to nucleate in the interface. The interface microstructure in Bump 4 in Figure 5-5(d) was also inspected by FIB, and the etching location is labeled by the dotted line in Figure 5-5(d). The SEM image in Figure 5-6(c) also reveals the void formation at the interface. Its ion image is shown in Figure 5-6(d). Some of the IMCs in the interface spalled into solder, causing void formation at the original location of the IMCs. The FIB results from both bumps indicated that TM of Cu took place and voids started to nucleate at the original location of the Cu UBMs.

In addition to EM and TM forces, chemical potential may also play a role in Cu migration. The Cu on the chip end may migrate to the substrate end to form ternary

Cu-Ni-Sn IMCs, which have a lower free energy [20]. To examine whether chemical potential is able to influence the Cu diffusion in the present case, another set of solder joints was annealed at 165 °C on a hot plate for 90 hrs. This process takes Joule heating into consideration, and the annealing time is longer than the stressing time for the samples with a Cu UBM. Only chemical potential force exists during the annealing. It is found that the Cu₆Sn₅ IMCs grew thicker from 1.72 to 4.31 μm, but they did not detach nor migrate to the substrate side, as shown in Figure 5-7. These results suggest that the force of chemical potential is negligible compared with forces of EM and TM in the present case.

It is noteworthy that TM of Sn also takes place in all the four bumps. Hsiao *et al.* reported that the Sn atoms migrate toward the hot end in the SnAg solder joints under a large thermal gradient. The heat of transport is measured to be 1.36 kJ/mol for Sn. In the present study, the Cu atoms diffuse to the cold end in solder joints, which is inconsistent with the results for TM on pure Cu [21]. The results in Bumps 1 and 4 indicate that the voids appear in the chip side, which is the hot end. This finding implies that the TM flux for Cu overwhelms that of Sn.

It is speculated that the high Cu solubility in Pb-free solder facilitates the occurrence of the serious TM of Cu-Sn IMCs. Zeng and Tu reported that the solubility of Cu is 0.18 wt% in eutectic SnPb solder at 220 °C. However, it increases to 1.54 wt% in Pb-free solders at 260°C [22]. Therefore, it is difficult to observe Cu TM in the SnPb solder during the EM test of solder joints. EM or TM of Sn and Pb prevails in the SnPb solder joints. Yet, for Pb-free solders, TM of Cu becomes obvious because of the high solubility of Cu. In some stressing conditions, the TM flux of Cu may be greater than the EM or TM flux of Sn. Therefore, we can observe the unique failure mode in Figures 6-3 and 6-5.

(ii) SnAg with CuNi UBM

It is of interest that whether TM of Ni would happen in a Pb-free solder joint because Ni is another important UBM material in the microelectronics packaging industry. It is reported that Ni atoms also migrate toward to the cold end [23]. Similar EM tests were performed in eutectic SnAg solder joints with an additional 3- μm Ni UBM on the 5- μm Cu UBM. The dimensions of the joints are similar to the ones with 5- μm Cu UBMs. After current stressing at 0.55 A at 150°C for 180 hrs, the microstructures for the four bumps were observed and shown in Figures 5-8(a) to 5-8(d). Voids formed only in Bump 3, which had a downward electron flow. These voids are caused by EM and they formed in the interface of the solder and the Ni₃Sn₄ IMCs. The resistance of this bump increased to 1.5 times of its initial value. It is interesting that there were no damages or voids observed in Bumps 1, 2, and 4, except that the thickness of Ni-Sn IMCs increased from 0.9 μm to 1.7 μm . Thus, no TM of Cu and Ni was found in the joints with Ni UBMs. The results also suggested that the Ni UBMs serve as an excellent diffusion barrier for Cu TM.

5.3.2 Temperature Distribution Measurement

(i) SnAg with Cu UBM

Figures 5-9(a), 5-9(b), 5-9(e), and 5-9(f) show the temperature distributions for the four bumps with Cu UBMs stressed at 0.55 A through Nodes 3 and 4 at 100°C. The average temperature was 116.0°C for Bump 1, 118.5°C for Bump 2, 118.0°C for Bump 3, and 115.8°C for Bump 4. The mean value was obtained by averaging the temperatures in an area of 50 \times 50 μm^2 around the center of the bump. Figures 5-9(c), 5-9(d), 5-9(g), and 5-9(h) present the temperature profile along the white line in Figure 5-9(a), 5-9(b), 5-9(e), and 5-9(f), respectively. Since the Al trace serves as the major heating source [8,9], the temperature in the solder close to the chip end was

higher than those close to the substrate end. Therefore, a huge thermal gradient was built up across the solder bump during the stressing by high current density. The thermal gradient is defined here as the temperature difference between the two ends of the white line divided by the length of the line, which was 70 μm . The measured thermal gradient reached 1143 $^{\circ}\text{C}/\text{cm}$ Bump 1, 1643 $^{\circ}\text{C}/\text{cm}$ for Bump 2, 1857 $^{\circ}\text{C}/\text{cm}$ for Bump 3, and 1143 $^{\circ}\text{C}/\text{cm}$ for Bump 4.

(ii) SnAg with CuNi UBM

We also have thermal gradient of CuNi UBM system as shown in Figures 5-10(a) to 5-10(d) which present the temperature distributions in Bumps 1 to 4, respectively. When they were stressed by 0.55 A at 100 $^{\circ}\text{C}$, the measured thermal gradient was 857, 1286, 1429 and 857 $^{\circ}\text{C}/\text{cm}$. The thermal gradients are slightly smaller than those in the bumps with a 5- μm Cu UBM. This phenomenon may be attributed to the 3- μm Ni relieving the local current crowding effect in solder [24].

5.3.3 Theoretical Calculation

(i) SnAg with Cu UBM

The EM force also pushes the Cu and Sn atoms to the chip end for Bump 2. Hillocks might be formed in the chip end if only EM force is considered. However, voids formed in the anode/chip end, instead of hillocks, as shown in Figure 5-5(b). Therefore, it is inferred that the TM force overwhelms the EM force in the present stressing condition. To verify this point, theoretical calculations are performed. The EM force is represented as [25]:

$$F = Z^* eE = Z^* \rho j \quad (5-1)$$

where Z^* is the effective charge number of ions, ρ is the resistivity, j is the electric current density, e is the charge of an electron, and E is the electrical field. We assume

that Cu atoms are the diffusion species for the migration of the Cu-Sn IMCs. The effective charge number is taken as 6.4 for Cu [26], resistivity as $1.67 \times 10^{-8} \Omega\cdot\text{m}$, and the current density as $9.7 \times 10^7 \text{ A/m}^2$. Thus, the EM force is $1.66 \times 10^{-18} \text{ N}$. The work done by the force in an atomic jump distance of $3 \times 10^{-10} \text{ m}$ is $4.98 \times 10^{-28} \text{ J}$. On the other hand, the TM flux is given by [27,28]:

$$J = C \frac{D}{kT} \frac{Q^*}{T} \left(-\frac{\partial T}{\partial x} \right) \quad (5-2)$$

where Q^* is the molar heat of transport, C is the concentration, D is the diffusivity, and kT is the thermal energy. The driving force of TM is given by:

$$F = -\frac{Q^*}{T} \left(\frac{\partial T}{\partial x} \right) \quad (5-3)$$

With a temperature difference across an atomic jump $\Delta T/\Delta x$, the thermal energy change would be $3k\Delta T$. When the TM force balances with the EM force, we have:

$$3k\Delta T = 4.98 \times 10^{-28} \text{ J}$$

which yields $\Delta T = 1.2 \times 10^{-5} \text{ k}$ across an atomic jump. Therefore, the critical thermal gradient goes to $400 \text{ }^\circ\text{C/cm}$. In other words, when the thermal gradient is greater than $400 \text{ }^\circ\text{C/cm}$, TM force on Cu atoms would be bigger than the EM force. Voids would form in the chip/anode end in Bump 2. Otherwise, voids would not be present in the chip/anode end for Bump 2. Instead, hillocks would form there. The results on the thermal gradient also agree with this calculation. As shown in Figure 3, the thermal gradient in Bump 2 reached $1643 \text{ }^\circ\text{C/cm}$, which is greater than the calculated critical gradient. Therefore, Cu atoms migrated toward the substrate side, which was against the direction of electrical current in Bump 2.

It is noteworthy that the critical thermal gradient varies with stressing current density and temperature. If the applied current decreases from 0.55 A to 0.4 A , the critical thermal gradient would also decrease to $290 \text{ }^\circ\text{C/cm}$ given the temperature remains the same.

(ii) SnAg with CuNi UBM

Theoretic calculation also supports that Ni-Sn compounds do not migrate under the above thermal gradients. If we take the effective charge number of Ni to be 67 [29], resistivity as $6.4 \times 10^{-8} \Omega \cdot \text{m}$, and the current density as $9.7 \times 10^7 \text{ A/m}^2$, the EM force is estimated to be $6.7 \times 10^{-17} \text{ N}$ using Eq. (5-1). The work done by the force in an atomic jump distance of $3 \times 10^{-10} \text{ m}$ is $2.01 \times 10^{-26} \text{ J}$. When the TM force is balanced with EM force, a temperature difference of $\Delta T = 2.415 \times 10^{-4} \text{ k}$ is needed across an atomic jump, which is equivalent to $8050 \text{ }^\circ\text{C/cm}$. That is, it needs a thermal gradient over $8050 \text{ }^\circ\text{C/cm}$ to observe thermal migration of Ni atoms during EM. The thermal gradients in the four bumps are much smaller than this value in the present study. Therefore, migration of Ni-Sn compounds was not observed in the SnAg solder joints.

5.3.4 Thermomigration Model

Basis on the above results, the following model is proposed to explain the interesting observation. Figures 5-10(a) through 5-10(c) illustrate the atomic migration in the four bumps. The atomic flux due to chemical potential is not considered in this model. Figure 5-10(a) depicts the atomic migration in Bumps 1 and 4. Only TM occurs in these two bumps because they were not subjected to current stressing. Copper atoms move to the cold end (substrate), whereas Sn atoms diffuse to the hot end (Si side). The flux of the Cu TM is much larger than that of Sn, as illustrated by the length of the arrows in the figures. For Bump 2 with an upward electron flow, the TM is the similar to that in Figure 5-10(a). EM force pushes the Cu and Sn atoms to the chip side, as presented in Figure 5-10(b). However, voids are still observed in the chip side. The results indicate that TM flux of Cu is larger than the sum of the fluxes of Cu EM, Sn EM, and Sn TM. This is mainly attributed that Cu

diffuses interstitially in Sn, and the diffusion rate is very fast. In addition, the built-in thermal gradient is very large. Figure 5-10(c) presents the atomic diffusion in Bump 3 with a downward electron flow. Both the EM and TM forces push the Cu atoms to the substrate side. In addition, the EM force also causes the Sn atoms to drift to the substrate side. Therefore, the downward flux appears to be the largest among the four bumps, resulting in the biggest void formation in the chip side.

5.4 Summary

In summary, TM in Pb-free SnAg solder joints with Cu and Cu/Ni UBMs has been investigated during accelerated EM tests under $9.7 \times 10^3 \text{ A/cm}^2$ at 150 °C. In solder joints with Cu UBMs, serious damage was observed in bumps subjected to the current stressing and in the bumps without current stressing. The damage is attributed to TM of Cu atoms. Theoretic calculations indicate that a critical thermal gradient of approximately 400 °C/cm was needed to observe TM during EM tests, above which the TM force would be bigger than the EM force. It is proposed that Cu-Sn IMCs migrate toward the cold end on the substrate end and, thus, deplete the passivation opening. The TM of the Cu-Sn has serious detrimental effect on the joints. Therefore, under stringent stressing conditions, TM of Cu-Sn IMCs plays a crucial role on the failure mechanism. On the contrary, the critical thermal gradient of approximately 8050 °C/cm was needed for the TM of Ni atoms. Therefore, it is difficult to observe TM in the EM test in solder joints with Ni UBMs. It also indicates that the Ni UBMs serves as an excellent diffusion barrier for Cu TM.

5.5 References

1. C. Chen, H.M. Tong and K.N. Tu, Annual Reviews Materials Research, **40**, 531 (2010).
2. L.D. Chen, M.L. Huang and S.M. Zhou, J. Alloys Compd. **504**, 535 (2010).
3. J.S. Zhang, Y.C. Chan, Y.P. Wu, H.J. Xi and F.S. Wu, J. Alloys Compd. **458**, 492 (2008).
4. H. J. Lin, J. S. Lin and T. H. Chuang, J. Alloys Compd. **487**, 458 (2009).
5. B. Chao, S. H. Chae, X. F. Zhang, K. H. Lu, J. Im and P. S. Ho, Acta Mater. **55**(8), 2805 (2007).
6. H. Ye, C. Basaran and D. C. Hopkins, Appl. Phys. Lett. **82**, 1045 (2003).
7. A. T. Huang, A. M. Gusak, K. N. Tu and Y. S. Lai, Appl. Phys. Lett. **88**, 141911 (2006).
8. S. H. Chiu, T. L. Shao, C. Chen, D. J. Yao and C. Y. Hsu, Appl. Phys. Lett. **88**(2), 022110 (2006).
9. J. W. Nah, J. H. Kim, H. M. Lee and K. W. Paik, Acta Mater. **52**(1), 129 (2004).
10. Y. H. Lin, Y. C. Hu, C. M. Tsai, C. R. Kao and K. N. Tu, Acta Mater. **53**(7), 2029 (2005).
11. T. L. Shao, S. W. Liang, T. C. Lin and C. Chen, J. Appl. Phys. **98**, 44509 (2005).
12. M. O. Alama, B. Y. Wua, Y. C. Chan and K. N. Tu, Acta Mater. **54**, 613 (2006).
13. J. W. Nah, K. W. Paik and J. O. Suh, J. Appl. Phys. **94**, 7560 (2003).
14. H. Y. Hsiao and C. Chen, Appl. Phys. Lett. **90**(15), 152105 (2007).
15. C. Chen and K. N. Tu, Annu. Rev. Mater. Res. **40**, 531 (2010).
16. H. Y. Chen, C. Chen and K. N. Tu, Appl. Phys. Lett. **93**, 122103 (2008).
17. H. Y. Hsiao and C. Chen, Appl. Phys. Lett. **94**, 092107 (2009).
18. Y. W. Chang, S. W. Liang and C. Chen, Appl. Phys. Lett. **89**(3), 032103 (2006).
19. H. B. Huntington. Diffusion (American Society for Metals, 1973), Chap. 6.

20. D. G. Kima, J. W. Kim, S. S. Ha, B. I. Noh, J. M. Koo, D. W. Park, M. W. Ko and S. B. Jung, *J. Alloys Compd.* **458**, 253 (2008).
21. C. J. Meechan and G. W. Lehman, *J. Appl. Phys.* **33**(2), 634 (1962).
22. K. Zeng and K. N. Tu, *Materials Science and Engineering Reports*, **R38**, 55 (2002).
23. R. W. Cahn and P. Haasen, *Physical Metallurgy*, forth ed. The Netherland: North Holland; 1996.
24. H. Y. Hsiao, S. W. Liang, M. F. Ku, C. Chen and D. J. Yao, *J. Appl. Phys.* **104**, 033708 (2008).
25. I. A. Blech, Diffusional back flows during electromigration, *Acta Mater.* **46**, 3717 (1998).
26. K. L. Lee, C. K. Hu and K. N. Tu, *J. Appl. Phys.* **78**(7), 4428 (1995).
27. P. G. Shewmon, *Diffusion in Solids* (TMS, Warrendale, PA, 1989), Chap. 7.
28. D. V. Ragone. *Thermodynamics of Materials* (Wiley, New York, 1995), Vol. 2, Chap. 8.
29. D. C. Yeh and H. B. Huntington, *Phys. Rev. B.* **53**(15), 1469 (1984).

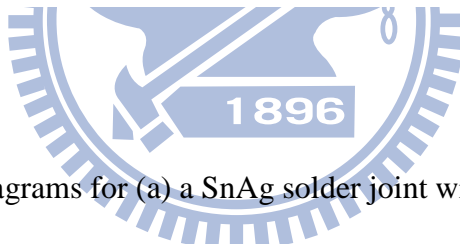
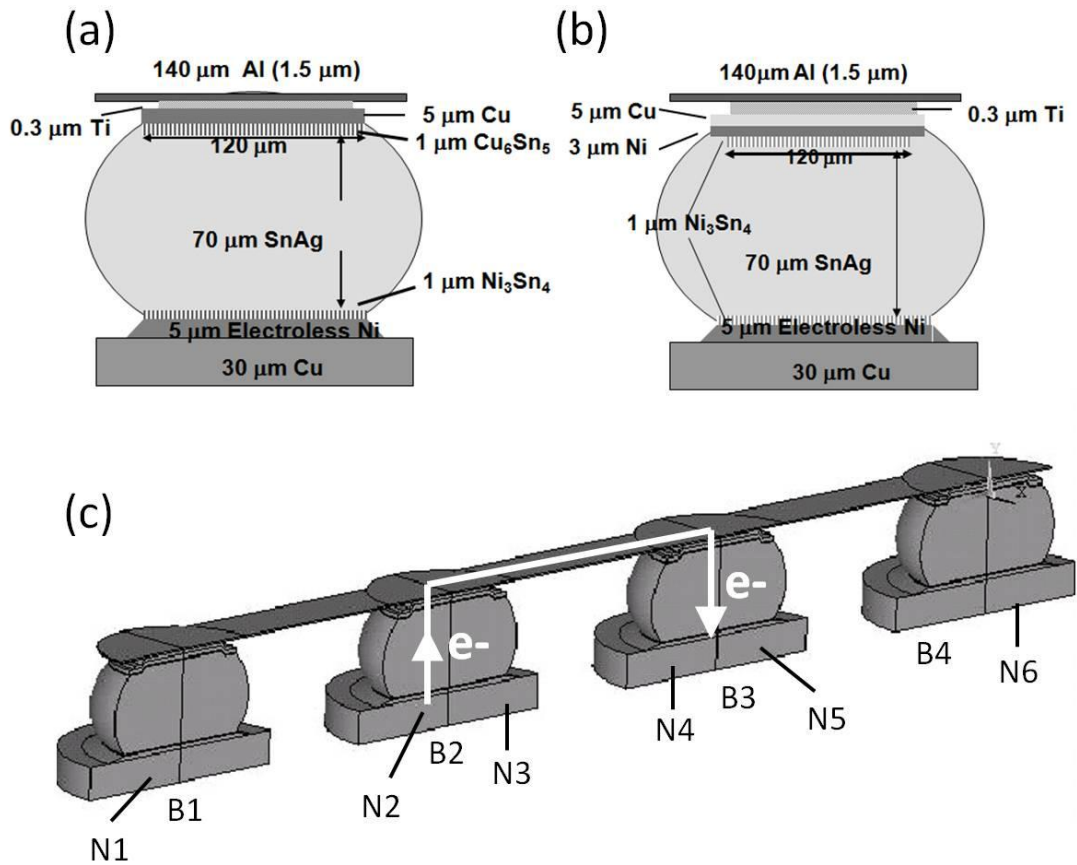


Figure 5-1 Schematic diagrams for (a) a SnAg solder joint with a 5- μ m Cu UBM, (b) a SnAg solder joint with a 5- μ m Cu/3- μ m Ni UBM, (c) cross-sectional view of the test layout. The electron flows are indicated by the arrows.

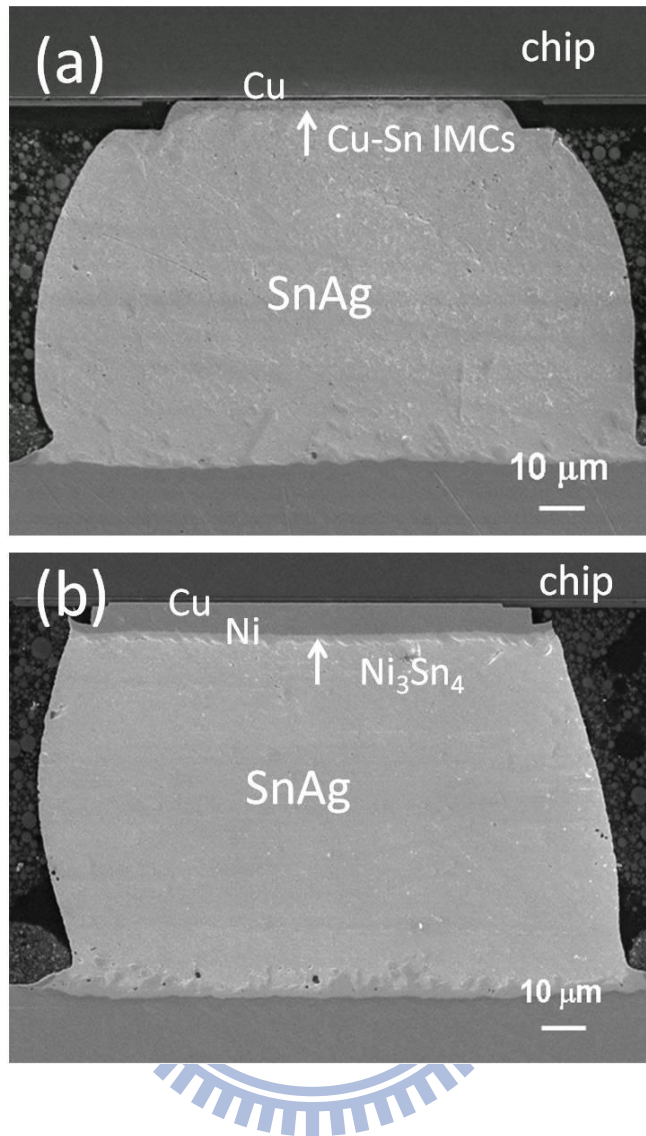


Figure 5-2 Back-scattered SEM images for solder bumps before current stressing. (a)

SnAg bump with a Cu UBM. (b) SnAg bump with a Cu/Ni UBM.

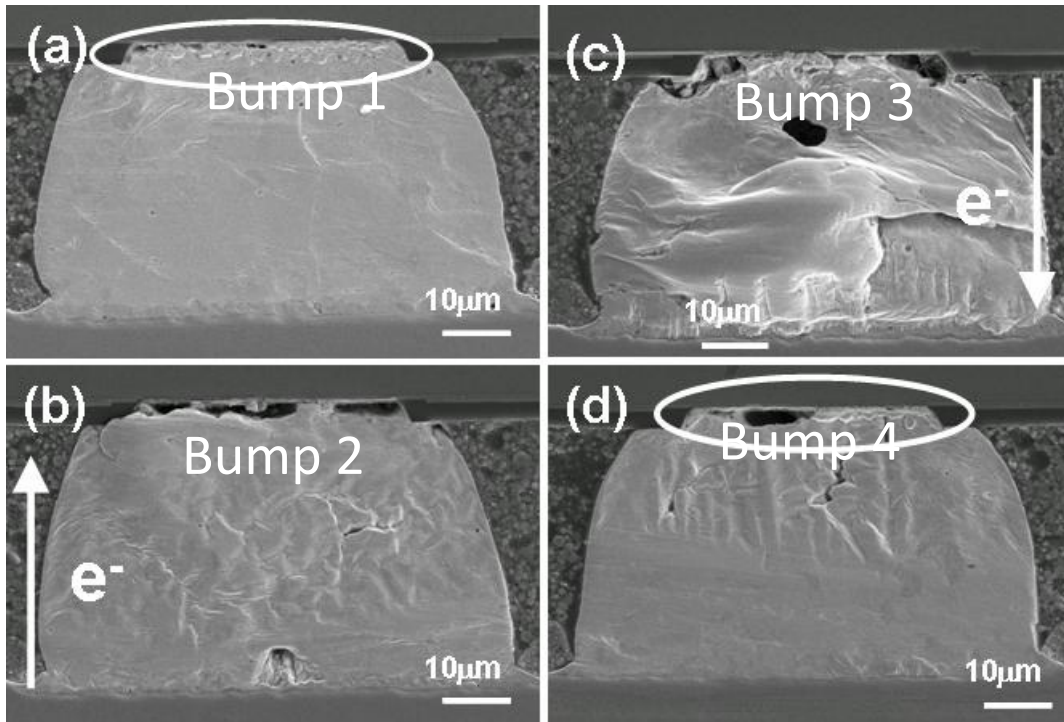


Figure 5-3 Cross-sectional SEM images showing the microstructures of the four bumps after the current stressing of 0.55 A through N3 and N4 at 150°C for 76 hrs. (a) Bump 1, (b) Bump 2 with a resistance increase of 200%, (c) Bump 3 with a resistance increase of 300%, (d) Bump 4. Voids formed in the chip side in all the four bumps.

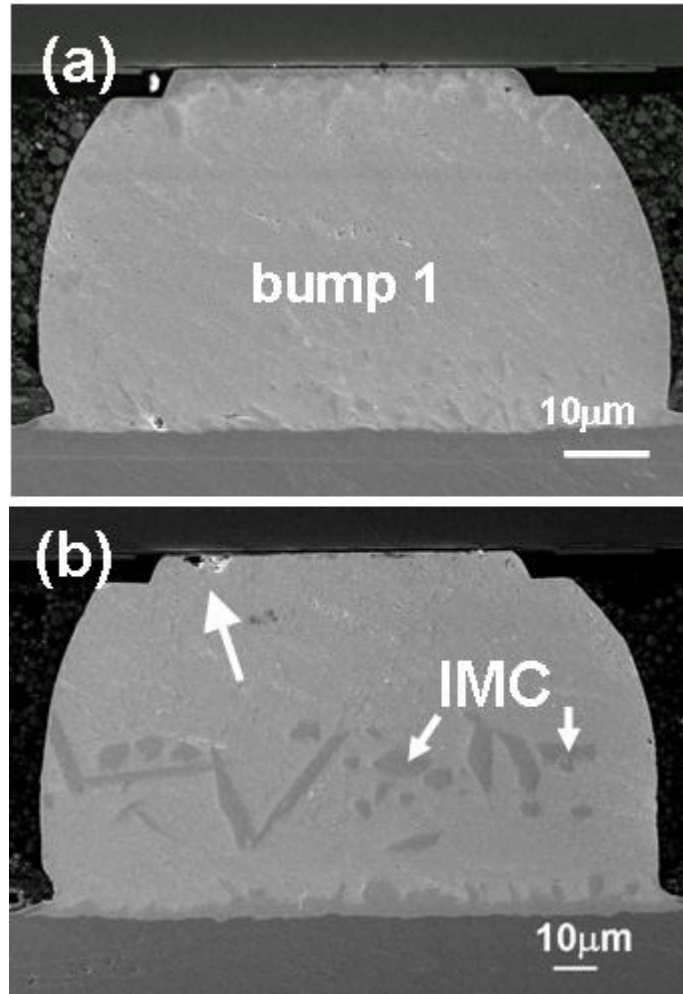


Figure 5-4 Cross-sectional SEM images representing the microstructure for the un-powered bump 1 in Cu UBM system before and after current stressing in bump 2 and 3 at 0.55A at 150°C for 60 hrs. (a) before, (b) after.

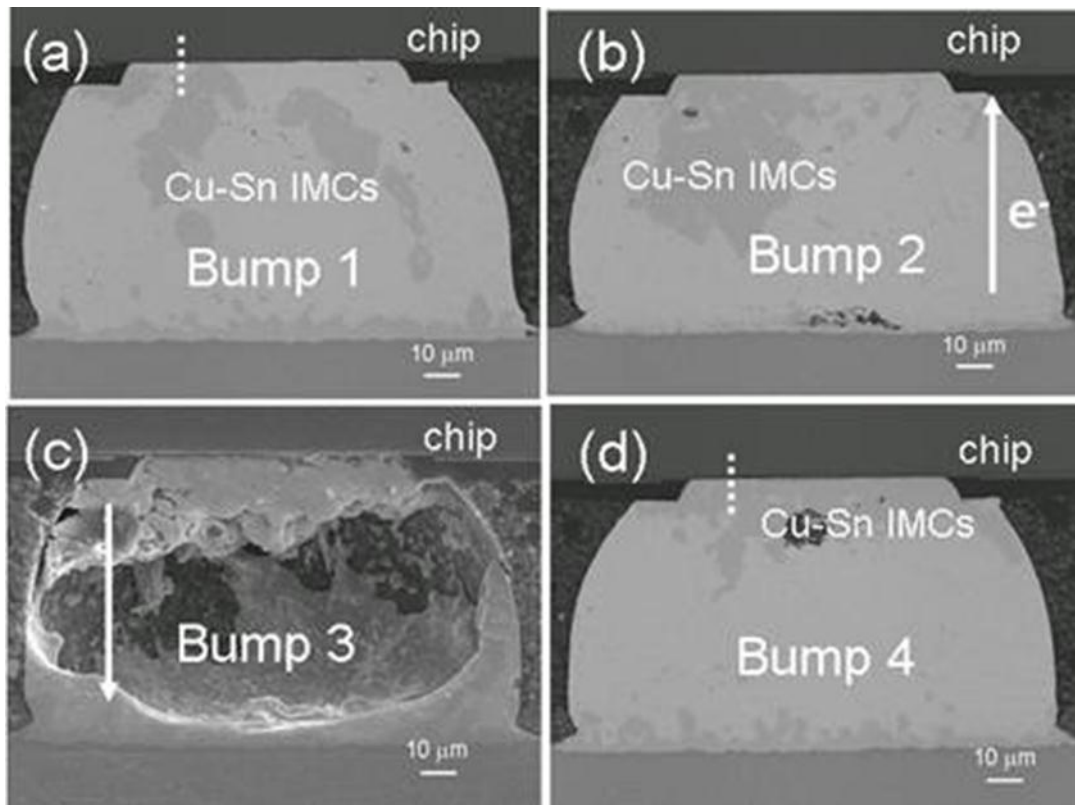


Figure 5-5 Cross-sectional BEI images showing the microstructures of another set of bumps after the current stressing at 0.55 A through N3 and N4 at 150°C for 82 hrs. (a) Bump 1, (b) Bump 2 with a resistance increase of 100%, (c) Bump 3 with a resistance increase of 350%, (d) Bump 4. Consumption of Cu UBM and spalling of Cu-Sn IMCs were observed in Bumps 1, 2 and 4.

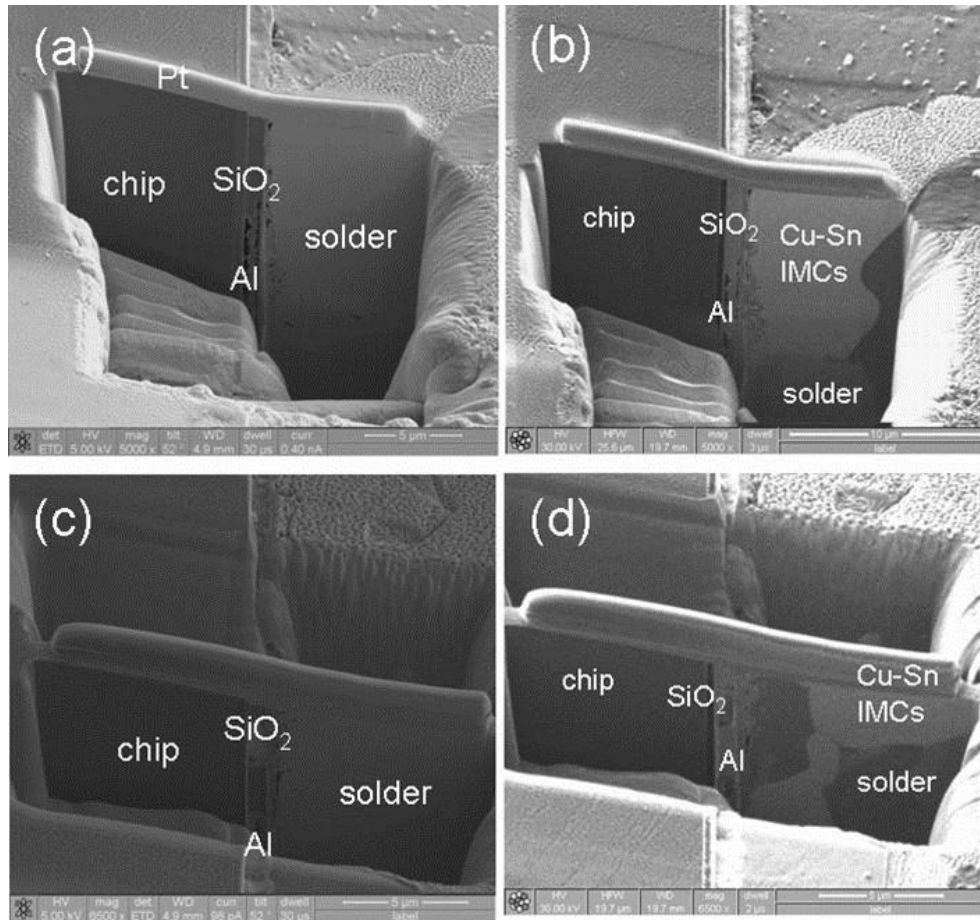


Figure 5-6 Microstructures at the interface of the chip and the solder after the current stressing of 0.55 A through Bumps 2 and 3 at 150°C for 82 h. (a) SEM image for Bump 1, (b) Ion image for Bump 1, (c) SEM image for Bump 4, (d) ion image for Bump 4.

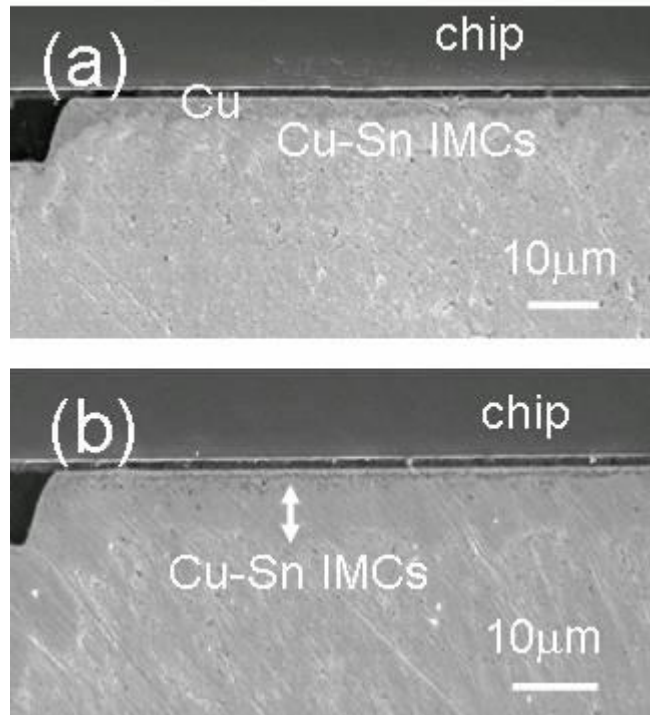


Figure 5-7 Enlarged cross-sectional SEM images of the chip-solder interface for (a) the bump before aging, and (b) the same bump after the aging at 165°C for 90 hrs. The Cu-Sn IMCs grew thicker, but no migration of Cu-Sn IMCs was observed.

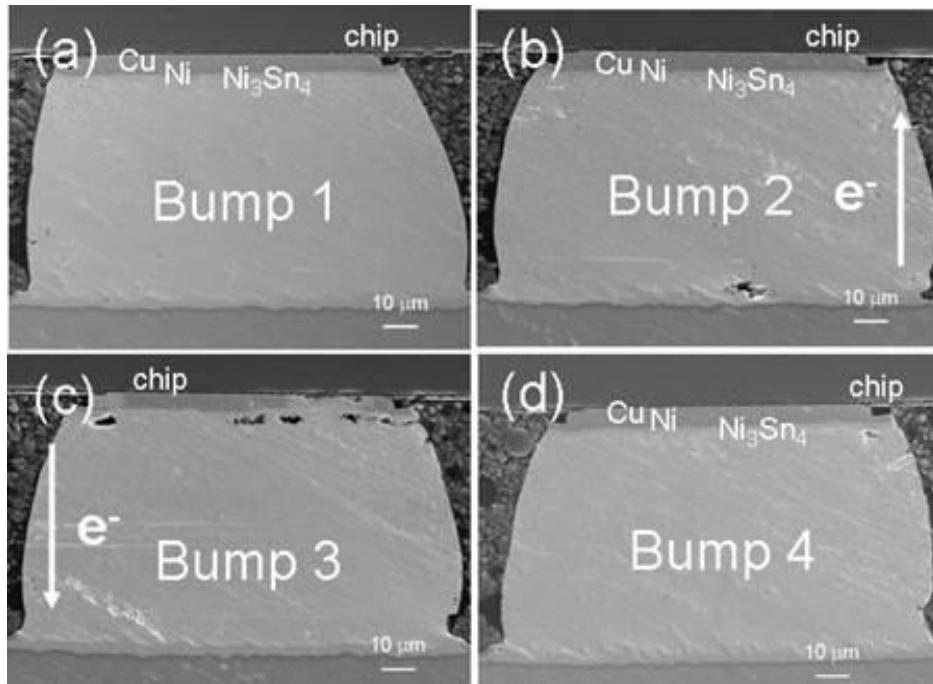


Figure 5-8 Cross-sectional SEM images of the solder joints with Cu/Ni UBMs after the current stressing at 0.55 A through N2 and N3 at 150°C for 180 hrs. (a) Bump 1, no current; (b) Bump 2, with an upward electron flow; (c) Bump 3, with a downward electron flow; (d) Bump 4, no current. Only electromigration damages were observed in the chip side of Bump 3.

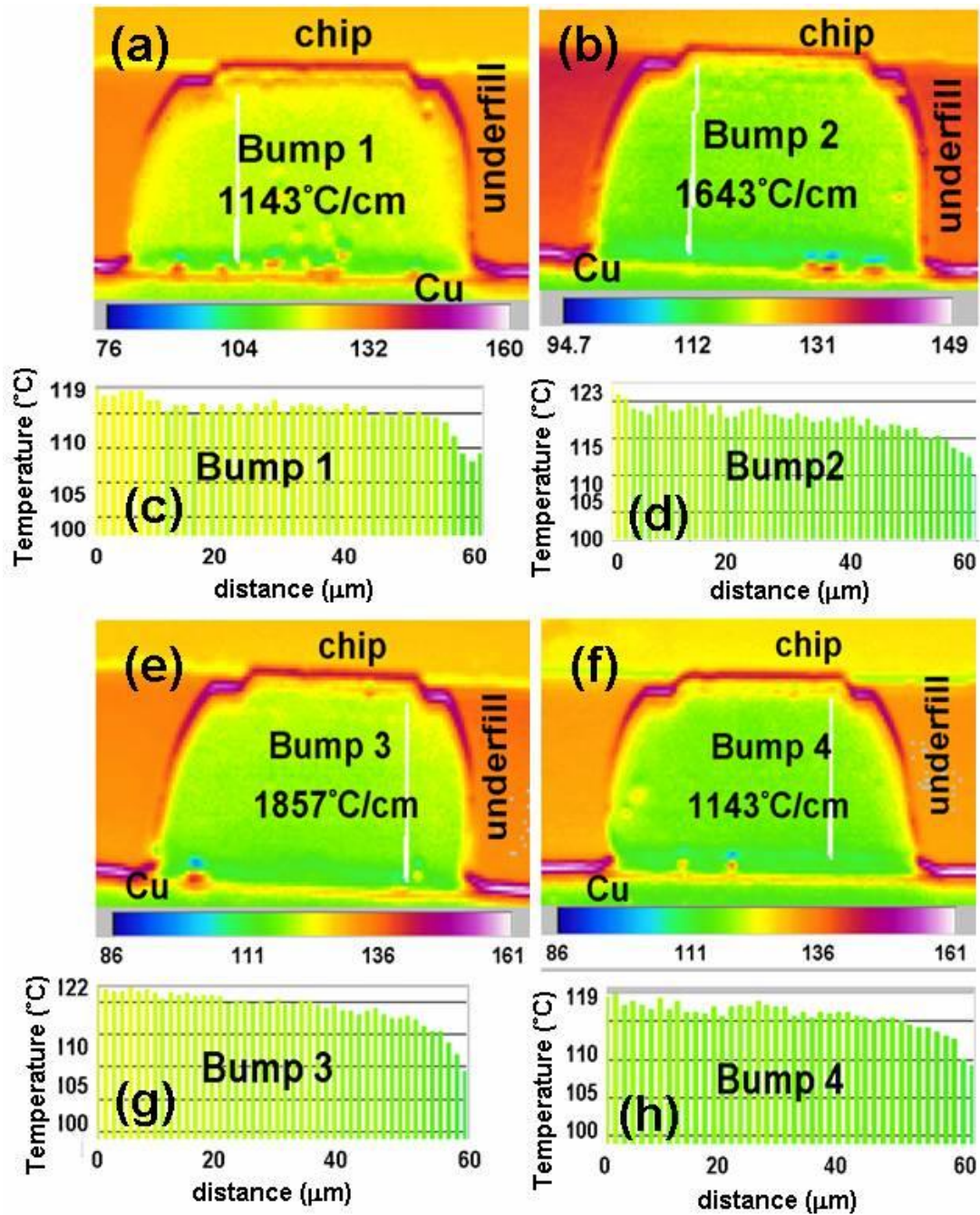


Figure 5-9 Temperature distributions in the four bumps with Cu UBMs. (a) Bump 1, no current; (b) Bump 2, with upward electron flow of 0.55 A; (c) temperature profile along the white line in (a); (d) temperature profile along the white line in (b); (e) Bump 3, with downward electron flow of 0.55 A; (f) Bump 4, no current; (g) temperature profile along the white line in (e); (h) temperature profile along the white line in (f). The temperature gradients are labeled on the bumps.

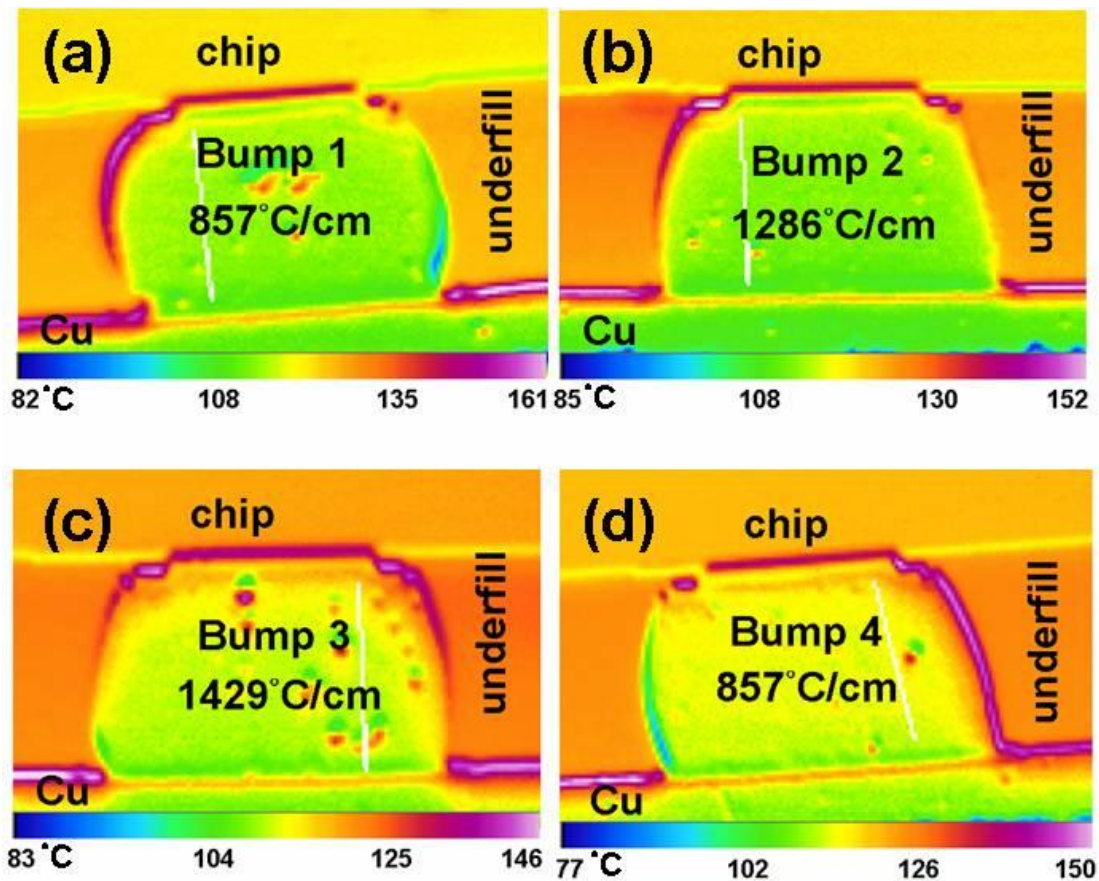


Figure 5-10 Temperature distributions in the four bumps with Cu/Ni UBMs stressed at 0.55 A through N3 and N4 at 100°C. (a) Bump 1, no current, and a temperature gradient of 857°C/cm; (b) Bump 2, with upward electron flow of 0.55 A, and a temperature gradient of 1286°C/cm; (c) Bump 3, with a downward current flow of 0.55 A, and a temperature gradient of 1429°C/cm; (d) Bump 4, no current, and a temperature gradient of 857°C/cm.

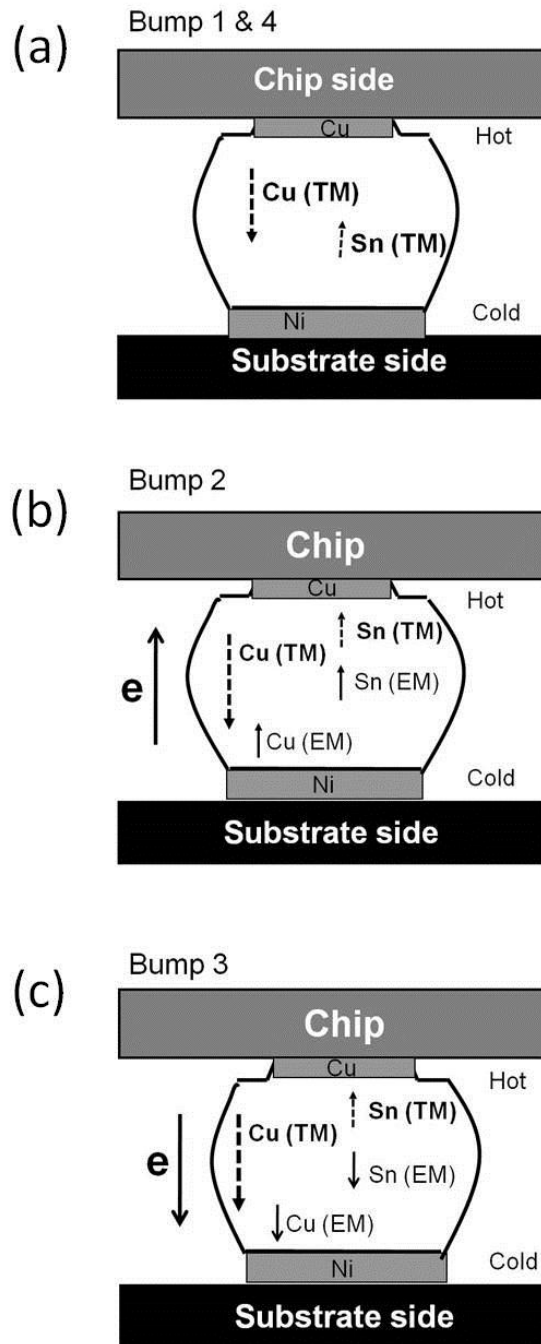


Figure 5-11 Schematic diagrams of the possible atomic fluxes of Cu- and Sn-caused electromigration and thermomigration. (a) Atomic fluxes in Bumps 1 and 4, which have no currents passing through: only thermomigration takes place. (b) Diffusion fluxes of Cu and Sn in Bump 2 with an upward electron flow. (c) Atomic fluxes of Cu and Sn in Bump 3 with a downward electron flow.

Chapter 6 Void Formation in Al Interconnects Induced by Ti Thermomigration and Al-Cu Reaction in Flip-chip Solder Joints

6.1 Introduction

Owing to continuous scaling down in dimensions and increasing demand for high performance devices, the current density in the devices and interconnects continues to increase. EM becomes a critical reliability issue [1-4]. During high current-density stressing, non-uniform heating takes place in the solder joint, resulting in TM damage in solder joints [5-8]. Recently, TM has attracted a lot of attention in flip chip solder joints. Since Al traces serve as the major heat source during accelerated EM tests, a non-uniform temperature distribution is produced and results in a large thermal gradient across the flip-chip solder joint [9]. This thermal gradient has been demonstrated to introduce a component of TM during accelerated EM tests [5,7,8]. Many efforts have been conducted to provide scientific understanding of this reliability issue in solder materials [5-12]. Pb atoms tend to migrate to cold end along the thermal gradient while Sn atoms tend to migrate to the hot end. It is also reported that TM also occurs in Cu, which serves as UBM [11]. Copper moves to the cold end in a thermal gradient. Among the UBM materials, Ti has been adopted as a diffusion barrier between the Al pad and the Cu UBM. Titanium has a high value of heat of transport, 768 kJ/mol [13,14]. It may be quite susceptible to migrate in a thermal gradient. However, no study has been performed to examine the TM of Ti.

In this chapter, damage in Al trace resulting from TM of Ti is reported in eutectic SnAg solder joints with Cu and CuNi UBM. It is found that TM of Ti atoms cause

damage in the diffusion barrier layer, and then Al may migrate into Cu UBM. Simulation results reveal a large a thermal gradient cross the Ti layer and therefore induced the TM of Ti atoms from the hot end toward the cold end. A comparison study on isothermal aging was performed to verify the results. Theoretical calculation was also conducted to support the observed phenomena.

6.2 Experimental Procedures

Cross-sectioned solder bumps were employed to facilitate the observation of the EM and TM damages. The test layout is shown in Figure 6-1(a). The dimensions of the flip-chip joints used in this study are shown schematically in Figures 6-1(b) and 6-1(c). The bump has a dimension of 130 μm in width and 75 to 80 μm in height with a UBM opening of 100 and 110 μm in diameter for Cu UBM and Cu/Ni UBM, respectively. The solder joints consist of eutectic SnAg solder bumps with electroplated 5- μm Cu UBMs or with electroplated 5- μm Cu/electroplated 3- μm Ni UBMs, as shown in Figure 6-1(b) and 6-1(c), respectively. The EM test layout consisted of four bumps. An electric current of 0.55 A was applied through nodes N3 and N4, producing a nominal current density about $9.7 \times 10^3 \text{ A/cm}^2$ in solder and $7.3 \times 10^5 \text{ A/cm}^2$ in Al trace, respectively. Yet the four bumps have experienced similar amount of Joule heating because the Al line connects four bumps together and the Si die possess excellent heat conduction. On the chip side, a 0.12 μm Ti layer was sputtered as an adhesion/diffusion-barrier layer between Cu UBM and the Al trace. Figure 6-2 shows the cross-sectional TEM image of the interface of the Al trace and the Cu UBM. A diffusion barrier of 0.2 μm Ti exists between the Al trace and the Cu layers. The bump height is approximately 70 μm . The diameter of the solder joint is about 150 μm and they were joined to an FR5 substrate. The dimension of Al trace in the chip side is 100 μm wide and 1.0 μm thick, while the dimension of the Cu lines on

the substrate was 25 μm thick and 100 μm wide. To observe the microstructure in the Al/Ti/Cu interface, FIB was adapted to produce a second surface at the interface between the Si die and solder to analyze the damage. Furthermore, TEM specimens were prepared by utilizing FIB. Three-dimensional (3D) finite element modeling was performed to analyze the temperature distribution across the interface because no experimental methods are able to analyze the temperature distribution in the 1.0 μm thick Al traces.

6.3 Results and Discussion

6.3.1 Void Formation inside Al Trace

Surprisingly, void formed in the Al trace of Bump 1 and Bump 4, which had no current passing through. Figure 6-3(a) shows the SEM image for the interface between the Si chip and solder in the Bump 4. A current stressing of 0.55 A was applied through Bump 2 and 3 at 150°C for 82 h. The Bump 4 experienced similar Joule heating effect as Bump 2 and 3. Although there was no current drifting in the Bump 4, a thermal gradient over 1000°C/cm may built up in the solder and thus TM may take place in the joint. Some voids in Al trace and in the Cu-Sn interfacial IMCs were observed after the TM test for 82 h, as shown in Figure 6-3(a). Figure 6-3(b) presents the FIB ion image of the interface and the Cu-Sn IMCs were observed more clearly. In our previously work reported that Cu is susceptible to move to cold end, resulting in the void formation in the original position of the Cu UBM. However, serious void formations were also observed in the Al trace. During the TM test, Si chip served as the hot end, whereas the substrate side was the cold end. Thus, the temperature in the Si was higher than that in solder in Figure 7-3. It is reported that Ti and Al has a positive heat of transport and it tends to move to cold end under a thermal gradient [13-15]. Thus, TM of Ti or Al may be responsible for the void

formation in the Al trace. Figure 6-4 shows the SEM images of Bump 1 after 82 hrs current stressing. Again, we can observe the undesirable void formation not just inside Al trace but also at the interface of originally UBM position due to Cu TM from hot end to cold end.

Evidence from Cu/Ni UBM also reveals the same trend here. The test condition is exactly the same as samples with Cu UBM, which is 0.55 A current stressing at 150°C. For Ni-Sn IMC TM, we did not get any microstructure change after test. In chapter 5, we already discussed about why we cannot get Ni-Sn IMC TM, therefore we now mainly focus on void formation inside Al trace. Figure 6-5(a) to (d) show SEM and ion images after 165 hrs EM test of Bump 1 and Bump 4, respectively. Clearly void formation inside Al trace can be observed and the Ti layer which is as the diffusion barrier between UBM and Al trace was partly disappeared after test.

Chemical potential may also have effect on the atomic migration. Al may react with Cu to form Cu-Al IMCs at elevated temperatures [16]. Yet there exist a diffusion barrier of 0.12 μm Ti film between the Al trace and the Cu UBM. Al atom may not be able to penetrate the diffusion layer at the present condition. To verify whether the chemical potential may play a role in the void formation in the present condition, a heat treat was conducted in another solder bumps. Chen *et al* reported that the current stressing of 0.55 A may impose a temperature increase of approximately 15°C. Therefore, a heat treatment was performed on the solder bump at 165°C for 90 h. Figure 6-6 depicts the cross-sectional FIB ion image for the interface structure of the annealed sample. No voids were observed in the Al trace. Only some Kirkendall voids were found at the interface of Cu_3Sn and Cu_6Sn_5 , which is attributed to the phase transformation of Cu_6Sn_5 into Cu_3Sn [17]. Therefore, the force of the chemical potential at the present condition was not big enough to migrate Al atoms through the Ti layer and to form Al-Cu IMCs.

Results from TEM analysis indicates that Cu-Al IMCs formed after the TM test. Figure 6-7 shows the cross-sectional TEM image for the damaged Al trace. Perfect Ti layers, which are between SiO₂ and Al trace and between Al trace and Cu UBMs can be obtained as we received. Some voids formed in the Al trace, as indicated by the arrows in the figure. In addition, the Ti layer between the Al and Cu layers disappeared. TEM-EDX was performed to identify the composition of the IMCs near the Ti/Cu interface. IMCs of Cu₉Al₄ were detected near the interface. The above results suggested that TM of Al or Ti may be mainly responsible for the void formation. As shown in Figures 6-2 and 6-3, the Al trace had no voids at where the Ti layer stayed intact. Once the Ti layer was destroyed, the Al may diffuse into Cu UBM to form Cu-Al IMCs [14-16]. Therefore, the Ti layer plays critical role on the void formation in the Al trace. It is reported that Ti may react with Al to form Al₃Ti at temperatures above 350°C [18]. However, if the temperature is at 165°C and uniform, as in thermal aging in Figure 3, the reaction between Al and Ti may not take place. However, under a large thermal gradient, the Ti TM may occur and the Ti layer became discontinuous. We propose that the large thermal gradient may trigger the atomic migration and thus facilitate the formation of Al₃Ti. Furthermore, as soon as the Ti layer is consumed, the Al may react with Cu UBM. Hentzell *et al* reported that the Cu-Al reaction may take place at 200°C for 1 h [19]. Once the Al diffuse into the Cu UBM to form Al-Cu IMCs, voids form in the Al trace.

6.3.2 Theoretical Calculation

The TM forces of Ti, Al and Cu are estimated, and Ti has the largest value among the three elements. The TM force is described as [20]

$$F = -\frac{Q^*}{T} \left(\frac{\partial T}{\partial x} \right) \quad (6-1)$$

where T is the temperature, x is the distance, and Q^* is the heat of transport. It is reported that the three materials all migrate to the cold end. If we assume that thermal gradient is approximately the same as that in the solder bump, which is around 1000 °C/cm in the present condition. Finite element simulation was contract out to simulate the thermal gradient in the Al/Ti/Cu layers.

For Al, the heat of transport is taken as -8.36 kJ/mole [21]. Then the TM force is calculated to be 3.1×10^{-20} N for Al under our test condition. On the other hand, the heat of transport of Cu is -22.6 kJ/mole [13]. The thermal gradient in the solder is also about 1000 °C/cm. Therefore the TM force of Al is in the same order with the Cu. That means, Al might TM under this test condition from hot end to cold end, and then resulted in void formation inside Al trace as we observed.

6.3.3 Simulation Results

Figure 6-8(b) reveals the temperature distribution along the straight line in Figure 6-8(a). The measured point starts from the top of Al trace and goes further downward into the Cu UBM. The thermal gradient cross the 1.0 μm Al is calculated to be 500°C/cm. On the other hand, we have the thermal gradient reached to 1200°C/cm since the Ti layer is very thin. Ti possesses a huge value of heat of transport [21,22], which is 768 kJ/mole toward the cold end. Thus, it is highly susceptible to migrate under a thermal gradient. The TM force is then calculated to be 3.5×10^{-18} N for the Ti. The force is approximately two orders in magnitude larger than those of Al and Cu. In other words, Ti may migrate under our test condition.

In fact, Ti TM might be the main reason that we can observe failure inside Al trace. Ti is diffusion barrier, in other words, as long as Ti layer is intact, we cannot obtain Al-Cu IMCs and Al atom flux from hot end which is Si side to cold end.

6.4 Summary

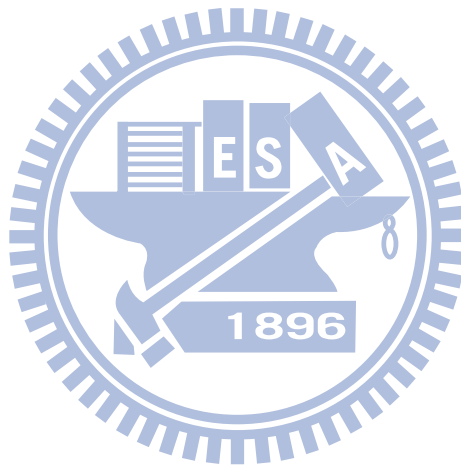
In summary, the TM behaviors of lead-free solders have been investigated under a current density of $9 \times 10^3 \text{ A/cm}^2$ at 150°C . Void formation was observed in Al trace which is without current passing through above Bump 1 and 4. The TM of Al and Ti from hot end toward the cold end left behind supersaturated vacancies was proposed for the void formation and resulted in failure.



6.5 References

1. W. J. Choi, E. C. C. Yeh, K. N. Tu, J. Appl. Phys. **94**, 5665 (2003).
2. C. Chen, H.M. Tong, K.N. Tu, Annual Reviews Materials Research, **40**, 531 (2010).
3. Hu, C. K., Rodbell, K. P., Sullivan, T. D., Lee, K. Y. and Bouldin, D. P., IBM J. Res. Develop., **39**, 465 (1995).
4. E.C.C. Yeh, W.J. Choi, K.N. Tu, P. Elenius, and H. Balkan, Appl. Phys. Lett. **80**, 580 (2002).
5. H. Ye, C. Basaran, and D. Hopkins, Appl. Phys. Lett. **82**,1045 (2003).
6. S. H. Chiu, T. L. Shao, and C. Chen, Appl. Phys. Lett. **88**, 022110 (2006)
7. A. T. Huang, A. M. Gusak, K. N. Tu, and Y.-S. Lai, Appl. Phys. Lett. **88**,141911 (2006)
8. H. Y. Hsiao and C. Chen, Appl. Phys. Lett. **90**, 152105 (2007).
9. H. Y. Hsiao, S. W. Liang, M. F. Ku, C. Chen, D. J. Yao, J. Apple. Phys. **104**, 033708 (2008).
10. H. Y. Hsiao, C. Chen, Appl. Phys. Lett. **94** (2009) 092107.
11. H. Y. Chen, C. Chen, K. N. Tu, Appl. Phys. Lett. **93**, 122103 (2008)
12. H. Y. Chen, C. Chen, J. Mater. Reserch. In press.
13. R. W. Cahn and P. Haassen, Physical Metallurgy (North, Holland) Chap. 7
14. F. W. Wulff, C. D. Breach, D. Stephan, Saraswati and K. J. Dittmer, EPTC 2004. Proceedings of 6th pp. 348-353
15. P. G. Shewmon, Diffusion in Solids, Second ed., TMS, Warrendale, Pa, 1989.
16. Phase diagram book.
17. K. Zeng JAP K. Zeng, R. Stierman, T. C. Chiu, D. Edwards, K. Ano, K. N. Tu, J. Appl. Phys. **97**, 024508 (2005).
18. J. Tardy, K. N. Tu, Phys. Rev. B. **32**, 2070 (1985).

19. H. T. G. Hentzell, R. D. Thompson, K. N. Tu, *J. Appl. Phys.* **54**, 6923 (1983).
20. D. V. Ragone, *Thermodynamics of Materials* (Wiley, New York, 1995), Vol. 2, Chap. 8.
21. J. H. Matlock and J. P. Stark, *Acta Mater.* **19**, 923 (1971).
22. R. W. Cahn and P. Haassen, *Physical Metallurgy* (North, Holland) Chap. 7
23. F. W. Wulff, C. D. Breach, D. Stephan, Saraswati and K. J. Dittmer, EPTC 2004. Proceedings of 6th pp. 348-353



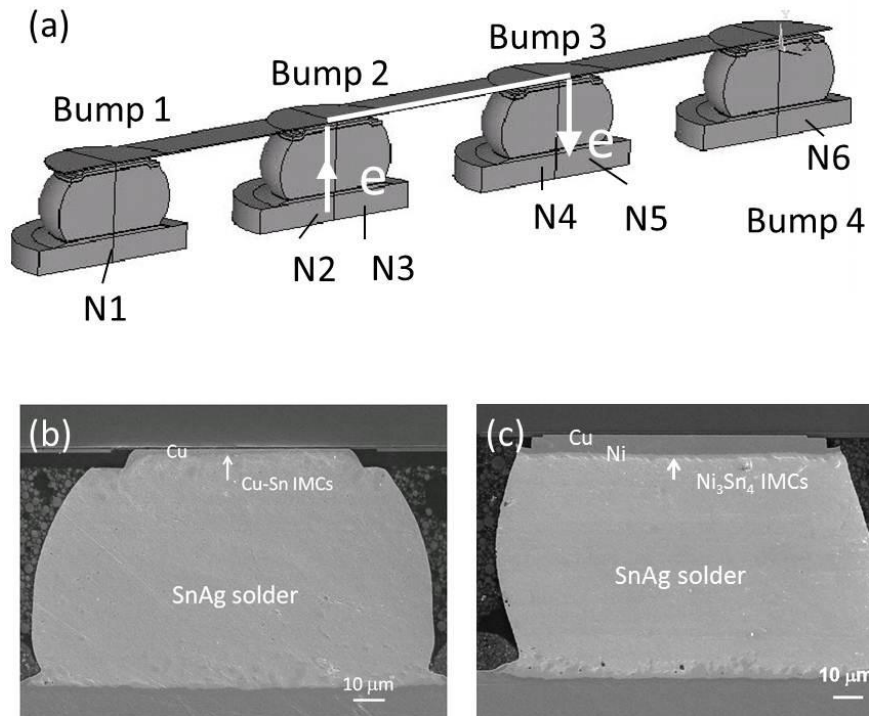


Figure 6-1 (a) Cross-sectional schematic of the layout design. An Al trace connected all the four solder bumps together. (b) Cross-sectional SEM image showing that the microstructure for the solder bump used in this study with Cu UBM. (c) Cross-sectional SEM image with Cu/Ni UBM.

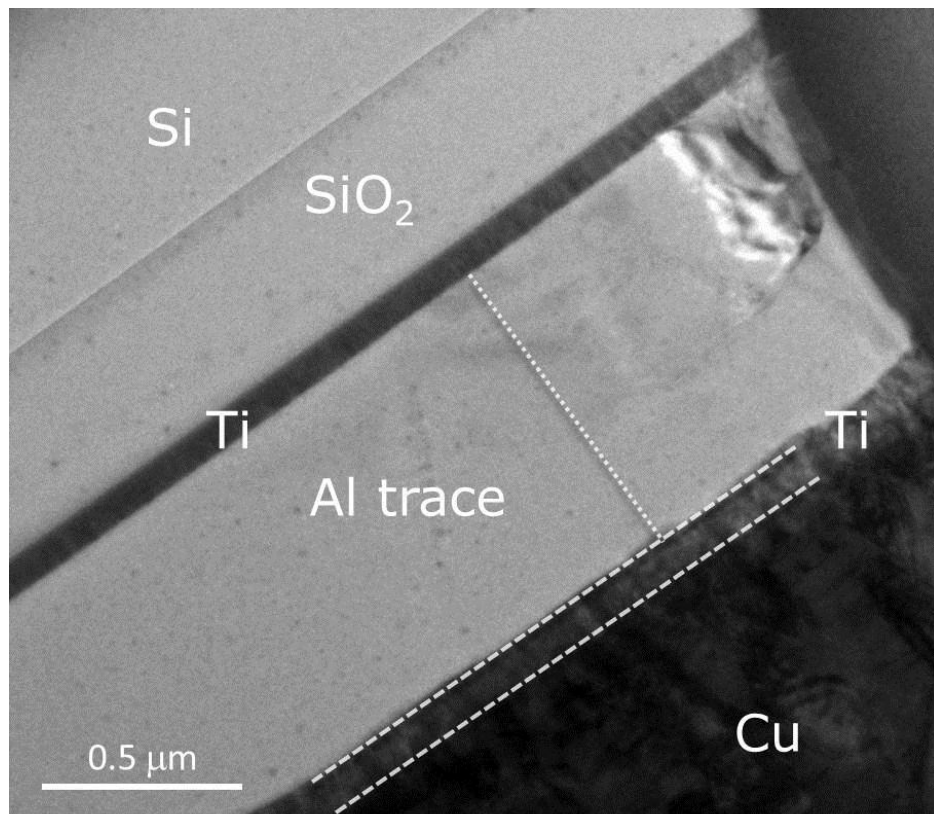


Figure 6-2 Cross-sectional TEM image of interface in the chip side before current stressing.

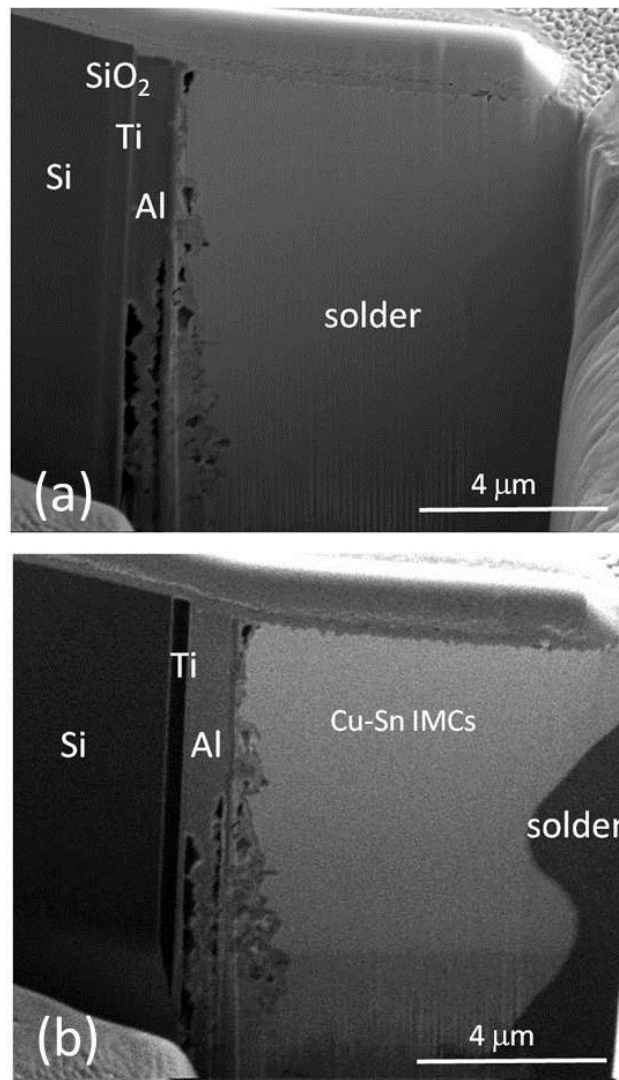


Figure 6-3 (a) Cross-sectional SEM image for Bump 4, showing the microstructures at the interface of the chip and the solder after the current stressing of 0.55 A through Bumps 2 and 3 at 150°C for 82 hrs, (b) FIB ion image for Bump 4 on the same area of (a).

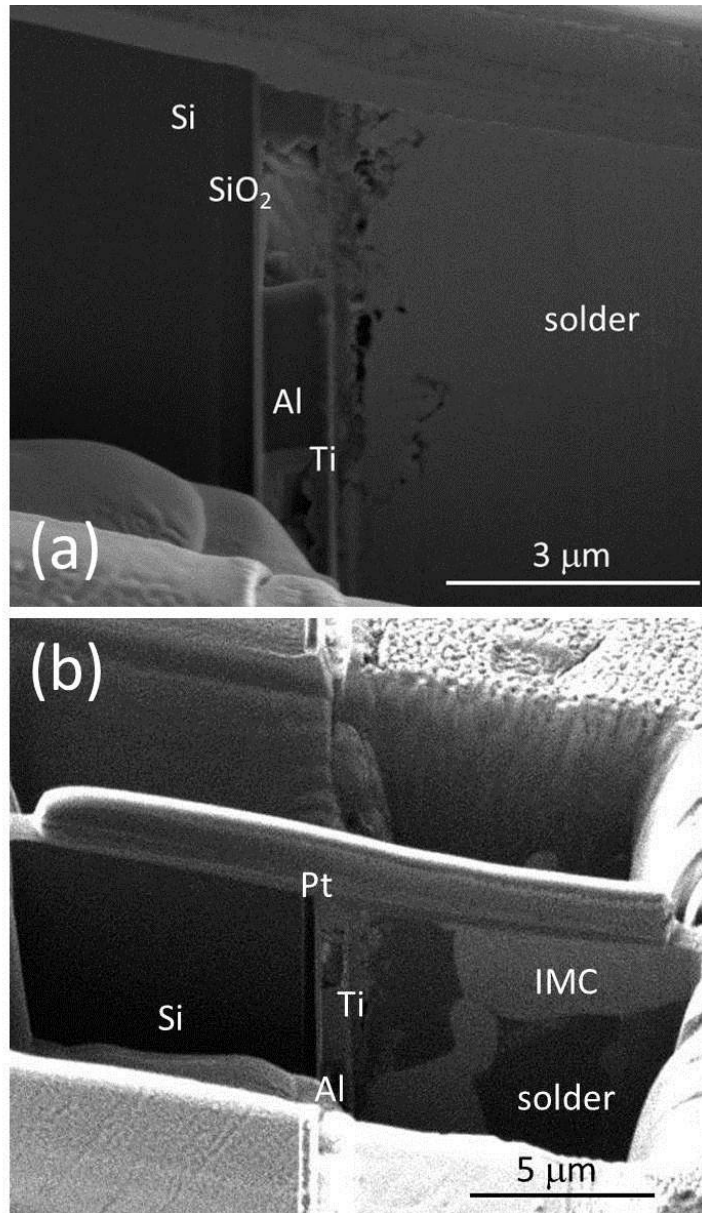


Figure 6-4 (a) Cross-sectional SEM image for Bump 1, showing the microstructures at the interface of the chip and the solder after the current stressing of 0.55 A through Bumps 2 and 3 at 150°C for 82 hrs, (b) FIB ion image for Bump 4 on the same area of (a).

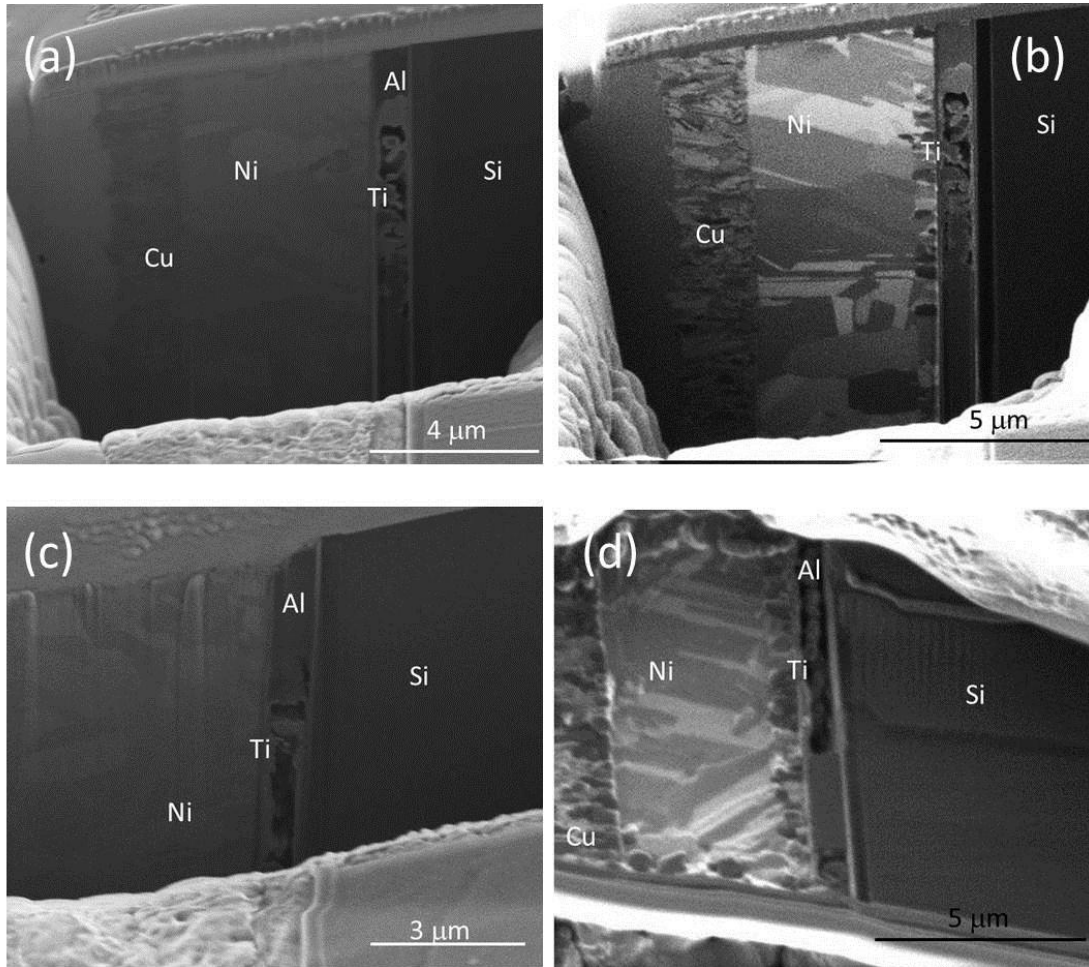


Figure 6-5 (a) Cross-sectional SEM image for Bump 1, showing the microstructures at the interface of the chip and the solder after the current stressing of 0.55 A through Bumps 2 and 3 at 150°C for 165 hrs, (b) FIB ion image for Bump 1 on the same area of (a). (c) Bump 4 after current stressing. (d) FIB ion image for Bump 4 on the same area of (a)

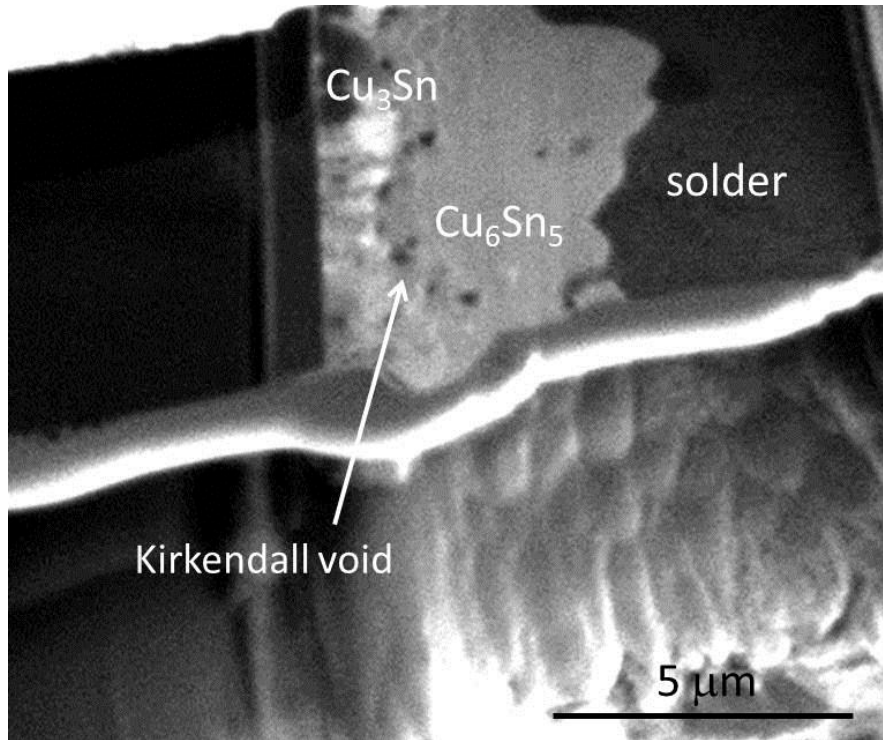
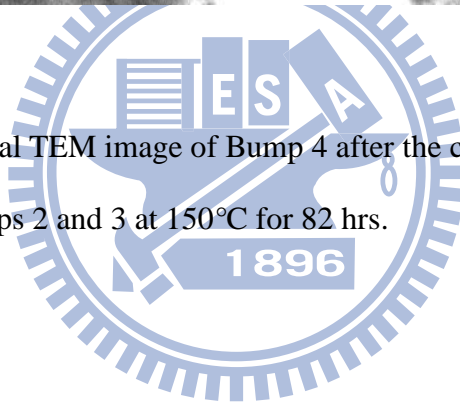


Figure 6-6 Cross-sectional TEM image of Bump 4 after the current stressing of 0.55 A through Bumps 2 and 3 at 150°C for 82 hrs.



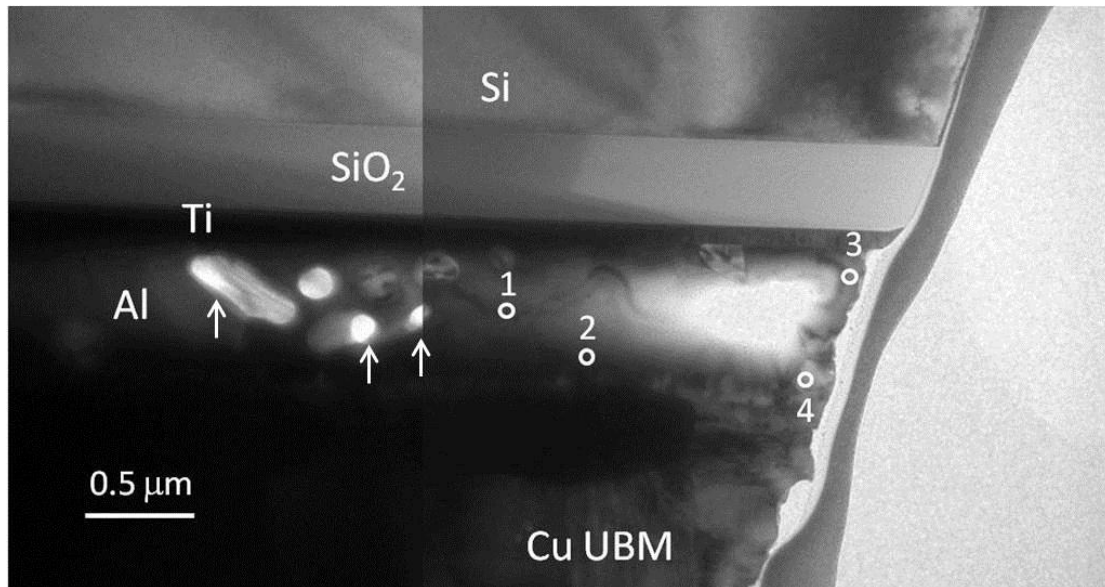
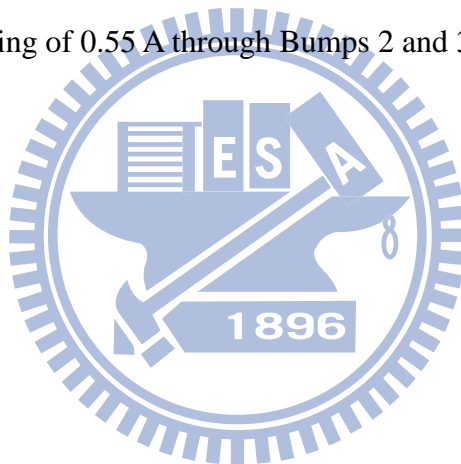


Figure 6-7 Cross-sectional TEM image of the Al/Cu interface for the Bump 4 after the current stressing of 0.55 A through Bumps 2 and 3 at 150°C for 82 hrs.



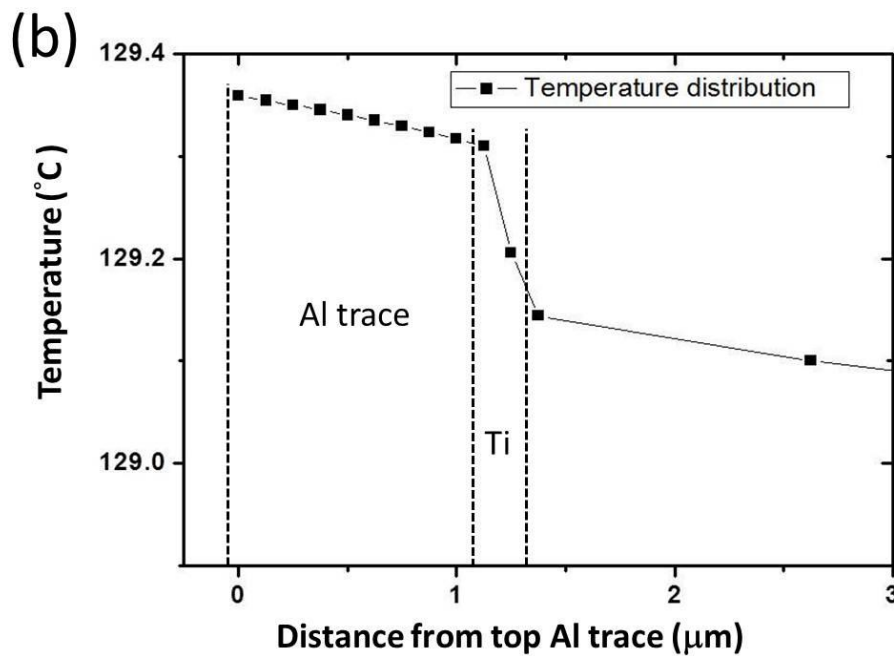
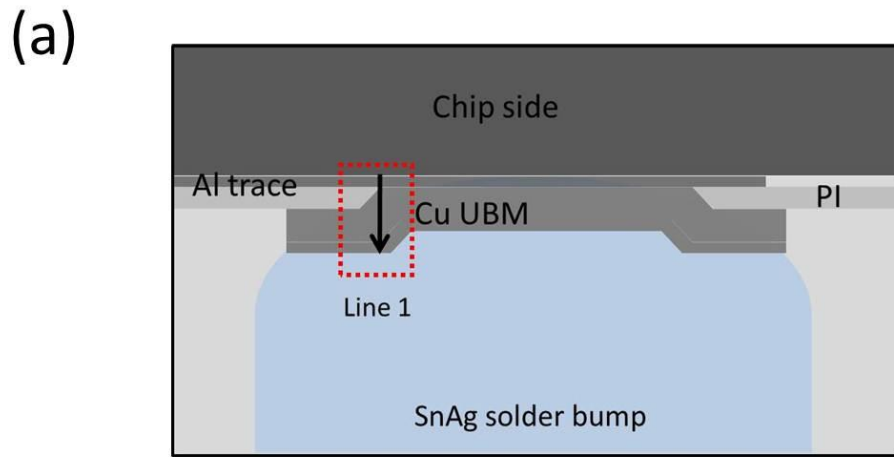
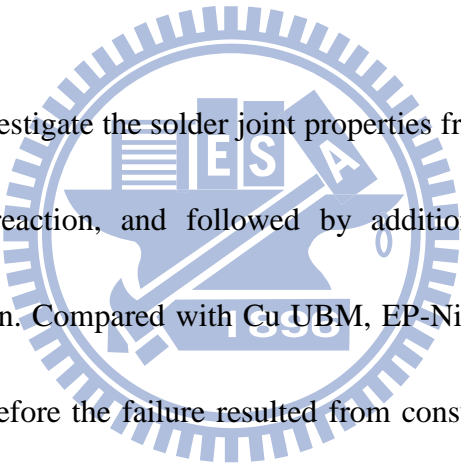


Figure 6-8 (a) Schematic structure of Bump 4 for simulation. (b) Temperature distribution along line 1 in Bump 4.

Chapter 7 Conclusion and Future Work

7.1 Conclusion

The reliability issue of solder joint technology in microelectronic packaging industry has been a concern for long time, for example, the mechanical property, electrical property and thermal property which can affect the solder joint life time. Electromigration, which is an the effect of external force can lead to phase change and thermomigration, on the other hand, phase change due to a temperature gradient across solder bumps



In our work, we investigate the solder joint properties from the very fundamental mechanical interfacial reaction, and followed by additional current stressing to simulate the real situation. Compared with Cu UBM, EP-Ni UBM possesses a much slower reaction rate therefore the failure resulted from consumption of UBM should be no longer an issue here. On the other hand, from the mechanical point of view, EP-Ni have much higher internal stress due to the plating process, we might need to take this into consideration carefully. However, higher resistivity and slower reaction rate of EP-Ni do bring industry benefit while choosing it as UBM. An additional layer of higher resistivity EP-Ni helps redistribute current route and the corresponding temperature distribution; therefore we can obtain longer EM life time in CuNi system.

By utilizing Al TCR effect, we can calibrate solder bump temperature during

current stressing and thus we can obtain more accurate EM activation energy different from others work. Compared with Cu UBM system, the EM activation energy of CuNi UBM system, which is about 0.85 eV after calibration is mostly related to void formation and void propagation in our systematically analyze. Different from CuNi UBM system, the EM activation energy of Cu UBM are mainly related to UBM consumption and IMC formation. The EM activation energy is 1.05 eV for SnAg solder, which is very close to IMC formation between Cu and SnAg (1.06 eV); on the other hand, the activation energy is 0.87 eV after calibration for SnPb solder and also very close to IMC formation between Cu and SnPb (0.94 eV).

Besides EM, failure due to unique TM behavior of Cu-Sn through fast interstitial diffusion of Cu into Sn-based solder joints can also be obtained. With a large thermal gradient across solder joint, Cu-Sn IMC would migrate from hot end (chip side) to cold end (substrate side). This special phenomenon gives us a chance to reconsider and redesign the adoption of Cu as UBM. Moreover, under such great thermal gradient, Ti TM and Al TM should be taken into consideration as well for the failure can be observed inside Al trace in powered or unpowered bumps. Here in our study, the model of TM of Ti, which is always used as diffusion barrier to keep Al and Cu reaction, firstly migrate towards cold end can be obtained and then followed by TM of Al. The net atomic flux from chip side to substrate side of Ti and Al induce the

reverse vacancy flux from cold end to hot end, therefore we have void formation inside Al trace.

To sum up, the adoption of EP-Ni can be evaluate from different points of view, mechanical, electrical and thermal to have a better understanding. Other phenomenon can also be analyzed by EM and TM experiments.

7.2 Future Work

Three-dimensional integration chip (3DIC) is a promising technology to further improve the performance of computational systems and therefore the shrinkage of the outside packaging is inevitable. For scaling down packaging system, all the force would be magnified as well, therefore we should take the EM, TM and even stress migration (SM) into consideration very carefully. For the information we have so far from flip-chip technology, it is a good start to apply to the so called micro-bump. Even though there should be a little bit difference between flip-chip bump and micro-bump, they still have many things in common.

For interfacial reaction, it will become more and more important since we will have very little solder volume when it comes to micro-bumps, therefore the IMC formation and the UBM consumption will be a serious issue in the future. For EM, current density may be reach to as high as 10^4 or 10^5 A/cm², or even higher, which can

lead to very severe damage. The following TM and SM should be reconsidering as well. Therefore, from flip-chip technology to micro-bump technology, we still have lots of work to do. In the prospective study, it will be interesting to study all the behavior, including interfacial reaction, EM, TM and SM as well, with micro-bumps and compared with flip-chip bumps.



Appendix Effect of Polyethylene Glycol Additives on Pulse Electroplating of SnAg Solder

A.1 Introduction

The adoption of flip chip technology has received increasing acceptance for high density and fine pitch interconnection [1]. In flip chip bumping process for high volume production, the electroplating method is considered to be the most efficient fabrication approach among possible solutions to deliver fine pitch configuration at reasonable cost [2-4]. Conventional solder material employs alloy of Pb and Sn. Codeposition of Pb and Sn via electroplating is relatively straightforward as both elements exhibit similar standard reduction potential (Sn^{2+} : -0.136V and Pb^{2+} : -0.125V). With rising emphasis of “lead-free” material, the Pb-Sn solder itself has become the primary target for replacement. Hence, electroplating of alternative binary alloy such as Sn-Ag[5-11], Sn-Bi [12-13], Sn-Cu [14-15], as well as ternary system of Sn-Ag-Cu [16-17] has been aggressively pursued.

Unfortunately, due to intricate interactions between thermodynamics and kinetics, today's plating technology is unable to deliver exact ternary composition at wafer level requirement. As a result, binary SnAg and SnCu solders are used in applications for flip chip technology. Between them, Sn-Ag is better suited to replace Pb-Sn because its intrinsic properties such as melting temperature and surface tension are closely resembled to those of Pb-Sn alloys [18].

However, there are inherent challenges associated with electroplating of Sn-Ag alloy. First, in the Sn-Ag binary phase diagram, a small deviation of Ag amount from the eutectic composition (Sn-3.5wt% Ag) induces substantial increase of temperature along solidus line. This leads to higher working temperature in subsequent soldering

operation. For process reliability and repeatability, therefore, it is preferred to acquire the deposited film at exact eutectic composition. Secondly, Ag^+ exhibits a much more positive standard reduction potential (0.799V) than that of Sn^{2+} (-0.136V). As a result, Ag^+ would be favored for “plating out” in electrolyte solution and the composition of the derived film differs substantially to that of electrolyte phase. In contrast, the difference of standard reduction potential between Sn^{2+} and Pb^{2+} is much smaller ($\Delta E = 0.0113 \text{ V}$) [19], ensuring sufficient composition replication from electrolyte phase to the plated film.

To mitigate relatively high activity of Ag^+ , complexing agent is used to stabilize Ag^+ for retardation of preferential precipitation. Electrodeposition of binary alloy with large difference in standard reduction potentials has been well-documented with the aid of complexing agents [20,21]. For example, using citrate, glycine, and triethanolamine as complexing additives, Mizushima et. al. have achieved optimized Ni-W alloy film with minimized residual stress [22,23]. The concentrations of complexing agent and Ag^+ in plating solution require diligent control for targeted film composition. To sum up, in order to proceed electroplating of Sn-3.5wt% Ag as intended, strict controls over plating formulations, additives, and plating methods are critical.

Pulse electrodeposition is known to produce alloy film with varied materials properties. Recently, in Cu-Ni alloy system it was reported that composition, lattice constant, and magnetic property could be controlled by parameters used in pulse plating[24]. In addition, pulse plating using on-off mode has been reported to yield elaborate bump with smooth and homogeneous surfaces using triethanolamine, triton X-100, sorbitol, sodium gluconate, and 1,4-hydroxybenzene as agent [25]. Further, additives such as polyethylene glycol (PEG) has been studied extensively as inhibitive agent in electroplating of Cu for integrated circuit fabrication [26-30]. However, its

applicability to SnAg plating formulation is still unknown. In this paper, we explore the pulse plating with alternative polarities on SnAg plating solutions containing PEG with different molecular weights. Electrochemical analysis of the plating formulations and characterization of the resultant deposits were performed to identify proper plating parameters for desirable eutectic Sn-3.5wt% Ag solder film.

A.2 Experimental Procedures

The experiment for electrochemical deposition of SnAg film was conducted in a tank of non-conducting polymeric material. To study the physical properties of SnAg alloy, a Ti plate of 10 cm x 10 cm was used as the counter electrode and a Si wafer of 2 cm x 3 cm as an working electrode. An overcoat of Cu (~1 μm) was sputtered onto the wafer as conductive layer prior to electroplating. The electrodeposition process was carried out in pulse plating mode at 25°C in which the working electrode was imposed with a periodic current swing of 1 second at -10 mA/cm² and 5 second of current density controlled between 4.5~9.0 mA/cm². The entire pulse plating process lasted about 900 seconds. Variables such as current density, solution formulation, as well as PEG additive were investigated to identify the optimized combination for eutectic Sn-3.5wt% Ag deposition. Composition of the aqueous electroplating solutions used in our experiments is listed in table I. The plating formulation includes AgI and Sn₂P₂O₇ as ionic salts, K₄P₂O₇ and KI as complexing agents, and PEG of various molecular weights as plating additives.

To study the electrochemical characteristics of electrodeposition, current-potential curves of each plating bath were measured using EG&G potentiostat/galvanostat 273A in which a Pt plate was used as counter electrode, Ag/AgCl was chosen as reference electrode, and Cu plate of 1 cm² (99.99% Cu) was

employed as working electrode. Before each experiment the working electrode was first mechanically ground and cleaned with deionized (DI) water. The scanning rate was set at 0.5 mV/s and the conditioning time was 150 second.

The surface morphology of the plated films was examined by JEOL 6500 SEM and the chemical compositions were determined quantitatively by EDX. DSC (differential scanning calorimeter) was utilized to validate the alloy composition by recording endothermic solidus temperature with thermal scan performed from 80 to 260°C at a 3°C/min heating rate. Four-point-probe and XRD (Siemens D-5000 with Cu K_{α} line at wavelength of 1.54 Å) were used to identify electrical resistivity and phase of the resultant solder films.

A.3 Results and Discussion

A.3.1 Composition Characterization

The basic formulation for electroplating of Sn-Ag has been reported by Arai et. al. in 2003 [32] where $K_4P_2O_7$ and KI were used as complexing agents, $Sn_2P_2O_7$ and AgI were selected as ion sources, and PEG600 (polyethylene glycol with molecular weight of 600) and formaldehyde were employed as inhibitor. The formulation used in our study is listed in Table I. STD1 to STD5 contain identical ratio of ion sources and complexing agents ($K_4P_2O_7$: KI : $Sn_2P_2O_7$: AgI = 0.5 : 1.0 : 0.125 : 0.0025) with Arai's but the concentrations of those in our plating bath were reduced by half. The purpose is to slow down the electroplating process for better characterization. From Bath7 to Bath10, the concentration of AgI is reduced further to 0.00125 M while 0.001 M of PEG with molecular weight of 200, 600, 2000, and 4000 is added individually to study the influence of PEG molecular weight over plating behavior and the resultant solder film.

The formulation of STD1 contains all the necessary ingredients without any PEG

additive. Therefore, we started out with STD1 by exploring plating conditions to pinpoint the necessary process parameters for eutectic Sn-3.5wt% Ag deposit. A typical profile of the pulse plating mode is illustrated in Figure A-(a). The purpose for alternating current polarity during pulse plating is to obtain better control in morphology and film composition as both electropolishing and electroplating operate sequentially. We have reported similar results in Cu damascene process in which much improved surface uniformity of Cu layer is observed by reversing current polarity intermittently [33].

As shown from Figures A-(a) and (b), desirable Sn-3.5wt% Ag film was confirmed with the pulse plating mode at positive current density of 6.0 mA/cm^2 and negative current density of 1.0 mA/cm^2 for processing time of 15 minutes. Figure A-(b) is the SEM picture illustrating the surface morphology of as-deposited film with grain clearly seen larger than $1 \mu\text{m}$. Insert in Figure A-(b) is the EDX analysis result suggesting an uniform distribution of Sn and Ag without notable segregation. As described previously, the solidus temperature of the Sn-3.5wt% Ag solder is extremely sensitive to the concentration of Ag in the binary system. Hence, endothermic event of solidus temperature serves perfectly well as indicator reflecting the exact amount of Ag in the as-deposited alloy. In the DSC analysis in figure A-(c), an endothermic peak is recorded at 221.79°C which is consistent with what we expect from the eutectic temperature of Sn-3.5wt% Ag. In addition, the resistivity of the resultant film is measured at $15.64 \mu\Omega\text{-cm}$. The growth rate of the deposited film is determined to be $0.231 \mu\text{m/minute}$ using SEM to measure the thickness of the film.

Figure A-2 illustrates the relationship for the current density at positive polarity and the resultant Ag concentration in the SnAg film for several plating formulations. The amount of Ag is determined by EDX. The observed high amount of Ag in the low current density region is attributed to the relatively positive reduction potential of Ag^+

as compared to that of Sn^{2+} . As expected, the Ag concentration decreases sharply with increase in the current density for every plating bath. This is because at higher imposed current less favored reaction such as reduction of Sn^{2+} is able to participate as overpotential becomes considerable. This behavior is in agreement with previous report in electrodeposition of SnAg via galvanostatic and potentiostatic approaches [31].

After performing pulse electroplating with positive current density ranging between 4.5~9.0 mA/cm^2 , we collected the as-deposited films and analyzed with 4 point prob for resistivity. Their results are listed in table II. The current range for desirable eutectic Sn-3.5wt% Ag, defined as the process window, is also provided. Typically, a wider range of process window is favored for better plating tolerance. Relatively wide process window of 4.5~9.0 mA/cm^2 was observed for formulation STD2, Bath7, and Bath8. In contrast, Bath9 and Bath10 exhibited somewhat narrower process window of 6.0~7.5 mA/cm^2 , while STD1 delivered eutectic composition approximately at 6.0 mA/cm^2 . Unfortunately, eutectic composition of SnAg was not available from STD3, STD4, STD5, and STD6. It seems that reduction of Ag^+ concentration in plating formulation is beneficial to establishment of process window as evidenced by Bath 7-10. This accords nicely with the understanding that large difference in reduction potential between Ag^+ and Sn^{2+} causes composition instability in the as-deposited film. Consequently, inhibition of Ag^+ activity is necessary for repeatable plating process. The values for resistivity of the as-deposited films fall within reasonable range as expected for Sn-Ag alloy. In short, Table A-II indicates the importance in strict control over formulations and plating parameters for composition management in binary alloy plating.

The influence of PEG with different molecular weights is of great interest in Cu plating study. Previously, Kelly et. al. [33] and Healy et. al. [27] suggested that PEG

in the presence of Cl^- would adsorb on the substrate and inhibit subsequent reduction of Cu^{2+} . However, adding PEG alone exhibits a relatively small effect. In our study of Sn-Ag plating formulation, PEG shows a rather pronounced effect. Bath 7-10 include identical composition in $\text{K}_4\text{P}_2\text{O}_7$, KI, $\text{Sn}_2\text{P}_2\text{O}_7$, and AgI while PEG200, PEG600, PEG2000, and PEG4000 are added individually. PEG of higher molecular weight is likely to provide more coverage of active sites as well as stronger complexing reaction as compared to PEG of lower molecular weight. Therefore, PEG with higher molecular weight exerts stronger influence over plating process and thus the parameters for desirable composition are relatively confined. Nevertheless, PEG is needed to stabilize the plating solution to mitigate favored “plating-out” of Ag^+ . Indeed, Bath9 and Bath10 exhibit a narrower range of process window (6.0~7.5 mA/cm^2 vs. 4.5~9.0 mA/cm^2 of Bath 7-8).

A.3.2 Electrochemical Analysis

Current-potential curves for selective plating baths with PEG as additive as well as STD1 formulation are provided in Figure A-3. Electrochemical reduction of Ag^+ took place initially at approximate -0.5 ~ -0.55 V and the reducing current rose sharply when the potential becoming more negative as Sn^{2+} participated in reduction process. As expected, I-V curve of STD1 exhibited the highest current since PEG is well-established as inhibition additive. Bath7-10 contain PEG with molecular weight of 200, 600, 2000, and 4000, respectively. Among them, formulation with PEG4000 demonstrated the lowest current with the onset voltage of -0.55 V. In contrast, curve from formulation with PEG200 showed negligible difference as compared to that of STD1. Thus, we conclude that PEG4000 delivered the highest inhibition performance while PEG200 carried the lowest one. As expected, PEG200 was shown to have better process window than PEG4000.

It is to be noted that the current density used in our pulse deposition is between

4.5~9.0 mA/cm², which is in the upper range of the reducing current recorded here in I-V curve. Thus, it is suggested that substantial polarization occurred in pulse plating that promotes the reduction of Sn²⁺ and as a result, near eutectic Sn-3.5wt% Ag film was obtained at regime of relatively high current density.

A.3.3 Microstructure and phase identification

Figure A-4 shows SEM micrographs of the surface morphology of the as-deposited SnAg films from several plating formulations. The films were obtained with current density of 6.0 mA/cm² and the deposition process lasted 15 minutes. Figure A-4(a) exhibits the as-deposited film from STD1 where grains larger than 1 μm and uneven surface were clearly observed. In contrast, as evidenced from Figures A-4(b)~(d), the addition of PEG4000, PEG2000, PEG600, and PEG200 results in significant improvement in surface morphology and much finer grain. This trend suggested the positive influence of PEG as plating additive.

Figure A-5 shows the XRD pattern of the as-deposited film from Bath7 with the positive current density of 6.0 mA/cm² for deposition time of 15 minute. The diffraction peaks confirmed the existence of β-Sn and ε-Ag₃Sn phases suggesting that biphasic structure of eutectic Sn-3.5wt% Ag could be readily acquired from our pulse electrodeposition approach.

Figure A-6 exhibits DSC curves of the as-deposited film from formulation Bath7~10. As mentioned previously, the solidus temperature is sensitive to the exact composition of the SnAg alloy. In DSC, the negative heat flow represents endothermic reaction that corresponds to onset of melting for the alloy film. The temperatures of the endothermic peaks fall between 221 °C and 222 °C, which coincide nicely to the theoretical eutectic point of Sn-3.5wt% Ag at 221 °C. Hence, we are confident that eutectic SnAg solder film can be readily deposited in the pulse

plating method.

A.4 Summary

The eutectic Sn-3.5wt% Ag alloy films with homogenous composition and smooth surface morphology were readily obtained from pulse electrodeposition for plating formulations containing AgI and Sn₂P₂O₇ as ionic salts, K₄P₂O₇ and KI as complexing agents, and polyethylene glycol with molecular weight of 200, 600, 2000, and 4000 as additive. Composition analysis of the as-deposited film indicated that Ag concentration decreases with increasing deposition current. From data of DSC, EDX, and X-ray, we concluded that the processing window for desirable eutectic Sn-3.5wt% Ag composition can be extended once PEG additive is included. We attribute the widening of process window to the inhibitive characteristics of PEG molecules that retard preferential deposition of Ag⁺ ions. In addition, SEM micrographs showed that the as-deposited films with PEG as additive exhibit grains smaller than 1 μm and much improved surface morphology. From current-voltage curve, we identified that PEG with molecular weight of 4000 demonstrates the highest inhibition capability while PEG with molecular weight of 200 exhibits the least. In addition, we established that the process window can be expanded by simply reducing the concentration of active Ag⁺ concentration.

A.5 References

1. International Technology Roadmap for Semiconductors, Assembly and Packaging Section, Semiconductor Industry Association, San Jose, CA, p.4 (2003).
2. D. Suraski and K. Seeling, *IEEE Trans. Electron. Packag. Manufact.*, **24**, 244 (2001).
3. K. Nimmo, in *Proc. Electron. Goes Green 2000+*, Berlin, Germany, Sep., p.43 (2000).
4. K. J. Puttlitz, in *Proc. Short Course, 50th Electron. Comp. Technol. Conf.*, Las Vegas, NV (2000).
5. H. Nawafune, K. Ikeda, H. Kitamura, S. Mizaunoto, T. Takeuchi, and K. Aoki, *J. Surf. Fin. Soc. Japan.*, **49**, 759 (1998).
6. S. Arai and T. Watanabe, *J. Surf. Fin. Soc. Japan.*, **49**, 73 (1998).
7. T. Kondo, K. Obata, T. Takeuchi, and S. Masaki, *Plat. Surf. Finish.*, February, 51 (1998).
8. S. Arai and T. Watanabe, *Mater. Trans. JIM*, **39**, 439 (1998).
9. Y. Fujiwara, T. Narahara, H. Enomoto, K. Funada, and T. Omi, *J. Surf. Fin. Soc. Japan.*, **49**, 1316 (1998).
10. H. Nawafune, K. Shiba, S. Mizumoto, T. Takeuchi, and K. Aoki, *J. Surf. Fin. Soc. Japan.*, **51**, 1234 (2000).
11. S. Arai, N. Kaneko, and N. Shinohara, *Electrochemistry*, **69**, 254 (2001).
12. M. Jordan, *Trans. IMF*, **75**, 149 (1997).
13. H. Tanaka, M. Tanimoto, A. Matsuda, T. Uno, M. Kurihara, and S. Shiga, *J. Electron. Mater.*, **28**, 1216 (1999).
14. H. Nawafune, K. Ikeda, K. Shiba, S. Mizumoto, T. Takeuchi, and K. Aoki, *J. Surf. Fin. Soc. Japan.*, **50**, 923 (1999).

15. M. Fukuda, K. Hirakawa, and Y. Matsumoto, *J. Surf. Fin. Soc. Japan.*, **50**, 1125 (1999).
16. S. Arai and N. Kaneko, *Denki Kagaku oyobi Kogyo Butsuri.*, **65**, 1102 (1997).
17. S. Arai, N. Kaneko, and N. Shinohara, *J. Surf. Sci. Soc. Japan.*, **22**, 463 (2001).
18. F. Guo, S. Choi, J. O. Lucas, and K. N. Subramanian, *J. Electron. Mater.*, **29**, 10 (2000).
19. M. Jordan, *Galvanotechnik.*, **92**, 1225 (2001).
20. M. Paunovic and M. Schlesinger, *Fundamentals of Electrochemical Deposition*, John Wiley & Sons, New York (1998).
21. M. Schlesinger and M. Paunovic, *Modern Electroplating, 4th edition*, John Wiley & Sons, New York (2000).
22. I. Mizushima, P.T. Tang, H.N. Hansen, and M. A.J. Somers, *Electrochimica Acta*, **51**, 888 (2005).
23. I. Mizushima, P.T. Tang, H.N. Hansen, and M. A.J. Somers, *Electrochimica Acta*, **51**, 6182 (2006).
24. I. Baskaran, T.S.N. Sankara Narayanan, and A. Stephen, *Materials Letters*, **60**, 1990 (2006).
25. B. Neveu, F. Lallemand, G. Poupon, and Z. Mekhalif, *Applied Surface Science*, **252**, 3561 (2006).
26. S. Chieh Chang, J. Min Shieh, K. Cheng Lin, and B. Tong Dai, *J. Vac. Sci. Technol. B.* **20**(4), 1311 (2002).
27. J. P. Healy and D. Pletcher, *J. Electroanal. Chem.*, **338**, 155 (1992).
28. T. O. Drews, J.C. Ganley, and R.C. Alkire, *J. Electrochem. Soc.*, **150**, C325 (2003).
29. E.E. Fardon, F.C. Walsh, and S.A. Campbell, *J. Appl. Electrochem.*, **25**, 574 (1995).

30. T.P. Moffat, B. Baker, D. Wheeler, and D. Jossell, *Electrochem. Solid State Lett.*, **6**, C59 (2003).
31. S. Arai, H. Akatsuka, and N. Kaneko, *J. Electrochem. Soc.*, **150**(10), C730 (2003).
32. S. Chieh Chang, J. Min Shieh, K. Cheng Lin, and B. Tong Dai, *J. Vac. Sci. Technol. B*, **20**(6), 2233 (2002).
33. J. J. Kelly and A. C. West, *J. Electrochem. Soc.*, **145**, 3472 (1998).

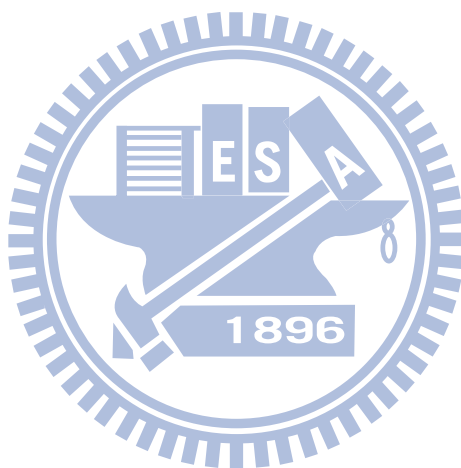


Table A-1 Composition of SnAg electroplating baths (mol dm⁻³) in our study.

	STD1	STD2	STD3	STD4	STD5	STD6	Bath7	Bath8	Bath9	Bath10
K₄P₂O₇	0.5	0.5	0.5	0.5	0.5	0.5	0.5	0.5	0.5	0.5
KI	1.0	1.0	1.0	1.0	1.0	0.5	1.0	1.0	1.0	1.0
Sn₂P₂O₇	0.125	0.125	0.125	0.125	0.125	0.125	0.125	0.125	0.125	0.125
AgI	0.0025	0.0025	0.0025	0.0025	0.0025	0.0025	0.00125	0.00125	0.00125	0.00125
PEG200		0.001		0.002			0.001			
PEG600			0.002		0.001			0.001		
PEG2000									0.001	
PEG4000										0.001

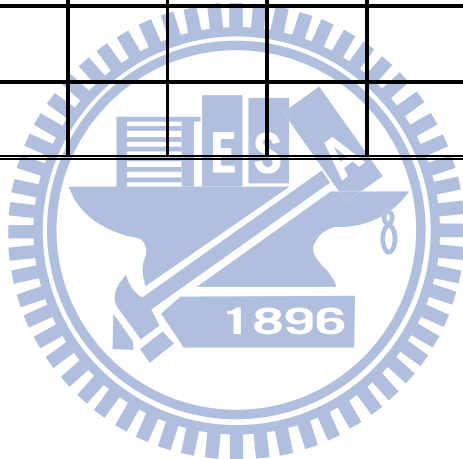


Table A-2. Composition analysis of the SnAg film from various plating baths with the process window listed for eutectic Sn-3.5wt% Ag. Also listed is the resistivity of the as-deposited film.

Process window for eutectic Sn-3.5wt% Ag		Resistivity ($\mu \Omega\text{-cm}$)
STD1	$\sim 6.0 \text{ mA/cm}^2$	15.86
STD2	$4.5 \sim 9.0 \text{ mA/cm}^2$	18.5
STD3	N/A	19.10
STD4	N/A	18.37
STD5	N/A	17.02
STD6	N/A	15.39
Bath7	$4.5 \sim 9.0 \text{ mA/cm}^2$	16.85
Bath8	$4.5 \sim 9.0 \text{ mA/cm}^2$	17.21
Bath9	$6.0 \sim 7.5 \text{ mA/cm}^2$	18.46
Bath10	$6.0 \sim 7.5 \text{ mA/cm}^2$	18.79

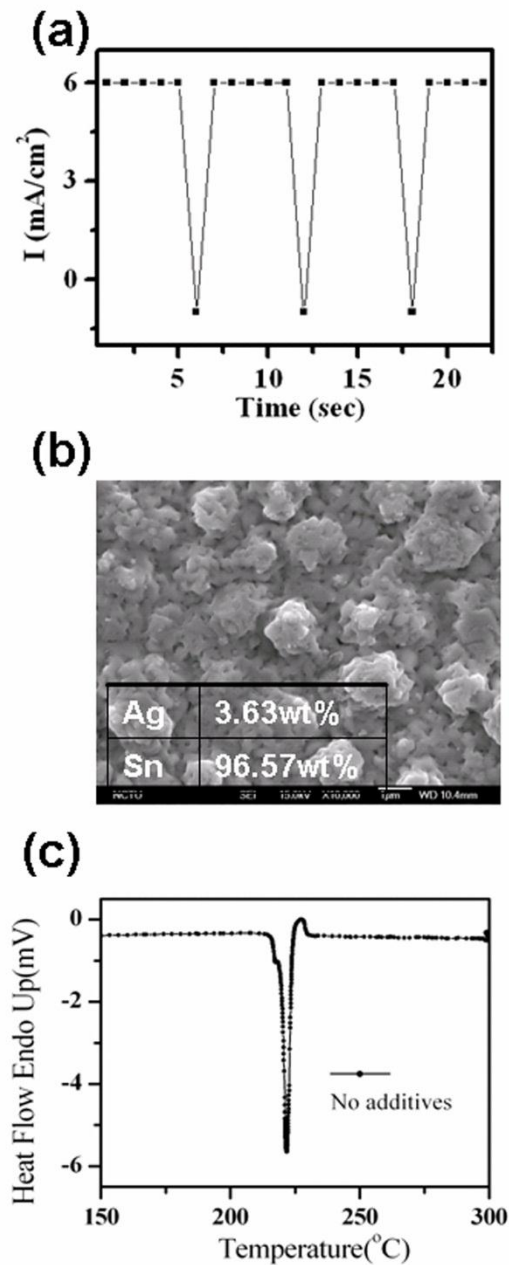


Figure A-1 Characterizations of the as-deposited SnAg film from pulse electroplating of STD1 formulation; (a) current profile for the electrodeposition process, (b) SEM micrograph of typical surface morphology, and the EDX analysis of film composition: Sn: 96.57 wt.%; Ag: 3.63 wt.%, and (c) DSC curve with endothermic peak recorded at 221.8°C.

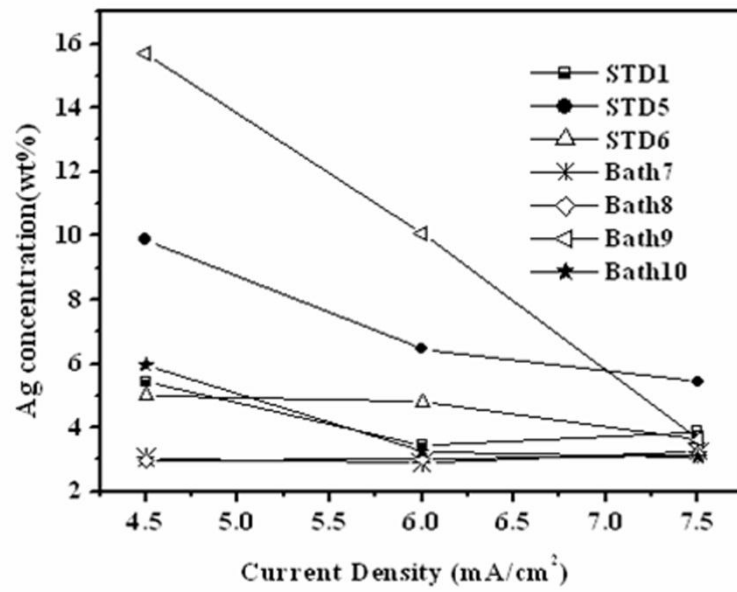
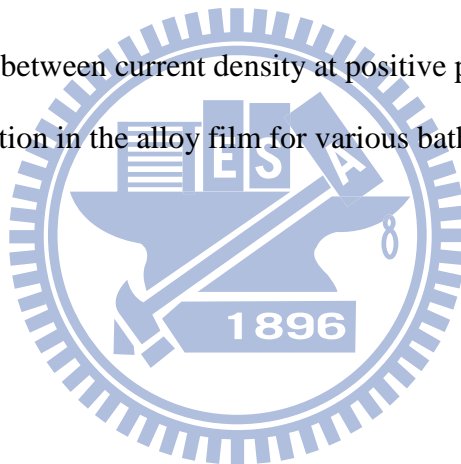


Figure A-2 Relationship between current density at positive polarity and the resulting Ag concentration in the alloy film for various baths



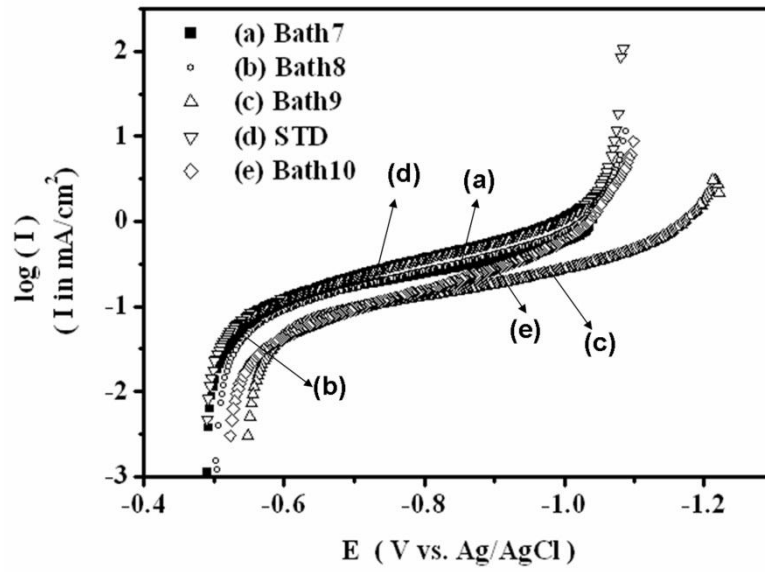
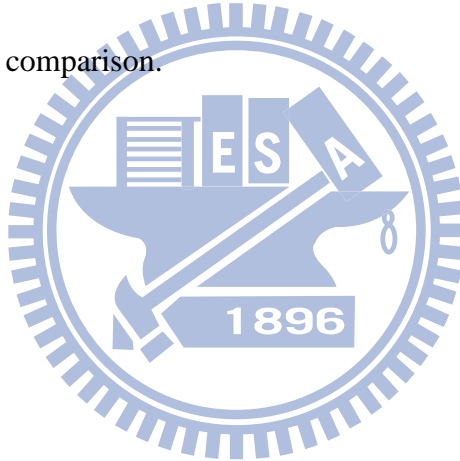


Figure A-3 Current–potential curves for several baths with PEG as additive. STD1 is included for comparison.



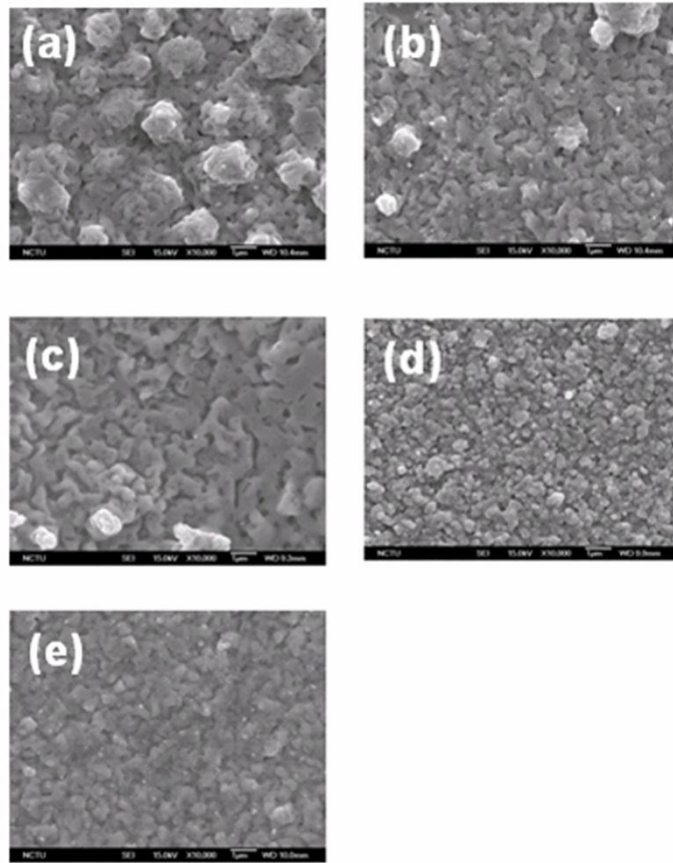


Figure A-4 SEM images of surface morphology of the as-deposited SnAg alloy films for (a) STD1, (b) STD5, (c) STD2, (d) Bath9, and (e) Bath10. EDX data confirmed their near-eutectic composition.

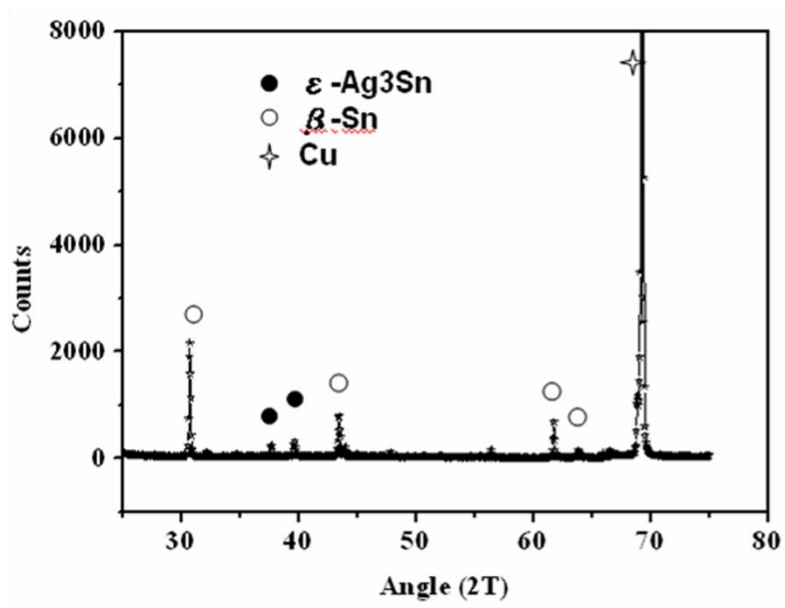
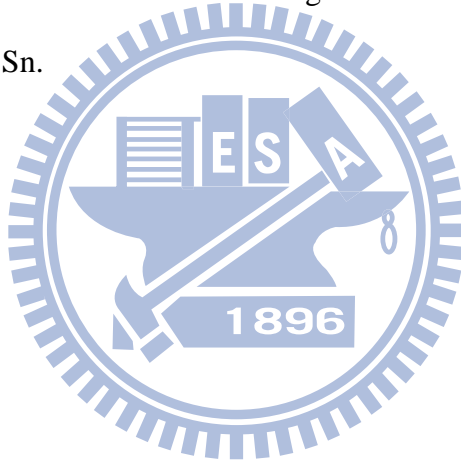


Figure A-5 XRD data for eutectic Sn-3.5wt.%Ag film showing coexistence of β -Sn and ϵ -Ag₃Sn.



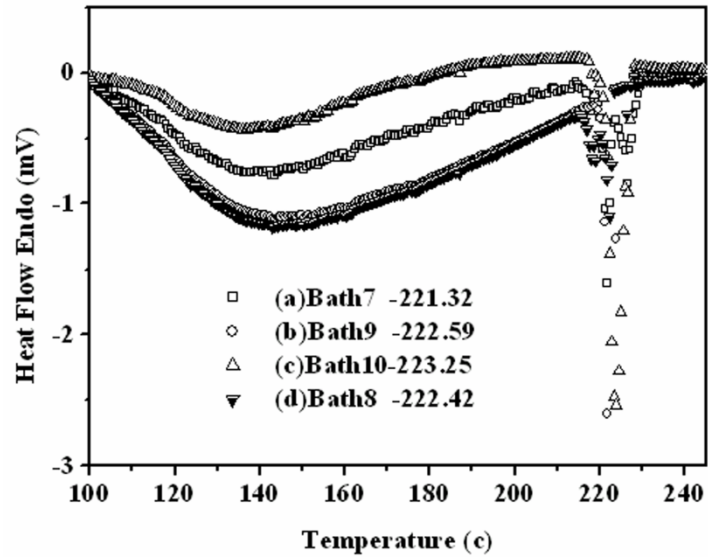


Figure A-6 DSC curve of heat flow for occurrence of solidus temperature of as-deposited SnAg film from different plating baths.



